博士論文

Impact-induced resurfacing process on asteroid Itokawa inferred from impact experiments and reflectance spectroscopy analyses

（衝突実験と反射スペクトル解析による小惑星イトカワの衝突表面更新過程の解明）

巽　瑛理

Abstract

Asteroids are very small bodies distributed mainly between the orbit of Mars and Jupiter. Smaller asteroids (< 50 km in diameter) account for approximately 30% of the total mass of main belt asteroids (MBAs) (Krasinsky, 2002; DeMeo and Carry, 2014). Many of them are expected to be rubble-pile bodies for many reason such as the spin rate distribution and the porosity estimates (Pravec and Harris, 2000; Britt et al., 2002). The Yarkovsky effect changes the orbits of smaller asteroids and finally swiftly eject from the main belt at resonances (e.g. Bottke Jr. and Vokrouhlický, 2006), while they are ground by collisions each other and become smaller and smaller. In consequence, the smaller asteroids are a main resource of the constant impact flux to the Earth. Impacts by asteroids have continuously affected the evolution of the inner Solar System planets, for example, water delivery or the dinosaur extinction. However, because the details of the physical properties of asteroids cannot be observed from Earth, their lifetime and mass evolution have not been fully understood yet.

Recently the Japanese spacecraft Hayabusa has made detailed observations of the tiny near-Earth asteroid 25143 Itokawa, which is a possible rubble-pile asteroid (e.g. Saito et al., 2006). One of the most valuable information that Hayabusa provided is the first samples from a S-type asteroid. The returned samples have presented strict constraints about its evolution (e.g. Nagao et al., 2011; Meier et al., 2014; Nishiizumi, Caffee, and Welten, 2015; Park et al., 2015). The obtained ages vary greatly depending on nuclear species of interest. A self-consistent surface evolution model to account for all those variety of ages have not been given yet.

In this thesis, we investigate Itokawa as the representative of the asteroids which are in the late stage of asteroid lifetime. Itokawa is the first rubble-pile sub-km-scaled asteroid to be observed closely and to be sampled by the spacecraft. The decreasing rate of the asteroid mass affects the migration rate of the asteroid controlled by the Yarkovsky effect. Therefore, understanding the final stage evolution of asteroids is important to constrain the impact flux to the inner Solar System and also entire main-belt mass evolution.

The goal of this thesis is to constrain the dynamical evolution of Itokawa based on the impact experiments and spectral analyses. We take three steps of investigations. First, impact experiments are conducted to elucidate the cratering mechanism on rubble-pile bodies. Second, crater distribution is simulated numerically with the Monte Carlo method and constrain the surface age of Itokawa. Finally, spectral analyses provides a global map of space weathering related to local ages.

Hayabusa revealed that Itokawa possesses many large boulders (cm-m) on the surface compared with its small body. Some impact-induced features were reported: the crater-like depressions (Hirata et al., 2009), the bright spots on boulders, and the disrupted boulders (Nakamura et al., 2008). These features and the depletion in small

craters suggest the crater efficiency reduction with surface boulder disruptions, so-called "armoring effect". Previously when the target grain size is comparable to or greater than the projectile size, a cratering efficiency reduction has been reported (Barnouin et al., 2011; Güttler, Hirata, and Nakamura, 2012). On the other hand, a recent study by Holsapple and Housen (2014) summarized that if the impact energy is much higher than the disruption energy of target grains, the cratering efficiency would not be reduced and no armoring effect would happen. Their results are not necessarily consistent to each other and the specific conditions for armoring is controversial. The crater size evaluation is important for crater chronology in historical sense, since crater distributions give tracers for their history through the crater retention age.

We conducted impact experiments using coarse-grained targets under the condition that the impactor size is comparable to or smaller than the target grain sizes as simulating the impact condition on small asteroids. We found that we can divide the cratering process into two stages, the fracture stage and the excavation stage. The fracture stage lasts very short period when the impactor hits targets. The target grains are disrupted immediately without moving in the fracture stage. After the fracture stage, the grains start to move following the momentum field as simple cratering. Thus, strengths and masses of target composed grains appear to affect the very first fracture stage. In our study, we clarify the armoring condition using two parameters: the energy ratio of impact energy and the energy needed to disrupt one target grain $\xi = \frac{1}{2} m_p U^2 / Q_D^* m_t$, and the size ratio of the impactor and the target grain $\psi = D_p / D_t$. The armoring effect worked when $\psi \lesssim 1$ and $\xi \lesssim 10^4$. There are three ranges to classify the effect: (1) the gravity scaling without armoring effect: $\xi \gtrsim 10^4$, (2) the armoring range I (cratering with heavy disrutption): $\psi \lesssim 1$ and $1 \lesssim \xi \lesssim 10^4$, (3) the armoring range II (cratering a contacted boulder): $\psi \lesssim 1$ and $\xi \lesssim 1$. The well known π-scaling analysis were performed but failed to explain our data. However, taking the momentum conversion and the disruption strength into account, we could modify the general π-scaling law (e.g. Holsapple, 1993) to fit our experimental results well. Using this new scaling enable us to assess the crater distributions on coarse-grained rubble pile asteroids. Note that on Itokawa the larger craters (> 100 m) involving the armoring effect are still more than half efficiency of cratering on sand targets and this means cratering is much more efficient compared with monolithic bodies.

High cratering efficiency on rubble-pile bodies suggests that a high excavation efficiency on cratering. The crater volume could be the reference of the mass loss due to cratering. The mass loss rate of the asteroid main belt is dominated by much more cratering than disruption by collision (Kobayashi and Tanaka, 2010). The rubble-pile asteroids can be ground down efficiently by small impactors based on our result, which leads to a reduction of the collision frequency for the larger asteroids because of a reduction of smaller asteroids as projectiles. Consequently, larger asteroids could survive for a long time.

Based on the experimental results, the crater retention age on Itokawa can be evaluated. The crater retention age on Itokawa is first estimated based on the material strength scaling on monolithic bodies (Michel et al., 2009) of 75 Myr – 1 Gyr, but the actual cratering phenomena on Itokawa, which is covered with coarse boulders can be different from the cratering on a monolithic body. Assuming that both production and erasure processes are critically controlled by impact events, the crater distribution on Itokawa was simulated by the Monte Carlo method and we examined the possible effect of armoring and impact-induced seismic shaking. The regolith moving rate by seismic shaking is still not established, but we employ the value fitted to Eros and found a better reproduction of crater distribution with armoring effect than without armoring effect. This might suggest armoring effect on Itokawa. The surface age could be derived from the larger crater's distribution because the smaller crater's reach an equivalent state. Itokawa was estimated to be younger than 10 Myr.

Crater retention ages exhibit an asteroids global age. In contrast, a map of space weathering which indicates the exposure time in space could be the index of the local age. Space weathering is the process of spectral change caused by micrometeorite bombardment and solar wind implantation over time in space. For S-type asteroids, it is known that their spectra become darker and redder by space weathering. The analyses of multi-band images taken by AMICA (Asteroid Multi-band Imaging CAmera) on the Hayabusa spacecraft presented us with a heterogeneously space-weathered surface of Itokawa (Ishiguro et al., 2007; Koga et al., 2014),while another S-type asteroid 433 Eros has a homogeneous surface. It is suggested that the first principal component (PC1) of Itokawa might indicate a degree of space weathering, reddening and darkening. That is, larger PC1 score indicates longer exposure time.

Comparison of the gravitational potential map and the PC1 map exhibited a correlation in the gradual change of PC1 score along the gravitational slope. More space-weathered particles are accumulated at the lower potential fields, especially in Muses-C and the large crater-like depression Arcoona. These features suggest the landslide-like regolith migration happens continuously on surface of Itokawa and this might be caused by impact induced seismic shaking. These spectroscopical analyses are consistent to the morphological observations by Miyamoto et al. (2007).

Using the Small Body Mapping Tool developed by APL/JHU enable the mapping of the known crater-like features on the PC1 global maps. Classification into three groups by means of PC1 score of the rim and floor of each crater was conducted: the rim-fresh craters (R), the floor-fresh craters (F), and the equally-fresh craters (E). By this classification, the large crater-like features ($\gtrsim$ 60m) with high PC1 score at the floors, that is with highly space-weathered floors, are dominated by R-types. In contrast, the small crater-like features are diverse in PC1 score, and so there are small craters ranging from new to old on Itokawa surface. However, with increasing PC1 score, that is, increasing exposure time in space, the PC1 classification type transform from F to R and E. Both of these trends suggest the modification of crater-like features over time.

If the rates of crater production and crater erasure were in an equilibrium state, craters would distribute uniformly over time (PC1 score). On the other hand, the lack of newly formed large craters might suggests change in the crater production rate.

It should also be pointed out that the old large craters possibly suggest the time of migration to the near-Earth orbit, because the impact probability in near-Earth orbit is ~ 1000 times less than in the main belt (Stuart and Binzel, 2004). The orbital lifetimes of NEAs are supposed to be a few million years (Farinella et al., 1994), and so they might have little possibility to be impacted by large meteorites in the near-Earth orbit. Thus, considering the stronger effect of space weathering by solar wind at near-Earth orbit, the ages of large craters possibly suggests the length of time in current orbit. According to the distribution of newer craters, the residence time in the near-Earth orbit is suggested to be longer than 2 Myr.

Considering all various factors which were derived by impact experiments and spectral analyses together, the evolution of asteroid Itokawa would be suggested as follows: Itokawa spent less than 10 Myr in the main belt and transited to the near-Earth orbit within the order of million years.. To sum up the residence times in the main belt and the near-Earth, Itokawa might be a very young asteroid, a few tens of million years at most. Moreover, Itokawa has geologically very energetic surface and the regolith is easy to rotate and rejuvenation the surface as the solar flare track ages and the rim deposition ages suggest (Noguchi et al., 2014; Berger and Keller, 2015). Therefore Itokawa is spectrally younger than its formed age .

Finally, two scheduled explorations will visit other small asteroids, Hayabusa2 by JAXA will visit Ryugu (1999JU3) and OSIRIS-REx by NASA will visit Bennu. Both target asteroids are smaller than 1 km and probably have coarse-grained surfaces like Itokawa. Our results of cratering efficiency on coarse-grained surfaces and spectra analyses are expected to apply to the upcoming explorations as well and reveal the dynamic evolution of each asteroid and the history of the whole main belt.

Acknowledgements

I cannot express my appreciation for my supervisor Professor Seiji Sugita enough in this small space. I could not accomplish my research without his continuous supports, encouragements and jokes. Especially, I thank him for involving me to the interesting subject, asteroids. I also thank Professor Yasuhito Sekine for constructive opinions and advices in lab seminars. I would like to pursue this subject more and hope to work together in the future too.

During experiments in ISAS/JAXA, Dr. Sunao Hasegawa and Dr. Ayako Suzuki gave me a lot of technical assistance and gave me practical advices. The experiments would not go well without them. I also thank to Mr. Kobori for helping our experiments many times and letting us to use their good instruments.

I am indebted to Professor Masahiko Arakawa and Professor Akiko Nakamura for giving me an opportunity to stay at Kobe University for a week. Discussions were very helpful and inspired me very much.

I would like to deeply express my appreciation to Professor Hirdy Miyamoto, Professor Kojiro Suzuki, Professor Toshihiko Kadono, and Professor Eiichi Tajika for giving insightful comments and suggestions, which definitely helped to improve and brush up this thesis.

It was my great pleasure to join Sugita lab. I believe that Sugita lab. was one of the leading places to study planetary science in Japan because lab members cover a wide variety of research topics, such as Earth, Mars, Moon, Jupiter and asteroids. I thank lab. members Dr. Kazuo Yoshioka, Hideharu Kuwahara, Sumire Koga, and Hukaru Furukawa. I also thank Doan to help my experiments and discuss about SMP on Hayabusa2. Sharing time with the members in Tajika lab. and Sekine lab. was even better. I thank all those members!

Special thanks have to go many other people. Those include Asako and Dr. Dent, who helped me improve English; Sachi, Tokiko, Marie, Mamiko, Abesaya, Hiroko and Chinatsu, who added a touch of color in my life; my former colleagues, who continued to encourage and share great time together even after my leaving the job, Nagao, who showed me other cultures and inspired me so much. I thank to Professor Aoki and Aoki lab. members who taught me what scientific research is and how to research. I do not forget we were working hard together through my master's course in Kyoto University. Last but not least, I really thank my family, who are always on my side, supportive and encouraging. Kyoto is at the center in my heart every moment.

So many events are intertwined each other from my birth to now and helped me grow, resulting in this thesis. I cannot even tell how many people I wish to thank.

Contents

List of Abbreviations

MBA	**M**ain **B**elt **A**steroid
NEO	**N**ear **E**arth **O**bject
SFD	**S**ize **F**requency **D**istribution
AMICA	**A**steroid **M**ulti-band **I**maging **CA**mera
PCA	**P**rincipal **C**omponent **A**nalysis
OC	**O**rdinaly **C**hondrite
CC	**C**arbonaceous **C**hondrite
CRE	**C**osmic **R**ay **E**xposure

List of Symbols

Roman symbols

a	impactor radius	m
D_a	diameter of a astroid	m
D_t	diameter of a transient crater	m
D_c	diameter of a rim-to-rim crater	m
D_p^*	diameter of a minimum projectile	m
E	irradiated energy	mJ
E_i	seismic energy injected by an impactor	J
f_x, f_y	flow rates of regolith	
g	surface gravity	$\mathrm{m/s^2}$
G	gravitational constant	$\mathrm{m^3kg^{-1}s^{-2}}$
h	regolith thickness	m
H_c	depth of crater	m
K_1	empirical parameter for pi scaling	
K_d	downslope diffusion constant	$\mathrm{m^3m^{-2}s^{-1}}$
K	sum of diffusion constant	$\mathrm{m^3m^{-2}}$
L	mean length of target grains	mm, m
m_p	mass of impactor	g
m_t	average mass of target grains	g
n	incremental number distribution	
N	cumulative number distribution	
P_i	the intrinsic collision probability	$\mathrm{km^{-2}yr^{-1}}$
Q_D^*	catastrophic disruption energy for unit mass	J/kg
t, T	time	yr
U	impact velocity	m/s
$\langle V \rangle$	mean collisional velocity	km/s
V_c	crater volume	$\mathrm{m^3}$
Y	tensile strength	MPa

Greek symbols

δ_t	density of a target grain	$\mathrm{kg/m^3}$
η	impact seismic efficiency factor	dimensionless
μ, ν	empirical paramters for pi scaling	dimensionless
ξ	energy ratio	dimensionless

π	π group parameters	dimensionless
$\Delta\tau$	time interval	yr
ρ_t	bulk density of a target	kg/m^3
ρ_p	density of a impactor	kg/m^3
ψ	size ratio	dimensionless

Subscript

a	asteroid
b	boulder
c	crater
p	projectile or impactor
t	target
s	seismic
eff	effective
imp	impact
Ito	Itokawa
tr	transient crater

Chapter 1

General Introduction

1.1 Asteroids

The largest reservoir of asteroids is the main belt, located between the orbits of Mars and Jupiter (2.0 - 3.3 AU). It currently comprises ∼1 million objects with diameter larger than 1 km (Bottke et al., 2005). The entire mass of main-belt asteroids (MBAs) is supposed to be $\sim 18 \pm 2 \times 10^{-10} M_{\odot}$ (Krasinsky, 2002) which is less than 10^{-4} of the Earth mass. In early years, asteroids had been considered as stationary objects like 'breadcrumbs' in space from the beginning of the Solar System. However, it has been desproved in these a few decades. Asteroids were suggested to move drastically over time and continuously affect the inner Solar System including Earth (Strom et al., 2005). The impact of asteroids and comets has resurfaced the terrestrial planets and their moons and may have been the carriers of water to the Earth (Morbidelli et al., 2000). Moreover, asteroid impacts have sometimes caused fatal damage to life and civilization.

Minor planets such as asteroids and comets are the most pristine materials remaining from the early stage of the Solar System. Most of them have not experienced differentiation, and they are expected to have undergone much less processing than the larger planets. Thus they preserve crucial information from the beginning of the Solar System. Meteorites are one of the materials which are available to study the pristine materials from minor planets. The relation of meteorite types and asteroid spectral types has been more and more understood from both observations and explorations (e.g. Binzel et al., 2004; Nakamura et al., 2011).

They are neither stationary nor 'breadcrumbs' in space but they still continue to change dynamically and affect the evolutions of the terrestrial planets. Thus, they are more like "breadcrumb list" to reveal the evolution of the Solar System.

1.1.1 Rubble-pile asteroids

Jeffreys (1947) introduced the idea of the gravitational aggregates of fragments made by collisional disruption of asteroids and comets, so-called "rubble-pile" bodies. They

are not monolithic bodies governed by material strength but collections of granular-like materials. Recently the hypothesis that a large portion of several tens of km-sized asteroids are rubble-piles has gained acceptance through observations and simulations.

Measurements of asteroid spin rates have suggested the interesting constraints on rubble-pile objects (Pravec and Harris, 2000). They found that small asteroids ($0.2 < D < 10$ km) have a bimodal distribution with fast rotators and slow rotators, while large asteroids have a more Maxwellian distribution. More importantly, the spin period has a threshold 2.2 hours, which corresponds to the critical breakup rotation period of gravitational aggregates with the density of ~ 3 g/cm^3 (Fig. 1.1). This fact suggests that many of asteroids of $0.2 < D < 10$ km have rubble-pile structures. Moreover, recent theoretical studies predict asteroids smaller than 0.2 km could be combined with very small cohesion (Holsapple, 2007; Scheeres et al., 2010).

From spacecraft observations, the densities of several asteroids have been reported. The NEAR Shoemaker spacecraft passed closely to C-type asteroid 253 Mathilde ($66 \times 48 \times 44$ km) to obtain the shape and mass of it. The density of Mathilde was suggested as 1.3 ± 0.2 g/cm^3, which implies the effective porosity of $\sim 40\%$, assuming that the body consists mostly of carbonaceous chondrite (Yeomans et al., 1997). More recently, the Hayabusa spacecraft visited small S-type asteroid 25143 Itokawa and took various measurements. The density of Itoakwa was suggested as 1.9 ± 0.13 g/cm^3, which implies that effective porosity of $\sim 40\%$, assuming that Itokawa consists of LL ordinary chondrites (Fujiwara et al., 2006).

The density of several other asteroids have been suggested by ground-based observations (Britt et al., 2002). Many asteroids were implied to have significant porosity (Fig. 1.2) and the asteroids with macroporosities $> 30\%$ would be loosely consolidated "rubble-pile" structures.

For these evidences, there might be many rubble-pile asteroids with diameter of less than several tens of kilometer. Among MBAs, the asteroids smaller than 50 km in diameter are supposed to consist approximately 30% of the entire mass of MBAs. Thereby, the dynamics of rubble-pile asteroids is in quite importance.

1.1.2 Migration of asteroids

Asteroids are not stationary objects but more likely to change their orbit due to the temporal scattering events induced by large planets and the steady force induced by the Solar thermal radiation. A recent hypothesis, which proposes the Solar System in earlier times would have looked very different from it does now, is known as the "Grand Tack" and is becoming popular (Walsh et al., 2011). This hypothesis suggests that two giant planets, Jupiter and Saturn, underwent an inward-then-outward migration in the first a few million years of the Solar System and drove the scattering and mixing of the primitive planetesimals which became asteroids. O ' Brien et al. (2014) denoted that the planets would accrete on order 1 – 2 % of their total mass from these planetesimals.

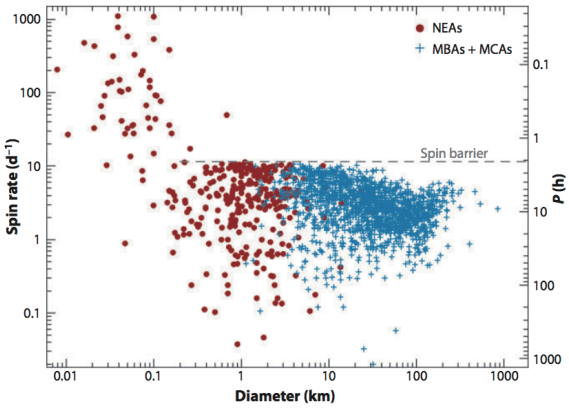

FIGURE 1.1: The asteroids spin retes. There is a cut-off of spin period at ~ 2.2 h. (From Asphaug (2009) after Pravec and Harris (2000))

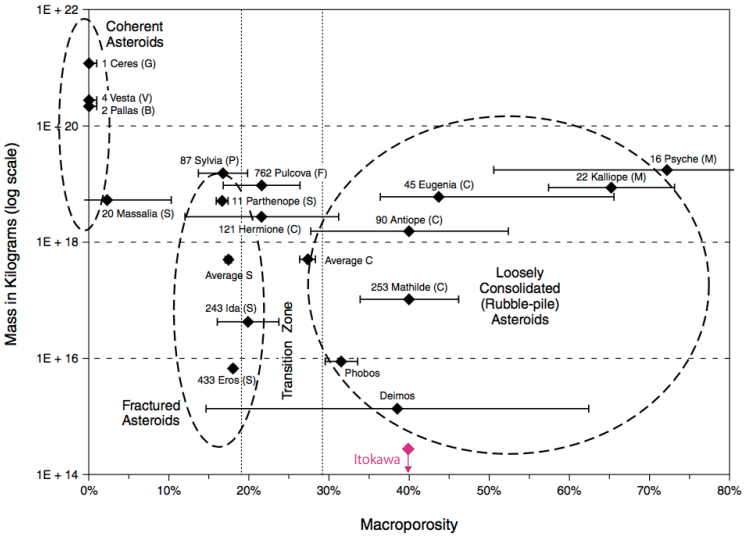

FIGURE 1.2: The asteroid porosities based on the space craft observations and ground-based observations. (After Britt et al. (2002))

Thus, this model suggests that the water on the Earth today would be delivered at that time.

There is another hypothesis that involves the scattering of asteroids. The Nice model is an hypothesis which explains the scattering of asteroids around 3.8 billion years ago, approximately 500 million years after the Grand Tack, the so-called Late Heavy Bombardment (LHB). The record of LHB is implied by the craters on the Moon as the mass of impactors needed to make late lunar basins like Imbrium is estimated to be 6×10^{21} g (Levison et al., 2001). In the Nice model, a planetary rearrangement is thought to unleash a flood of comets and asteroids throughout the Solar System (Gomes et al., 2005; Tsiganis et al., 2005). Torques from massive Kuiper Belt causes the planets to migrate and Jupiter and Saturn entered 2:1 mean motion resonance. This might cause the loss of the initial mass from Kuiper belt and the main belt. Moreover the calculation result derived after the Grand Tack model could be accounted for the initial condition of the Nice model.

However, those events occurred in the first 800 million years of the Solar System. Martian and lunar craters suggest the constant flux of asteroids to the inner Solar System still continues. What will cause the migration of asteroids after wards? After the rapid migration of asteroids just after beginning of the Solar System, the remnant of asteroids are considered to transfer steadily by the catastrophic disruption by collisions and the thermal radiation force. The asteroids sometimes collide with each other and are disrupted into smaller size asteroids, which form family asteroids. On collision, they might have gained acceleration and changed their velocity. Collision is one factor to change their orbit and another major mechanism is called the Yarkovsky effect, which is a non-gravitational acceleration produced by the anisotropic emission of thermal energy (Nesvornỳ and Bottke, 2004). The Yarkovsky effect causes small objects to undergo semi-major axis drift as a function of their spin, orbit, and material properties such as the density and the thermal conductivity (e.g. Rubincam, 1995). The Yarkovsky effect vanishes for both very small and very large objects and has a maximum mobility for $D \sim 10 - 20$ m for high thermal conductivity objects while objects as large as several tens of kilometers are still moderately affected by the effect (Bottke Jr. and Vokrouhlický, 2006). Those mechanisms can carry the asteroids to the chaotic mean motion and secular resonances which change their eccentricity and inclination. Finally they are pushed onto planet-crossing orbits and become member of the NEAs. Thus, the smaller asteroids are thought to be at the last stage of asteroid evolution and constantly hit terrestrial planets for 3.8 billion years or so.

1.1.3 Asteroid taxonomies

We can only obtain quite limited information of asteroids from ground-based observations due to their small sizes and faintness. Asteroids are commonly classified in groups by their visible and near infrared (VNIR) reflectance spectra shapes and albedos. The first color measurements for asteroids were reported by Bobrovnikoff (1929),

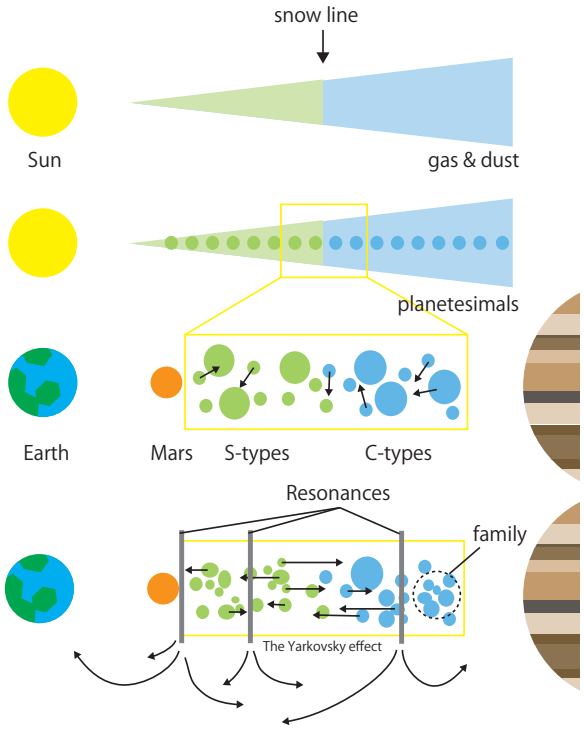

FIGURE 1.3: Schematic image of asteroid evolution from the beginning of the Solar System. The remnants of planetesimals became asteroids. They repeatedly collide with each other and are fragmented into smaller asteroids which form family asteroids. Smaller asteroids affected greatly by the Yarkovsky effet and change their orbits to reach the mean motion and secular resonances. Finally, they are swept from the main belt and some of them become members of NEAs. Itokawa could be in this last stage of the evolution.

however, at that time the measurements were neither sufficiently numerous nor precise to find out the characteristics of groups. As instruments developed, two distinct groups began to be recognized. One of the first to report a bimodal distribution in albedos was Zellner (1973), suggesting that asteroids could be divided into two groups: carbonaceous types (C-type) and stony types (S-type).

The first widely used among various asteroid taxonomies was that of Tholen (1984). The Tholen taxonomy was developed systematically using broad band spectrophotometric colors obtained during the Eight-Color Asteroid Survey (ECAS, Zellner et al., 1985). The Tholen taxonomy comprises 14 classes including the two most densely populated spectral classes of S-types and C-types.

More recently large number of asteroids were spectroscopically observed by Small Main-belt Asteroid Spectroscopic Survey (SMASS I) (Xu et al., 1995) and the following second phase (SMASSII) (Bus and Binzel, 2002b). The data is available online from `http://smass.mit.edu/smass.html`. The difference of wavelength ranges between ECAS and SMASSII disabled the data from SMASSII to classify into the Tholen taxonomy, and so the new taxonomy that builds on the Tholen taxonomy needed to be constructed. Bus and Binzel (2002a) established the new taxonomy by the principal component analysis and defined 26 classes. They first separated three main groups (C-, S-, X-complex) by the spectral slope value and principal component scores (Bus and Binzel, 2002b). The slope γ was defined by the least square fitting a line to each spectrum according to the equation

$$r_i = 1.0 + \gamma(\lambda_i - 0.55), \tag{1.1}$$

where r_i is the relative reflectance at each channel, λ_i is the wavelength of the channel in microns, forced to have the unity value at 0.55 micron. Then, the slope γ was treated as the first principal component (PC1). After each spectrum was normalized by its fitted slope function, principal component analysis was applied to derive the principal components PC2' and PC3' using the data of 1341 main-belt asteroids from SMASSII. According to this parameter sets, spectra of asteroids including NEOs spread in Slope-PC2' space as Fig. 1.4. The NEOs spread similarly as the MBAs, but they were populated more in less-sloped.

1.2 Hayabusa mission and Itokawa

Hayabusa spacecraft, launched by the Mu-V launch vehicle on 9 May 2003, was designed to acquire samples from the surface of near-Earth asteroid 25143 Itokawa (1998 SF 36) to Earth (Fujiwara et al., 2006). Hayabusa was originally developed to demonstrate the performance of various technical items such as ion engines, autonomous navigation, sampling system, and high-speed re-entry into the Earth's atmosphere

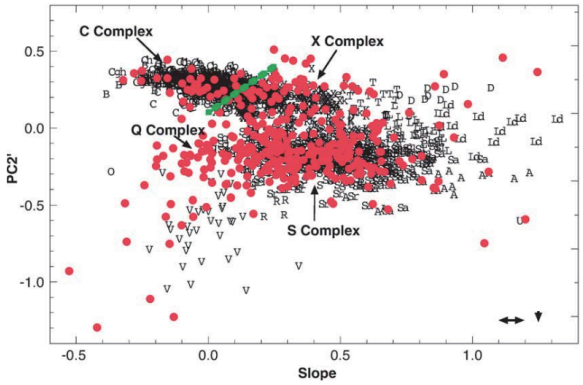

FIGURE 1.4: The Slope-PC2′ space defined by Bus and Binzel (2002b). NEOs are depicted in red. The green line denotes the boundary of C- and X- complexes. Q-complexes are found to be more common among NEOs.(from Binzel et al. (2004)

(Kawaguchi, Uesugi, and Fujiwara, 2003). However, further important scientific results have been derived so far.

After cruising with nearly one year of operation, Hayabusa experienced an Earth swingby on 19 May 2004 and arraived at Gate position (20km away from Itokawa) on 12 September 2005 and Home position (7km away) on 30 September 2005.

Observational instruments, a imaging camera with both a wide bandpass filter and seven narrowband filters (AMICA) (Saito et al., 2006), a laser ranging instrument (LIDAR) (Abe et al., 2006), and an x-ray fluorescence spectrometer (XRS), were onboard. Also a microrover named MINERVA which carried cameras and thermal probes was expected to land on the asteroid, but was not successful.

After completion of remote-sensing observations, the most challenging part of the mission, sampling on the surface of Itokawa, was performed (Yano et al., 2006). The Hayabusa team chose Muses-C regio as the sampling-site and two touchdowns were performed on 19 November 2005, however the projectiles failed to fire. Fortunately some regolith particles disturbed by the touchdowns were collected and successfully returned to Earth on 13 June 2010.

1.2.1 Information of Itokawa from ground-based observations

Itokawa is an Apollo asteroid discovered in 1998. It follows the orbital path from 0.9530 AU to 1.6947 AU which allows close encounters with the Earth. Photometric observations (Kaasalainen, Kwiatkowski, and Abe, 2003; Ohba et al., 2003) and radar observation (Ostro, Benner, and Nolan, 2004) had provided the initial physical information of Itokawa. Spectrally, Itokawa is classified as an S-type asteroid which is the most populated type of the inner main belt. Detailed spectroscopic observation revealed that surface composition of Itokawa is apparently dominated by silicates and Fe metal which implied space weathering on Itokawa (Binzel et al., 2001).

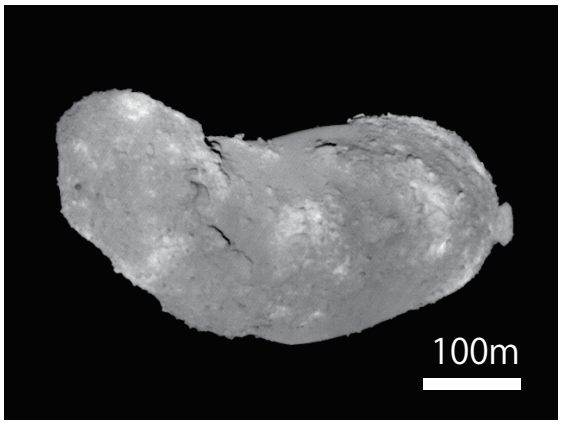

FIGURE 1.5: Asteroid 25143 Itokawa: $0.54 \times 0.29 \times 0.21$ km (ST_2458474873 by JAXA).

1.3 Impact cratering

1.3.1 Craters on small asteroids

Impact craters are commonly see on all objects in the Solar System. Some recent spacecraft observations have revealed detailed morphologies on asteroids. Craters might be the most important features in telling the asteroids' histories. The first image of asteroid surface was taken when the Galileo spacecraft encountered asteroid 951 Gaspra (Belton et al., 1992). The Galileo spacecraft images revealed the crater recorded on Gaspra ($19 \times 12 \times 11$ km) and no obvious ejecta. Galileo next headed to asteroid 243 Ida ($56 \times 24 \times 21$ km) which is Koronis family (Belton et al., 1994). Ida also had clear shaped craters on its surface and no distinct ejecta blanket.

Higher resolution images of asteroids have been obtained recently. The close encounter of NEAR Shoemaker spacecraft revealed the complete surface map of asteroid 433 Eros ($34 \times 11 \times 11$ km). Some of the craters that deposit the fine regolith on the floor, called ponds, are observed (Veverka et al., 2000). The relation of the depletion of craters in small sizes and the boulder size distribution on Eros was suggested (Chapman et al., 2002).

Most recent direct observation of an asteroid was by the Hayabusa spacecraft by JAXA. The target asteroid 25143 Itokawa was the smallest asteroid visited by spacecrafts to date: $0.54 \times 0.29 \times 0.21$ km (Fujiwara et al., 2006). The images of previously visited asteroids have shown similar impact features, regolithic smooth surfaces and bowl-shaped craters. However, Itokawa had rather blocky surface which consists of abundant meter-sized boulders, and quite irregular shaped crater-like features (e.g. Michikami et al., 2008; Hirata et al., 2009). These circular depressions are diverse in shapes and colors.

The Rosetta provided us the fine direct observations of two asteroids: the M-type asteroid 21 Lutetia and the E-type asteroid 2867 Šteins on the way to the target comet 67P/Churyumov-Gerasimenko. The Rosetta space probe flew by Lutetia ($121 \times 101 \times 75$

km) and took images of up to 60 m/pix (Coradini et al., 2011). Lutetia was found to be covered with fine material all over the surface and have numerous impact craters with diameters ranging from 600m to 55 km across (Vincent et al., 2012). The other visited asteroid Šteins was much smaller as about 5.3 km in diameter (Keller et al., 2010). This small asteroid was also covered with impact craters, while the number of smaller craters were depleted, similarly to what was found for Eros and Itokawa. The surface did not show color variations. Keller et al. (2010) suggested that the diamond-shaped Šteins is a rubble-pile and will be eventually break up by YORP spin-up.

The latest images of the asteroid 4 Vesta was provided by the Dawn spacecraft. The Dawn mission is the ongoing mission and aims to explore the asteroid 4 Vesta and the dwarf planet Ceres which are the second-largest and the largest object in the main belt. The Vesta phase of the Dawn mission lasted from May 2011 to September 2012. Numerous detailed images of Vesta had been taken by Dawn's Framing Camera, and now we see all the surface of Vesta. Many crates were found, some with ejecta blankets and large troughs extending around the equatorial region (Jaumann et al., 2012). The craters on Vesta was commonly associated with color variation such as dark material (Pieters et al., 2012; Reddy et al., 2012a). In near future, more results will reveal the surface geological features on Vesta.

All the observed asteroids had impact craters, but not all had grooves which are morphologically similar to craters excepting that those formed in lines. The groove were found on Vesta, Lutetia and Eros as well as the Martian moon Phobos. However, how these grooves were formed is still an open question.

The existence of 4179 Toutatis should be noticed as an analogical asteroid of Itokawa. The near-Earth asteroid 4179 Toutatis was observed very recently on the flyby of Chang'e-2 in 2012 (Huang et al., 2013). Toutatis has physical length and width of 4.75×1.95 km, which is as small as Š and the second smallest asteroid that was directly observed by a spacecraft. The close encounter of 770 ± 120 m obtained the high resolution images better than 3 m at most. Toutatis has similar geometrical features to Itokawa, for example a bifurcated shape with a head and body, a boulder-rich surface, shallow and irregular-shaped large craters. From these geological observations, Toutatis is supposed to be a rubble-pile asteroid. The composition of Toutatis is suggested as L-chondrite which content high pyroxene iron (Reddy et al., 2012b) and is categorized in a S-type asteroid spectrum. Thus, the chemical composition of Toutatis is also similar to Itokawa. The comparison between Toutatis and Itokawa would lead to more profound understand of S-type rubble-pile asteroid in general.

1.3.2 Cratering process

The impact cratering process is divided into three stages: contact and compression, excavation and collapse. Although these stages are a continuous process, each is dominated by different physical processes.

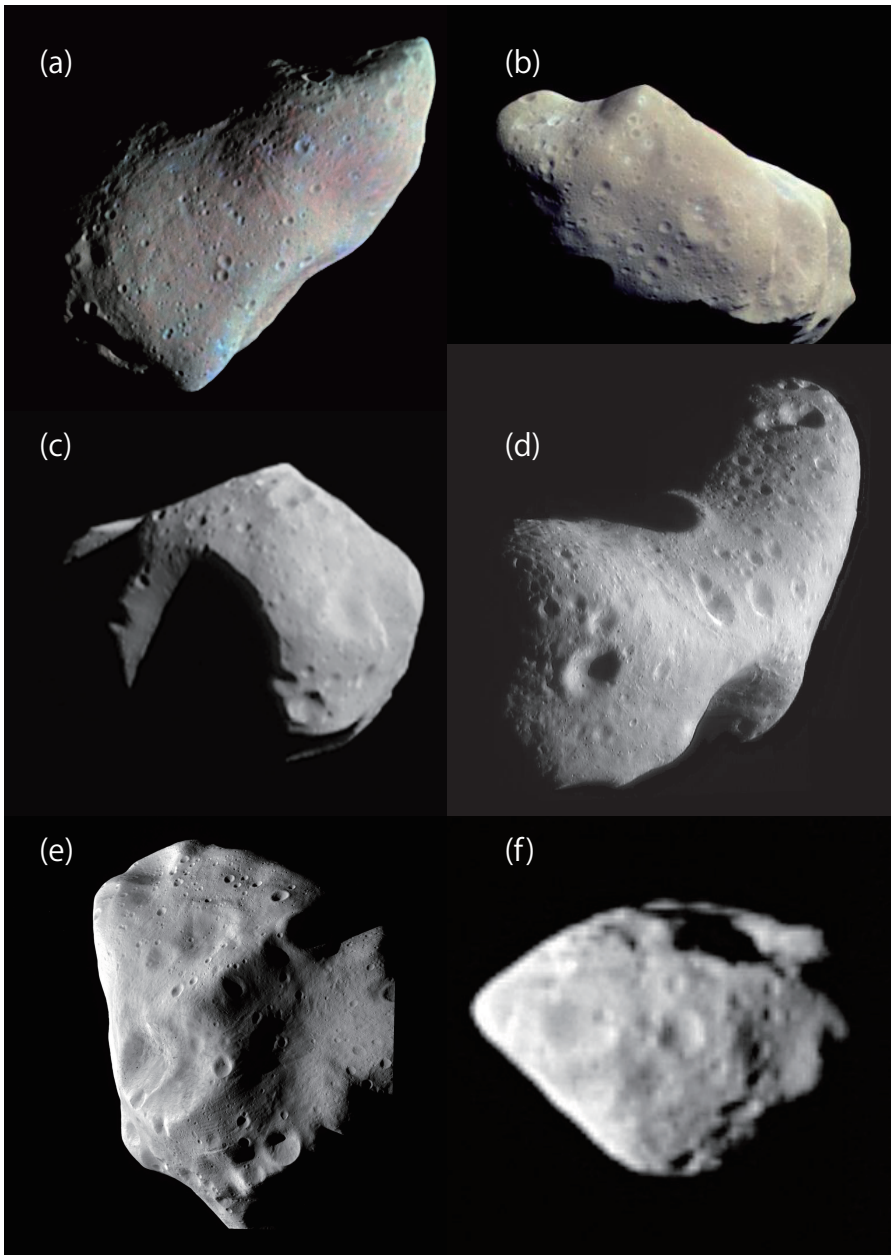

FIGURE 1.6: The surface of asteroids explored by spacecrafts. Smooth surfaces and numerous bowl-shaped craters can be seen. (a) Gapra ($19 \times 12 \times 11$ km), (b) Ida ($56 \times 24 \times 21$ km), (c) Mathilde ($66 \times 48 \times 46$ km), (d) Eros ($34 \times 11 \times 11$ km), (e) Lutetia ($121 \times 101 \times 75$ km), (f) Šteins ($6.7 \times 5.8 \times 4.5$ km). (Photos by NASA and ESA)

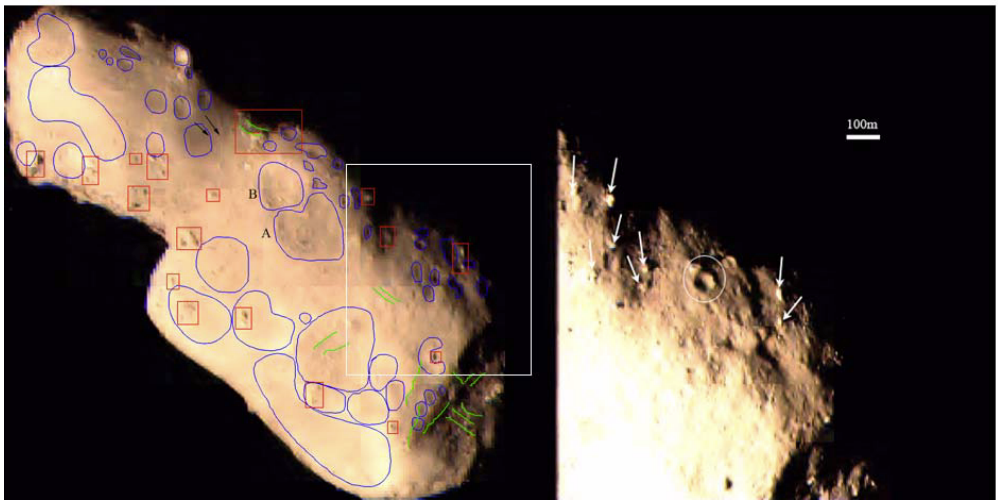

FIGURE 1.7: Geometrical features of the asteroid 4179 Toutatis (4.75×1.95 km). (a) Craters (blue profiles) and boulders (red squares). (b) White arrows indicate boulders with lengths of $\sim 20-30$ m. (from Huang et al. (2013))

The early stage of impact cratering process of hypervelocity impact events can be described as similar to an explosion due to the energy transition in a tremendously short time. In this stage, cratering has more in common with high energy explosion physics than momentum driven excavation. The first stage of the impact crater formation process begins when the impactor first contacts the target surface. Upon contacting, the impactor compress and accelerate the target and at the same time the target decelerates the impactor. Here the transference of the energy from impactor to the target occurs. The energy transference results in the formation and propagation of shock waves away from the impact point. The principal result of the contact and compression stage is to transfer most of the impactor's kinetic energy into the kinetic and internal energy of the target material. The internal energy heats the impactor and the target and results in melting and vaporization of material in close vicinity of impact site. When the target material is brittle, the material is fractured strongly around the melting point due to the compression wave and rarefaction wave coming through.

The geometry of the radial shock wave generated by an impact is that of a sphere centered on a point some distance below the surface (Melosh, 1989). Thus, the shock waves propagate upward from the impact point to the surface. Stress cannot be maintained at free surfaces and rarefaction waves develop and follow the shock wave, thereby the target is decompressed to ambient pressure. The velocity field of the target is the vector sum of the acceleration by those waves integrated over time. This residual velocity field acts to open the crater; the excavation stage starts. So called Z model devised by Maxwell (1977) well depicts the excavation flow field. The flow field derived

from the mass conservation law of the target material can be described by:

$$U(R,\theta) = \dot{R}\boldsymbol{R} + \dot{R}(Z-2)\tan\left(\frac{\theta}{2}\right)\boldsymbol{\theta}, \tag{1.2}$$

where U is the flow vector in cylindrical polar coordinates (R,θ). The Z defines the rate of velocity decay with range: $\dot{R} = \alpha(t)R^{-Z}$.

The excavation stage is stopped by cohesive strength plus dry friction which is resistant to shear of granular materials (material strength dominant regime) and gravity (gravity dominant regime). In large impacts, the crater cavity and excavation stops when the two forces - the force of the excavation flow lifting itself up and the force of gravity pulling it back - balance out. In small impacts, the crater cavity and excavation stops where the force of excavation flow equals the physical strength of the target material and and its surface friction. The largest cavity at the point of force equivalence is called the transient crater. The geometry of transient craters is a parabolic shape with a depth to diameter ratio of between 1:3 and 1:4 (Melosh, 1989).

The final stage of cratering process is the modification stage. Crater collapse or modification is driven by gravity and the final shape highly depends on the material properties such as strength and friction angle as well. The stage results in a shallower crater than its transient crater geometry that is more stable in gravity field. For simple craters, circular bowl-shaped depression, the collapse relationship between the transient and the final crater shape is well understood through experiments (Holsapple, 1993). However, for the large scale craters, the modification process is rather complex and the numerical simulations are often used for investigation (e.g. O'Keefe and Ahrens, 1999; Collins et al., 2002).

1.4 Future missions

Hayabusa2

As the importance of asteroids is being recognized, several exploration missions to asteroids are currently being planned. Hayabusa2 operated by JAXA was launched on 3 December 2015 via HIIA vehicle and planned to reach the C-type near-Earth asteroid Ryugu (1999JU3) in 2018. Hayabusa2 is basically a clone of Hayabusa including CCD cameras (ONC), a near infrared spectrometer (NIRS3), a thermal infrared imager (TIR), a laser ranging instrument (LIDAR), and sampler (SMP). In addition, Hayabusa2 has new features for an impact cratering experiment on the target asteroid, the Small Carry-on Impactor (SCI) and the stand alone observing camera (DCAM3). The second sample returning to Earth from the asteroids is expected in 2020. Samples from asteroids might record the earliest history of the Solar System. Furthermore, C-type asteroids are expected to contain abundant organic components which possibly were carrier of organics to the Earth and caused more complex organic components.

OSIRIS-REx

NASA also plans to send the spacecraft OSIRIS-REx to the D-type near-Earth asteroid Bennu. This mission is also a sample return mission from a carbonaceous asteroid. The spacecraft will be launched in 2016 and reach Bennu in 2018.

MarcoPolo-R

The MarcoPolo-R mission by ESA aims to sample the near-Earth asteroid 2008 EV5. The asteroid is expected to be a particularly primitive object which accreted in a volatile-rich region of space. The short mission duration of 4.5 years means the spacecraft will return to Earth at almost the same time of Hayabusa2 and OSIRIS-REx.

As is described above, near-Earth asteroid sample return missions are regarded as quite important by leading agencies. All these target asteroids are smaller than 1 km in diameter and our experiments and analyses are expected to apply to those asteroids. The information from various types of asteroids through future explorations is expected to provide us the key to understand the early history and the compositional questions of the Solar system.

1.5 Outline of this thesis

1.5.1 Motivation and aims

The motivation behind this thesis is to understand the surface evolution and history of rubble-pile asteroids, which are commonly populated among small objects in the Solar System. Furthermore, the rubble-pile asteroids are supposed to be in the late stage of asteroid evolution and might control the impact flux to the inner Solar System. However, information about small asteroids is limited from the ground-based observations due to their faintness. Recently, the NEAR Shoemaker spacecraft and Hayabusa have visited S-type asteroids and provided us detailed information of their morphological features. We hope to understand the evolution of the main belt and the effect to the Earth or other inner Solar System planets so far, but, understanding of the surface processes of a specific small asteroid is important enough to constrain the dynamical evolution of asteroids. Itokawa could be a representative of such a large number of small asteroids in the last stage of their evolution and un understanding of the phenomena on Itokawa would lead to an understanding of the entire main-belt mass evolution. Therefore, we investigate the most dominant and crucial phenomena of Itokawa, mainly focusing on the impact-induced cratering in this thesis. The primary objective of this thesis is to reveal the surface evolution of the rubble-pile asteroid Itokawa. Other than crater age, various ages have been estimated about Itokawa, however, what those ages suggested dynamically is not fully explained. Our secondary goal is to explain the history of Itokawa coherently by those ages.

1.5.2 Structures

The following Chapter 2 to Chapter 4 are designed to stand alone. Each chapter begins with a brief introduction and ends with a conclusion. However, they are in logical order and relate each other, sometime using the results in the previous chapters.

Chapter 2 discusses the cratering process on coarse-grained asteroid surfaces. The impact experiments on coarse-grained targets with both hyper-velocities and low velocities are reported. The armoring effect, reduction of cratering efficiency by the large grains on surface, is evaluated by proposing a new scaling law based on the classic π scaling (e.g. Holsapple, 1993). In addition, the mechanism of armoring effect will be discussed through the quarter-space experiments.

Chapter 3 describes the simulations of crater distribution on Itokawa. This chapter addresses to estimate the surface age of Itokawa. First, the modeling of crater production and erasure is discussed. And the crucial parameters which easily change the crater production and erasure rates will be examined. Finally, we compare the crater-like morphology distribution reported by Hirata et al. (2009) and the simulated distributions with our Monte Carlo code.

Chapter 4 shows the crater relative oldness distribution of Itokawa. In this chapter, the spectra principal component analyses using the images taken by the multi-band imaging camera loaded on the Hayabusa spacecraft is conducted and the principal component (PC) maps are depicted. From the PC maps, the degree of space weathering corresponding to the time of exposure in space for each crater-like features are implied by the first principal component score. The chronology of crater formation is discussed and we tried to constrain the history of surface evolution of Itokawa.

Chapter 5 gives discussion on the dynamical evolution of Itokawa. This chapter first reviews possible resurface mechanisms on Itokawa and ages investigated in other ways. Subsequently, the scenarios of Itokawa's evolution based on our results and also the ages from previous papers of such as sample and spectral analyses are given.

Finally, Chapter 6 gives the brief conclusions of each topics in the chapters.

Chapter 2

Armoring effect: Impact experiments on coarse-grained targets

2.1 Introduction

Japanese spacecraft Hayabusa made remote sensing observation and took numerous detailed pictures of the near-Earth asteroid 25143 Itokawa on 2005 (Fujiwara et al., 2006; Saito et al., 2006). This was the first spacecraft observation of a rubble-pile asteroid and provided us many information of surface structures on a rubble-pile asteroid, while we cannot observe directly its surface texture from the Earth.

These days it is widely accepted that the "rubble-pile" objects, which are loosely bound, gravity-dominated aggregates with negligible tensile strength (e.g. Fujiwara and Tsukamoto, 1980), are familiar among asteroids. The bi-modal distribution of rotational periods implied the major existence of rubble-piles among asteroids $0.2 < D < 40$ km(Pravec, Harris, and Michalowski, 2002). Recently, asteroids smaller than 0.2 km in diameter are also suggested to be loosely combined by very small cohesion even if they rotate faster than the spin barrier where gravitational aggregates break up (e.g. Holsapple, 2007; Scheeres et al., 2010; Rozitis, MacLennan, and Emery, 2014). Moreover, the porosities of asteroids smaller than a few tens km are small (Britt et al., 2002). The total mass of the main belt asteroids (MBAs) was estimated as 3.6×10^{21} kg from an analysis of the motion of the Mars, constraining the contribution of asteroids too small to be seen individually (Krasinsky, 2002). Subtracting the known masses of the largest asteroids from the total mass of the main belt, the minor asteroids (<50 km) are supposed to occupy $\sim 30\%$ of the total mass of MBAs. Another characteristic of small asteroids that can be observed by ground-based telescopes is the thermal inertia of asteroids, which allows us estimate the physical condition, such as blocky or covered by fine regolith. Km-sized asteroids have more than two orders of magnitude higher thermal inertia than larger asteroids (200 – 1000 km), which suggests the small asteroids are expected to have less regolith and more course-grained surface (Delbo' and Tanga, 2009). This observational result is consistent with the short collisional lifetimes of small

asteroids, which might have immature surfaces in regolith fragmentation. Thus, the small members of asteroids are possibly dominated by coarse-grained surfaces.

The astroid Itokawa would well represent such rubble-pile asteroids with coarse-grained surfaces. The surface of Itokawa has two distinct types of terrains, so-called rough terrains, which occupies $\sim 80\%$ of its surface, and smooth terrains (Saito et al., 2006). The most of the surface is covered by cm to m-sized angular boulders. The boulder size ranges rather large compared to Itokawa's small body ($0.54 \times 0.29 \times 0.21$ km). More detailed description of boulder size distribution is given in Sec. 3.1.3.

Another type of distinctive geological features on Itokawa are circular depressions, which is formed possibly by meteoroidal impacts (Hirata et al., 2009). The depressions were mostly found on the rough terrain. The number density of the larger depressions $\gtrsim 100$ m is almost at the crater empirical saturation level, although that of the smaller ones ($<$10 m) is lower than saturation by more than two order of magnitude. Thus, the power-law-index of the crater distribution was found to be much shallower than the lunar crater distribution. The reason for the depletion in small depressions could be caused by the combinations of production rate reduction and crater erasure processes. The regolith migration which is suggested by Miyamoto et al. (2007) and Tancredi, Roland, and Bruzzone (2015) might deform impact craters and finally could erase. On the other hand, close-up images of Itokawa surface with pixel resolution of ~ 6 mm to ~ 70 cm taken by the Asteroid Multi-band Imaging CAmera (AMICA) provide us the imprints of those processes (Fig.2.1). The presence of small meteorite collisions to boulders on the surface of Itokawa were reported by Nakamura et al. (2008), such as boulders of the possible fragments (Fig. 2.1(a)) with angular and conical shape and numerous bright spots on some boulders (the arrows in Fig. 2.1) which probably indicate fresh areas. Those features might suggest the presence of meteoroidal collisions without excavation of the substrates because the disruption energy of surface large boulders is too large to be ignored compared with the size of meteorites. Especially on small km-sized asteroids, whose surfaces are covered with coarse grains, the condition that the target grain size is comparable or larger than the projectile size occurs frequently. Such impacts on large grains may cause so-called an "armoring effect", in which, the large boulders on asteroid surface behave as armor. This effect was predicted in previous study (e.g. Barnouin-Jha, Cintala, and Crawford, 2005; Güttler, Hirata, and Nakamura, 2012). However, the quantitative analysis for the armoring effect in real situations, i.e., cratering involving heavy disruption of target grains, has not been achieved, although several experiments with limited condition were performed. Due to this uncertainty age estimate may vary significantly with crater size scaling. The precise age estimation for rubble-pile asteroids needs precise crater scaling law. Furthermore, a quantitative analysis is needed for the comparison with crater erasure rate. The goal of this study is to evaluate the efficiency of cratering on coarse-grained targets and investigate the armoring mechanism. To achieve this goal, we performed impact experiments using coarse-grained targets that simulate rubble-pile asteroids surfaces. More specifically,

the impact crater dimensions are measured and analyzed based on dimensional analysis. Then, we formulate an extended π scaling law to estimate crater size on coarse-grained targets in order to apply for asteroid surfaces. In this study, the age of Itokawa and its dynamical history is investigated.

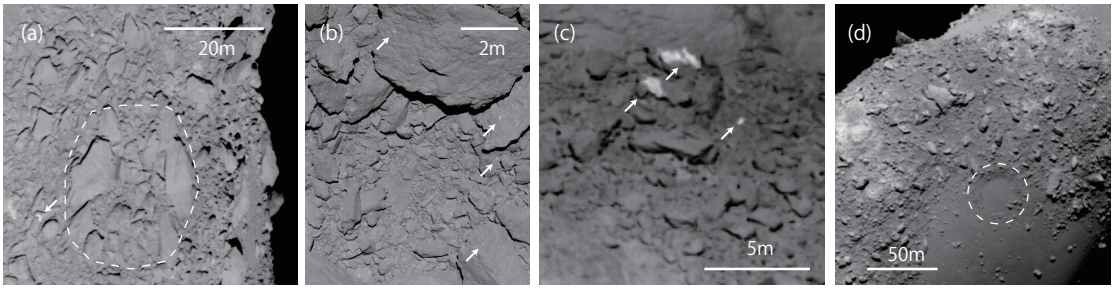

FIGURE 2.1: Itokawa's collisional imprints. (a) Angular and conical boulders' cluster (dashed enclosure) and a write spot (arrow) (ST_2530286817). (b) White spots (arrows) are considered to be relatively fresh areas (ST_2539444467). (c) A zoom up image of white spots (ST_2566271576). (d) A crater-like circular depression whose floor is filled with fine particles. (Nakamura et al., 2008; Hirata et al., 2009)

2.2 Previous experiments on coarse-grained targets

Several experiments on coarse-grained targets have been conducted and revealed that the ratio of target grain size to projectile size influences the cratering process greatly (Cintala, Berthoud, and Hörz, 1999; Barnouin-Jha, Cintala, and Crawford, 2005; Güttler, Hirata, and Nakamura, 2012; Holsapple and Housen, 2014). The first series of experiments on this issue was conducted by Cintala, Berthoud, and Hörz (1999). They used the 1 – 3 mm coarse-grained sand as targets and aluminum spheres of 4.76 mm in diameter as impactors. In their experiments impactors and target grains are comparable in size, although impactors were still larger than grain size. Although their primary interest was ejecta velocity, they have also found that the crater size was same as the crater size on fine-grained sand and that crater shapes with the depth/diameter ratios of $\sim$ 0.23 are similar to simple craters. More recently, Hayabusa mission revealed the asteroid Itokawa possesses a surface condition very different from the other explored asteroids (e.g. Fujiwara et al., 2006; Saito et al., 2006), bringing cratering processes on coarse-grained targets to many researchers' attention (Barnouin et al., 2011; Güttler, Hirata, and Nakamura, 2012; Holsapple and Housen, 2014). Low-speed ($\sim$200 – 300 m/s) cratering experiments on coarse glass sphere targets with a variety of the size ratio of projectile to target grains by Güttler, Hirata, and Nakamura (2012)revealed that the crater sizes on the coarse-grained targets are controlled by the size ratio of the projectile and the target grain. More specifically, when the ratio of the projectile and the target grain size is given, the armoring effect of crater reduction from the gravity

scaling is constant regardless of impact velocity. However, this estimation should apply to low-velocity cratering. Barnouin et al. (2011) suggests the velocity dependency of the armoring effect. More recent impact experiments at velocities high enough to fully disrupt a target grain revealed that craters formed under such condition as large as craters on dry fine sand (Holsapple and Housen, 2014), suggesting that armoring effect observed at low velocities may not be very pronounced at high velocities ~ 5 km/s. Previous experiments are necessarily consistent to each other, especially in velocity dependency. Then, we use the ratio $\xi = \frac{1}{2}m_p U^2/m_t Q_D^*$ of the impact energy to the disruption energy of a target grain as well as the size ratio $\psi = D_p/L$ of projectile to target grains in our analyses. In fact, Fig. 3.6, showing the relationship of armoring effect occurrence and experiments conditions of previous experiments in size ratio of projectile to target grain and energy ratio of impact energy to disruption energy, reveals the dependency in not only size but also energy, i.e., velocity. This figure shows armoring effect may occur when a projectile is smaller than a target grain size and impact energy is smaller than disruption energy of a grain. Previously the energy ratio did not be taken into account, but we found that the energy ratio account for the armoring condition. Thus, the armoring condition should be examined based on this phase diagram.

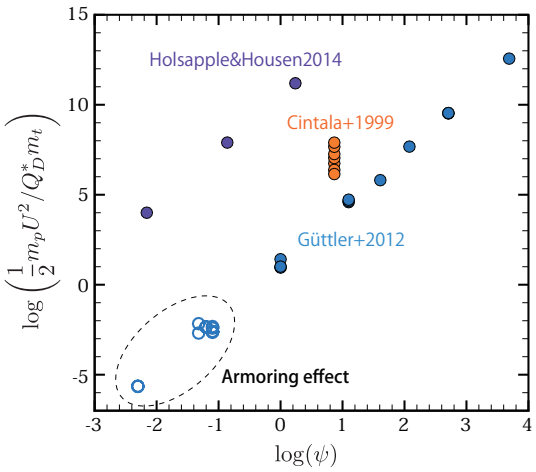

FIGURE 2.2: Phase diagram indicated by ψ (projectile size/ target grain size) vs. ξ (impact energy/ catastrophic disruption energy for one grain). Both parameters ψ and ξ might affect impact process.

Numerical simulations have been performed for cratering of granular or fractured materials namely using DEM (Discrete Element Method) and SPH (Smooth Particle Hydrodynamics) (e.g. Nolan et al., 1996; Barnouin-Jha, Cintala, and Crawford, 2002; Wada, Senshu, and Matsui, 2006; Jutzi, Michel, and Benz, 2010). Armoring is a complex phenomenon that involves disruption of grains and excavation dominated by momentum transferring. Both numerical method have advantages and disadvantages for simulating the individual mechanisms, but the models are have not answered this complex armoring mechanism yet.

2.3 Scaling law of impact process

2.3.1 π scaling law and the coupling parameters

In order to estimate the crater size on planets with different gravities and material conditions from experimental data in laboratories, scaling laws are needed. Craters are resulted from complex processes involving the balance in mass, momentum, and energy of the material and also the equation of states. Holsapple and Schmidt (1987) proposes one point-source measure that determines the final outcome, "coupling parameter":

$$C = aU^{\mu}\rho_p^{\nu}, \tag{2.1}$$

assuming to measure the results in the far field of the impactor with radius a, velocity U and mass density ρ_p. If the kinetic energy dominates all result, $\mu = 2/3$, $\nu = 1/3$ and if the momentum dominates all result, $\mu = 1/3$, $\nu = 1/3$. Then, they developed this relation to more generalized formulations based on the Buckingham π theorem of dimensional analysis (Buckingham, 1914). Starting from the crater volume V_c:

$$V_c = f[aU^{\mu}\rho_p^{\nu},\, \rho_t,\, Y,\, g], \tag{2.2}$$

where ρ_t and Y are the density and the strength of the bulk target and g is the surface gravity, they derived set of for dimensionless, π group parameters,

$$\pi_V = \frac{\rho_t V_c}{m_p}, \tag{2.3}$$

$$\pi_2 = \frac{g}{U^2}\left(\frac{m_p}{\rho_p}\right)^{1/3} = 3.22\left(\frac{ga}{U^2}\right), \tag{2.4}$$

$$\pi_3 = \frac{Y}{\rho_t U^2}, \tag{2.5}$$

$$\pi_4 = \frac{\rho_t}{\rho_p}. \tag{2.6}$$

The π_V is called the cratering efficiency, where $m_p = (4/3)\pi a^3\rho_p$ is the projectile mass. The π_2 is called the gravity-scaled size, and π_3 is called the non-dimensional strength indicating a measure of the importance of target strength Y in cratering event. Performing dimensional analysis using these four parameters is usually called π scaling, and leads to solution as:

$$\pi_V = K_1\left[\pi_2\pi_4^{(6\nu-2-\mu)/3\mu} + \left[K_2\pi_3\pi_4^{(6\nu-2)/3\mu}\right]^{(2+\mu)/2}\right]^{-3\mu/(2+\mu)}. \tag{2.7}$$

Assuming that K_2 is close enough to unity to permit the quantity K_2Y to equal an "effective" target strength $\bar{Y}$, eq.(2.7) is simplified as (Holsapple, 1993):

$$\pi_V = K_1\left[\pi_2\pi_4^{-1/3} + \bar{\pi}_3^{(2+\mu)/2}\right]^{-3\mu/(2+\mu)}. \tag{2.8}$$

Furthermore, the crater depth is roughly $1/3$ of the crater diameter by experimental results (Schmidt and Housen, 1987), and the crater diameter is derived from the relationship,

$$V_c = \frac{1}{24}\pi D_c^3. \tag{2.9}$$

If the force of gravity is much higher than the effective strength,

$$V_c = K_1 \left(\frac{m_p}{\rho_t}\right) \left(\frac{ga}{U^2}\right)^{-3\mu/(2+\mu)} \left(\frac{\rho_t}{\rho_p}\right)^{\mu/(2+\mu)}, \tag{2.10}$$

which is called gravity-dominated scaling law. In contrast, if the effective yield strength is much higher than the force of gravity,

$$V_c = K_1 \left(\frac{m_p}{\rho_t}\right) \left(\frac{\bar{Y}}{\rho_t U^2}\right)^{-3\mu/2}, \tag{2.11}$$

which is called strength-dominated scaling law. The parameters for geological materials are given in Table 2.1 from Holsapple (1993).

TABLE 2.1: Parameters for π-scaling (Holsapple, 1993).

Material	K_1	μ	$\bar{Y}$ [MPa]
Dry soil	0.24	0.41	0.18
Water	2.3	0.55	0
Soft rock	0.20	0.55	7.6
Hard rock	0.20	0.55	18

Using this scaling, the craters on Itokawa and the Moon are estimated in Fig. 2.3. The transition point from the strength scaling to the gravity scaling depends on the effective strength of the target material. The "effective" strength may include material tensile strength, friction, inter-locking resistance, and adhesion. Surface gravity even affects the "effective" strength through friction. Comparison between observations and theoretical calculations suggest the cohesive strength of small asteroids is a few tens Pa (Sánchez and Scheeres, 2014; Rozitis, MacLennan, and Emery, 2014). If the effective strength of Itokawa was a few tens Pa, the transition crater diameter between strength-controlled to gravity-controlled regimes is smaller than 1 m. Thus, the crater > 1 m can be predicted well with the gravity scaling if the target is fine regolith. Note that the crater size on rock target predicts more than 10 times smaller than that on sand with the small effective strength of 1 kPa.

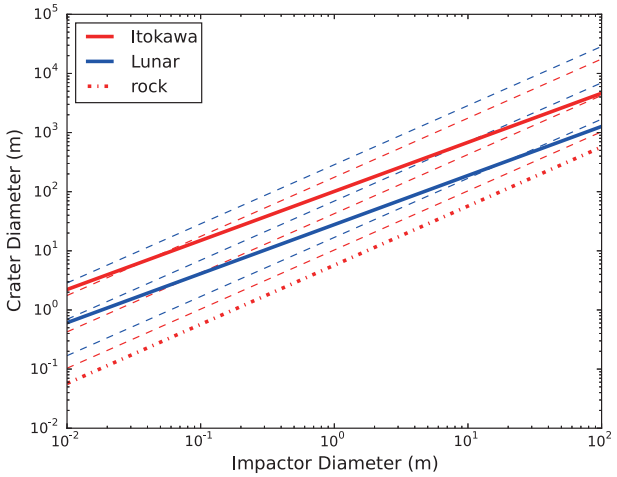

FIGURE 2.3: Crater sizes on Itokawa and Lunar estimated from π scaling eq. (2.8). (solid) Gravity-dominated scaling. (dashed) Strength-dominated scaling for sand with $\bar{Y} = 1\mathrm{MPa}, 1\mathrm{kPa}, 1\mathrm{Pa}$ in order from the top. (one-dot) Strength-dominated scaling for continuum target with $\bar{Y} = 18$ MPa corresponding to the strength of hard rock.

2.4 Impact experiments

2.4.1 Experimental conditions

Our interest is realistic cratering on rubble-pile asteroids with fragmentation of grains, where projectiles are comparable to or smaller than target grains in size and impact energy is larger than the disruption energy of one grain. We used two vertical guns in the University of Tokyo and Institute of Space and Astronautical Science/Japan Aerospace Exploration Agency (ISAS/JAXA), for impact velocities 79 - 224 m/s and 1 - 6 km/s, respectively (Fig. 2.4). We used polycarbonate projectiles 0.76 - 0.77 g in mass and 10 mm in diameter for the former gun and 0.068 g in mass and 4.7 mm in diameter for the latter gun, respectively. The shapes of the projectiles are "bullet shape" with spherical head and cylindrical tail for the former gun and for the latter gun.

We used pumice ($\sim$7, 9, and 16 mm), basalt ($\sim$ 10, and 18 mm), sintered-glass-beads (SGB) ($\sim$ 12 mm) and soda glass sphere (10 mm) as boulder target simulants. By choosing relatively fragile sintered-glass-beads (e.g. Setoh et al., 2010) as the target materials, we reproduced the condition of cratering involving disruption at low impact velocities. Besides these fragile materials, we used basaltic blocks and pumice blocks, which possess higher mechanical strength, over the entire velocity range. The material properties we used are summarized in Table 2.2. The grain size distributions in our experiments are given in Fig. 2.6, where all the averages of mean diameters have comparable to or greater than impactor size (i.e., $\psi \gtrsim 1$). Because the catastrophic disruption energy of pumice and sintered-glass-beads are ~ 2000 J/kg and ~ 30 J/kg, energies required to disrupt one grain are ~ 0.5 J and ~ 0.04 J, respectively. These are smaller than the impact energies of all of our experiments. The schematic configuration of experiments

TABLE 2.2: The mechanical properties of the materials used as targets.

Material	Density (g/cm^3)	Comp. Str. (MPa)	Q^*_D (J/kg)	Q^*_V (J/m^3)
Sintered-glass-beads	1.48 ± 0.15	0.5 - 5[a]	34	$\sim 5.1 \times 10^4$
Pumice	0.72 ± 0.1	854 ± 195[b]	2380[c]	$\sim 1.7 \times 10^6$
Basalt	2.7 ± 0.1	$\sim 100 - 300$[d]	$\sim 800 - 1000$[d]	$\sim 2.2 \times 10^6$

(a) Setoh et al. (2010), (b) Patmore et al. (2014), (c) Flynn et al. (2015), (d) Takagi, Mizutani, and Kawakami (1984).

is illustrated in Fig.2.5. Impact velocity was measured by a pair of laser detecting systems. Note that all the impacts were vertical, and each shot was recorded by high-speed cameras (NAC, Fx-4 and Q1v) at 5000 – 8000 fps of framing rate. Some of the experiments were performed in quarter space to observe the impact process underneath the target surface. We measured the final rim-to-rim diameter and depth of craters. The cross-section profiles of high-velocity cases were obtained by a laser profiler (Keyence, LJ-V). However, the shapes of the craters are sometimes difficult to determine, especially for low-velocity cases because the craters become comparable to the large grains in targets. In order to resolve this problem, we colored the initial targets surface with spray and make it noticeable which grains have moved. This technique turned out to be very effective and allowed us to discern which portion of the target is excavated (Fig. 2.7).

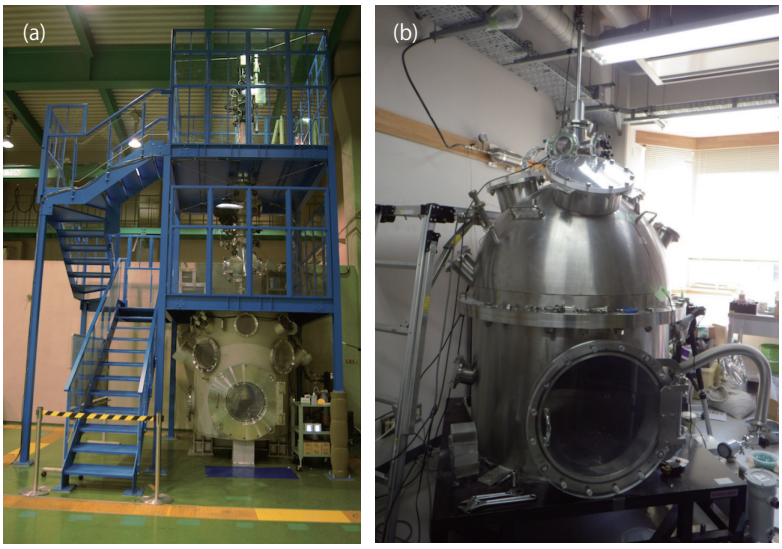

FIGURE 2.4: Two gas gun ranges used in this study. (a) The two-stage light gas gun range in ISAS/JAXA with velocity range of $\sim 1 - 6$ km/s. (b) The one-stage light gas gun range in the University of Tokyo with velocity range of $\sim 70 - 220$ m/s.

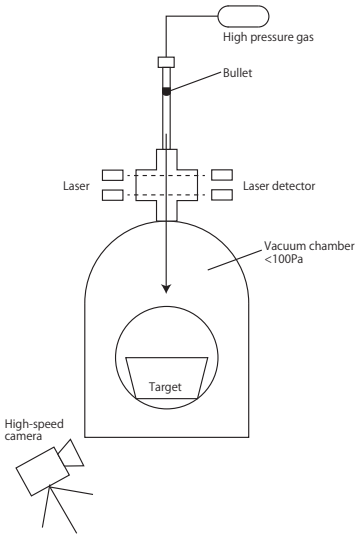

FIGURE 2.5: A schematic diagram for our experimental setting at the Univ. of Tokyo. The fundamental mechanism is same in the gun of ISAS/JAXA that have two stages of gas compression.

TABLE 2.3: The size and mass of the target grains.

Target name	Median mass (g)	Average mass m_t (g)	Average mean diameter L (mm)
Basalt (middle)	0.83	1.06 ± 0.63	9.9
Basalt (large)	6.25	6.46 ± 2.50	18.1
Pumice (small)	0.094	0.106 ± 0.045	7.0
Pumice (middle)	0.220	0.232 ± 0.077	9.1
Pumice (large)	1.20	1.29 ± 0.57	15.6
SGB	1.00	1.05 ± 0.45	11.7

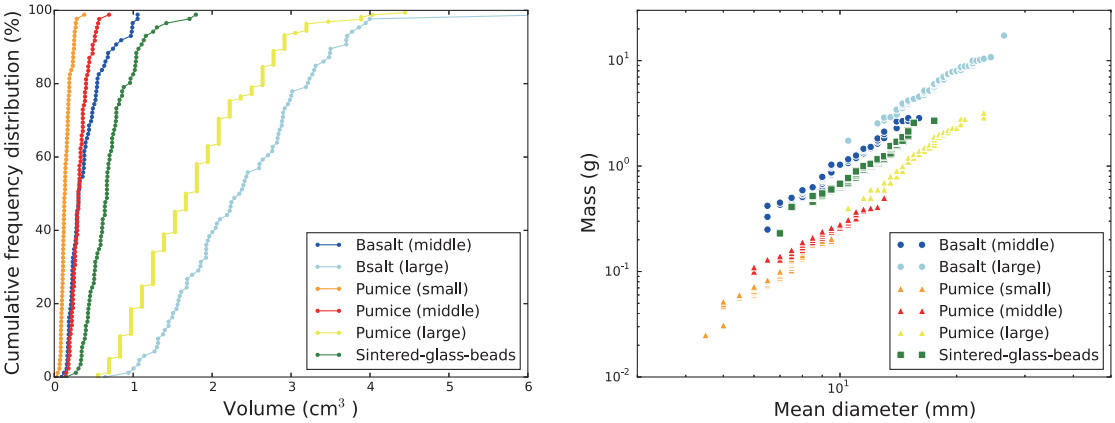

FIGURE 2.6: Size distributions of targets. (left) Cumulative frequency distribution of volumes of target grains. (right) Masses and mean diameters of target grains. $\sim$ 90 grains are randomly chosen from each targets.

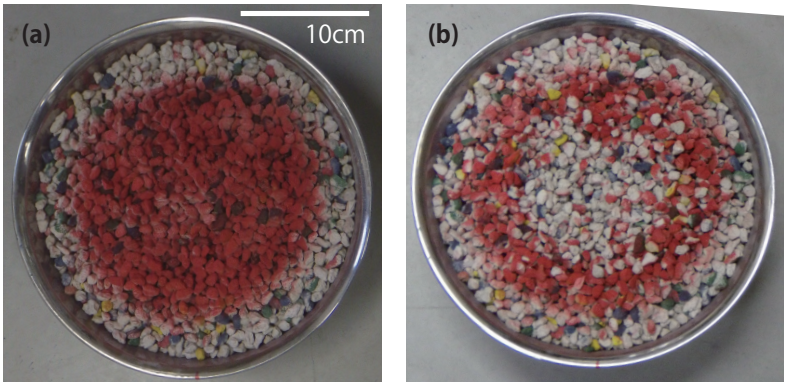

FIGURE 2.7: An example of pumice target with color-sprayed on the surface (a) before cratering and (b) after cratering.

2.5 Results

2.5.1 π_2 scaling

The impact conditions and resulting crater dimensions of all the cratering experiments in this study are given in Table 2.4. The crater sizes are plotted in π spaces (e.g. Holsapple, 1993) in Fig. 2.8 and 2.9. The definition of the π parameters used this stud is given in Sec. 2.3.1. Because the pi parameters are based on transient crater size not final crater size after post-impact modification processes, we used the proportional relationship between the transient crater and the final crater size for simple craters: $D_c = 1.18D_{\rm tr}$ (Chapman and McKinnon, 1986; Melosh, 1989).

If the mechanism of cratering on coarse-grained targets was same as the well-understood dry sand cratering, the results should follow the line for the dry sand gravity scaling, but many of our results show smaller size than the dry sand scaling line by Schmidt and Housen (1987) in Fig. 2.8. It is noted that the crater sizes for high impact energy or high impact velocity fall almost on the dry-sand scaling rule for the gravity regime. This result agrees with Holsapple and Housen (2014) at high velocity $\sim$ 5 km/s. At lower impact velocities, however, our experimental data indicate that cratering efficiency is significantly reduced. This might be caused by energy dissipation when the impactor hit and disrupted a target grain on uppermost surface.

2.5.2 π_3 scaling

Plotting the results on the π_3-π_V space reveals the effect of target material effective strength. Because the effective strength is combination of many factors as we mentioned, we cannot determined or measure the effective strength $\bar{Y}$ directly but corresponds to the bulk compression and tensile strength mainly. Thus, we chose widely used values for effective strength of dry soil ($\bar{Y} = 0.1$ MPa) and rocks ($\bar{Y} = 18$ MPa) fpr pir target grains when π_3 is calculated (Fig. 2.9). Interestingly, even the targets are considerably granular, the craters follows not the power-law index of the granular sand but

that of the monolithic rock, continuum material, although the effective strength of the targets are closer to the dry sand than the hard rock. Note that if the effective strength of rock is used for calculation of π_3, the values would shift toward larger values in π_3 (see, Fig. 2.9 (b)). Then, they would depart from the scaling line.

These results indicate that the coarse-grained targets behave similarly to dry sand during cratering processes for high velocity (> 5 km/s) impacts and coarse-grained targets behave as continuum material with very low mechanical strength much smaller than that of the constituting grains at moderate impact velocities (1 – 4 km/s). Impact processes for high-speed range might follow the sand gravity scaling because when the impact energy is sufficiently large, the energy dissipation by disrupted fragments is negligible compared with the energy to excavate the target. In contrast, impact processes at low velocities do not follow either the gravity or strength scalings of dry soils. Compared to the gravity scaling, the cratering effect is reduced to less than 0.1 times of the gravity scaling of dry sand. We note that in order to estimate crater retention ages of sub-km asteroids with coarse-grained surfaces, application formula to extrapolate the experimental results to real asteroid scale are needed. However, classic π-scaling could not explain cratering on coarse-grained surface. Thus, the results should be rearranged by another scaling.

TABLE 2.4: Experimental conditions and outcomes.

Exp. No.	Target material	Projectile mass m_p g	Impact velocity U m/s	Crater diameter D_c mm	Crater depth H mm
SGB001	Sintered-glass-beads	0.77	108	89 ± 5	20 ± 5
SGB002	Sintered-glass-beads	0.77	112	89 ± 6	23 ± 5
SGB003	Sintered-glass-beads	0.77	127	98 ± 8	26 ± 5
SGB004	Sintered-glass-beads	0.77	136	97 ± 5	24 ± 5
SGB005	Sintered-glass-beads	0.77	152	95 ± 12	29 ± 5
SGB006	Sintered-glass-beads	0.77	162	103 ± 5	28 ± 5
SGB007	Sintered-glass-beads	0.77	170	100 ± 5	25 ± 5
SGB008	Sintered-glass-beads	0.77	177	112 ± 12	33 ± 5
SGB009	Sintered-glass-beads	0.77	194	103 ± 6	33 ± 5
SGB010	Sintered-glass-beads	0.77	224	107 ± 8	28 ± 5
P001	Pumice-m	0.76	79	94 ± 11	18 ± 5
P002	Pumice-m	0.76	84	100 ± 15	16 ± 5
P003	Pumice-m	0.76	85	105 ± 12	16 ± 5
P004	Pumice-m	0.76	92	106 ± 11	18 ± 5
P005	Pumice-m	0.76	105	95 ± 7	26 ± 5
P006	Pumice-m	0.76	109	92 ± 13	24 ± 5
P007	Pumice-m	0.76	110	101 ± 14	20 ± 5
P008	Pumice-m	0.76	130	108 ± 12	17 ± 5
P009	Pumice-m	0.76	132	118 ± 7	19 ± 5
P010	Pumice-m	0.76	144	106 ± 10	19 ± 5
P011	Pumice-m	0.76	144	125 ± 14	16 ± 5
P012	Pumice-m	0.76	155	126 ± 32	18 ± 5

Continue on next page

continued from previous page

Exp. No.	Target material	Projectile mass m_p g	Impact velocity U m/s	Crater diameter D_c mm	Crater depth H mm
P013	Pumice-m	0.76	156	119 ± 12	21 ± 5
P014	Pumice-m	0.76	169	96 ± 15	19 ± 5
P015	Pumice-m	0.76	173	120 ± 21	20 ± 5
P016	Pumice-m	0.76	175	118 ± 11	18 ± 5
P017	Pumice-m	0.76	193	126 ± 15	25 ± 5
P101	Pumice-m	0.76	129	102 ± 5	24 ± 5
P102	Pumice-m	0.76	140	99 ± 5	25 ± 5
P103	Pumice-m	0.76	184	114 ± 5	29 ± 5
P104	Pumice-m	0.76	188	112 ± 5	27 ± 5
P105	Pumice-m	0.76	201	121 ± 5	27 ± 5
P106	Pumice-m	0.76	203	101 ± 5	25 ± 5
P107	Pumice-m	0.76	219	107 ± 5	40 ± 5
P201	Pumice-m	0.068	0.98×10^3	96 ± 11	18 ± 5
P202	Pumice-m	0.068	1.57×10^3	127 ± 14	24 ± 5
P203	Pumice-m	0.068	2.06×10^3	161 ± 14	34 ± 5
P204	Pumice-m	0.068	2.83×10^3	193 ± 17	32 ± 5
P205	Pumice-m	0.068	3.60×10^3	215 ± 13	44 ± 5
P206*	Pumice-m	0.068	4.33×10^3	240 ± 10	48 ± 5
P207	Pumice-m	0.068	5.05×10^3	280 ± 13	56 ± 5
P208*	Pumice-m	0.068	5.49×10^3	310 ± 10	58 ± 5
P209	Pumice-m	0.068	6.05×10^3	277 ± 16	51 ± 5
P301	Pumice-s	0.74	122	126 ± 6	-
P302	Pumice-s	0.74	132	139 ± 7	-
P303	Pumice-s	0.74	144	118 ± 5	-
P304	Pumice-s	0.74	152	124 ± 5	-
P305	Pumice-s	0.74	163	121 ± 5	-
P306	Pumice-s	0.74	165	131 ± 5	-
P307	Pumice-s	0.74	184	118 ± 16	-
P308	Pumice-s	0.74	186	131 ± 8	-
P401	Pumice-s	0.068	0.99×10^3	99 ± 10	17 ± 5
P402	Pumice-s	0.068	1.70×10^3	147 ± 14	32 ± 5
P403	Pumice-s	0.068	3.32×10^3	200 ± 28	42 ± 5
P404	Pumice-s	0.068	4.59×10^3	250 ± 19	49 ± 5
P405	Pumice-s	0.068	5.92×10^3	276 ± 11	64 ± 5
P501	Pumice-l	0.74	183	92 ± 12	23 ± 5
P502	Pumice-l	0.74	69	32 ± 7	8 ± 5
P503	Pumice-l	0.74	115	55 ± 5	14 ± 5
P504	Pumice-l	0.74	145	60 ± 20	15 ± 5
P505	Pumice-l	0.74	160	78 ± 12	20 ± 5
P601*	Pumice-l	0.068	0.96×10^3	110 ± 10	20 ± 5
P602	Pumice-l	0.068	1.78×10^3	130 ± 18	22 ± 5
P603	Pumice-l	0.068	3.15×10^3	163 ± 16	35 ± 5
P604	Pumice-l	0.068	4.43×10^3	206 ± 23	44 ± 5
P605*	Pumice-l	0.068	5.34×10^3	220 ± 10	53 ± 5
P606	Pumice-l	0.068	5.95×10^3	275 ± 19	66 ± 5
B001*	Basalt-m	0.068	0.88×10^3	108 ± 8	12.5 ± 5

Continue on next page

continued from previous page

Exp. No.	Target material	Projectile mass m_p g	Impact velocity U m/s	Crater diameter D_c mm	Crater depth H mm
B002*	Basalt-m	0.068	2.53×10^3	135 ± 5	38 ± 5
B003*	Basalt-m	0.068	4.30×10^3	240 ± 10	53 ± 5
B004*	Basalt-m	0.068	5.91×10^3	205 ± 5	48 ± 5
B005	Basalt-m	0.068	6.10×10^3	238 ± 8	43 ± 5
B101*	Basalt-l	0.068	4.21×10^3	190 ± 10	43 ± 5
B102*	Basalt-l	0.068	5.40×10^3	220 ± 10	55 ± 5

*Quarter-space experiments.

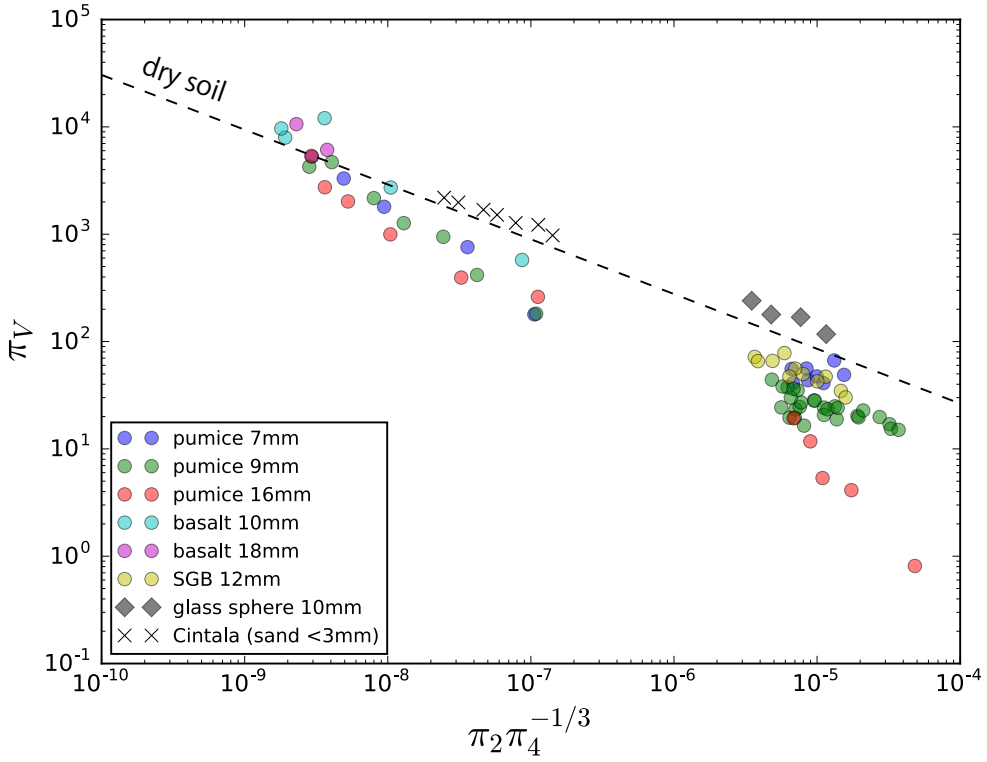

FIGURE 2.8: The π-scaling plot with $\pi_2 \pi_4^{-1/3}$ and π_V, compared with the empirical scaling line for dry sand (dashed) (Schmidt and Housen, 1987). If the mechanism of cratering on coarse-grained targets was same as the well-understood dry sand cratering, the results should follow the line.

2.5.3 Quarter-space experiments

The above experimental results suggest that the classic π scaling might not be satisfactory to explain the armoring. Detailed observations of cratering processes using quarter space experiments give us the hints for armoring processes. Figure 2.10 time-series images of a polycarbonate projectile impacting a pumice target at ~ 4.3 km/s

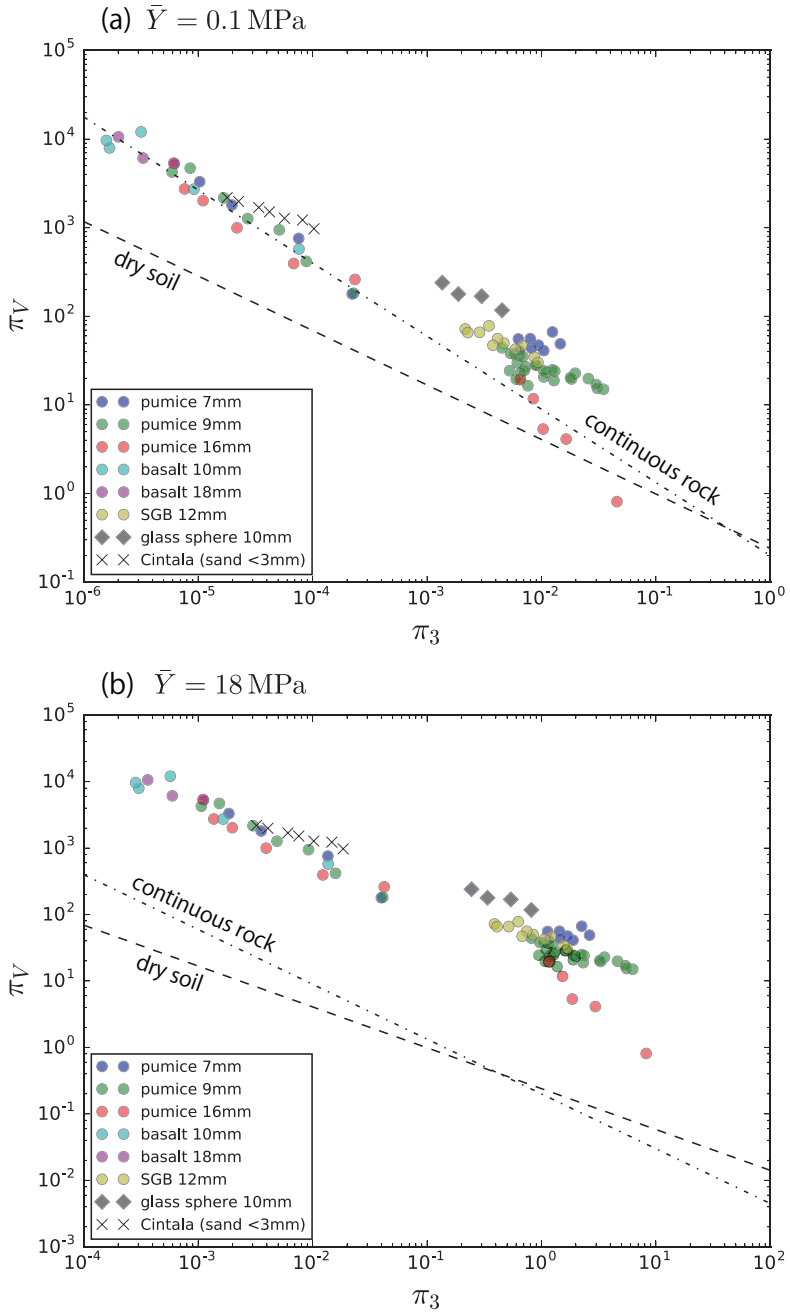

FIGURE 2.9: The π-scaling plot with π_3 and π_V assuming the effective strength of (a) $\bar{Y} = 0.1$ MPa and (b) $\bar{Y} = 18$ MPa. The experimental results are compared with the results for dry soil (dashed) and rock (one-dot) (Schmidt and Housen, 1987).

(P206). The images were background subtracted in order to visualize moved grains. Upon the contact between the impactor and a target grain at a high velocity, the flash of light occurs first because of extremely high shock pressure due to solid-to-solid collision (e.g. Sugita, Schultz, and Adams, 1998). As shock wave propagates, the very fast ejecta emerges. It is note that the grains did not move much. The shock wave in coarse-grained target is far slower than that within the rigid targets which usually have shock wave velocity on the order of km/s. Because fragments in the very fast ejecta are fully fractured, they do not have size large enough to be measured. We could see that the fragmentation of target grains occurred in the very vicinity of the impact site, agreeing with the simulation results by (Barnouin-Jha, Cintala, and Crawford, 2002). After fracture stage, the momentum transfer triggers subsequent excavation flow. The unfractured grains move along the excavation flow in a very similar fashion as the flow of the gravity-dominated simple crater. However, the ejecta speed was extremely slow compared with the excavation flow in fine-grained sand targets. The excavation stage appears virtually uninfluenced by the material strength of constituent grains, but might be controlled by the friction between grains as dry sand. In the excavation stage, because target grains were not fractured in the flow field macroscopically, the material strength of each grain may not be very important. These observations suggest that the material strength of constituent grains may influence only the compaction and fracture stage of cratering. The very first stage of cratering, where momentum is transferred from the impactor to the contacted grain and initiate the excavation field, is influenced directly by mechanical strength of target grains.

Figures 2.11 and 2.12 exhibit the final craters and the measurements by the laser profiler. For low impact energies, crater shapes deviate from simple craters; irregular shapes (Fig. 2.11 (a), (b)). This observation may be explained if the excavation flow dose not develop fully because the low energy is dissipated mostly by the disruption of the first contacted grain. For large impact energy impacts, the shapes very similar to simple craters (Fig. 2.11 (c), Fig. 2.12).

2.6 Discussions

2.6.1 Extension of the π scaling

The above results in this study and previous studies (Fig. 3.6) strongly suggest that the crater volume on the coarse-grained targets would be influenced by target disruption energy for unit mass Q_D^* (e.g. Benz and Asphaug, 1999), the target material density δ_t and the target grain radius $r_t = L/2$ as well as other parameter used in the classic π scaling ,such as projectile diameter a, impact velocity U, projectile density ρ_p, target bulk density ρ_t, target strength Y, and surface gravity g, in Sec. 2.3.1. Thus, we deduce the π scaling, starting from the following equation instead of eq. (2.2):

$$V_c = f^*[a,\, U,\, \rho_p,\, \rho_t,\, Y,\, g,\, Q_D^*,\, \delta_t,\, r_t]. \tag{2.12}$$

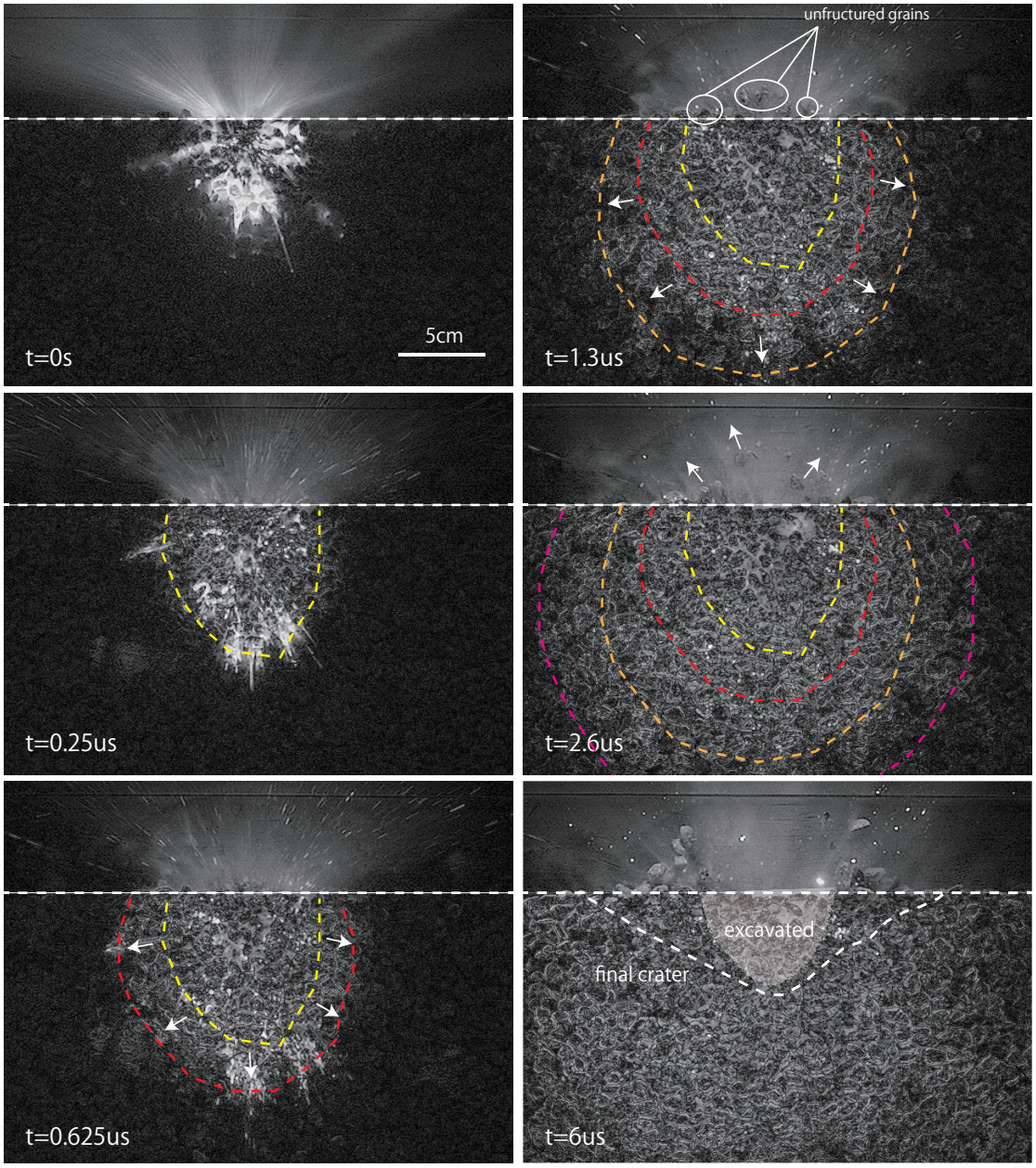

FIGURE 2.10: Background-subtracted time series of a polycarbonate ($a = 2.38$ mm) impact on a pumice target with ~ 9 mm in mean diameter at ~ 4.3 km/s of velocity (P206). Note that these images are background-subtracted images; grains that have moved from the pre-impact conditions are seen.

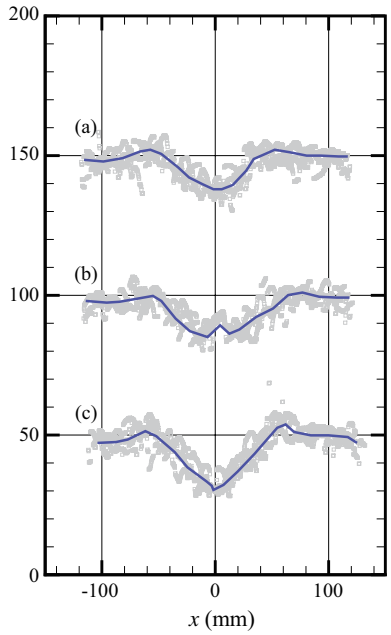

FIGURE 2.11: Crater profiles for low energy experiments. Target grains are pumice blocks with the diameter of ~ 9 mm. (a) P001, $m_p = 0.76$g, $U = 79$m/s, (b) P010, $m_p = 0.76$g, $U = 144$m/s, (c) P017, $m_p = 0.76$g, $U = 193$m/s.

Note that $\rho_t = \phi\delta_t$,where ϕ is the bulk porosity of target. Then, other three dimensionless parameters are automatically derived by the dimensional analysis:

$$\pi_5 = \frac{Q_D^*}{U^2}, \tag{2.13}$$

$$\pi_6 = \frac{r_t}{a}, \tag{2.14}$$

$$\pi_7 = \frac{\delta_t}{\rho_p}. \tag{2.15}$$

The ξ and ψ are the ratio of impact energy to the disruption energy of a target grain and the size ratio of projectile to target grains. They are given as the combinations of these π parameters:

$$\xi = \frac{1}{2}\pi_5^{-1}\pi_6^{-3}\pi_7^{-1}, \tag{2.16}$$

$$\psi = \pi_6^{-1}. \tag{2.17}$$

Because the dimensional analysis suggests the phenomena can be parameterized by those seven parameters if the phenomena is controlled by the physical properties in eq. (2.12), it is reasonably that the grain disruption energy ratio ξ and the projectile target grain size ratio ψ could describe the cratering on coarse-grained targets.

The observations of the quarter-space experiments in Sec. 2.5.3 suggest that the fracturing stage and the excavation should be considered separately. More specifically,

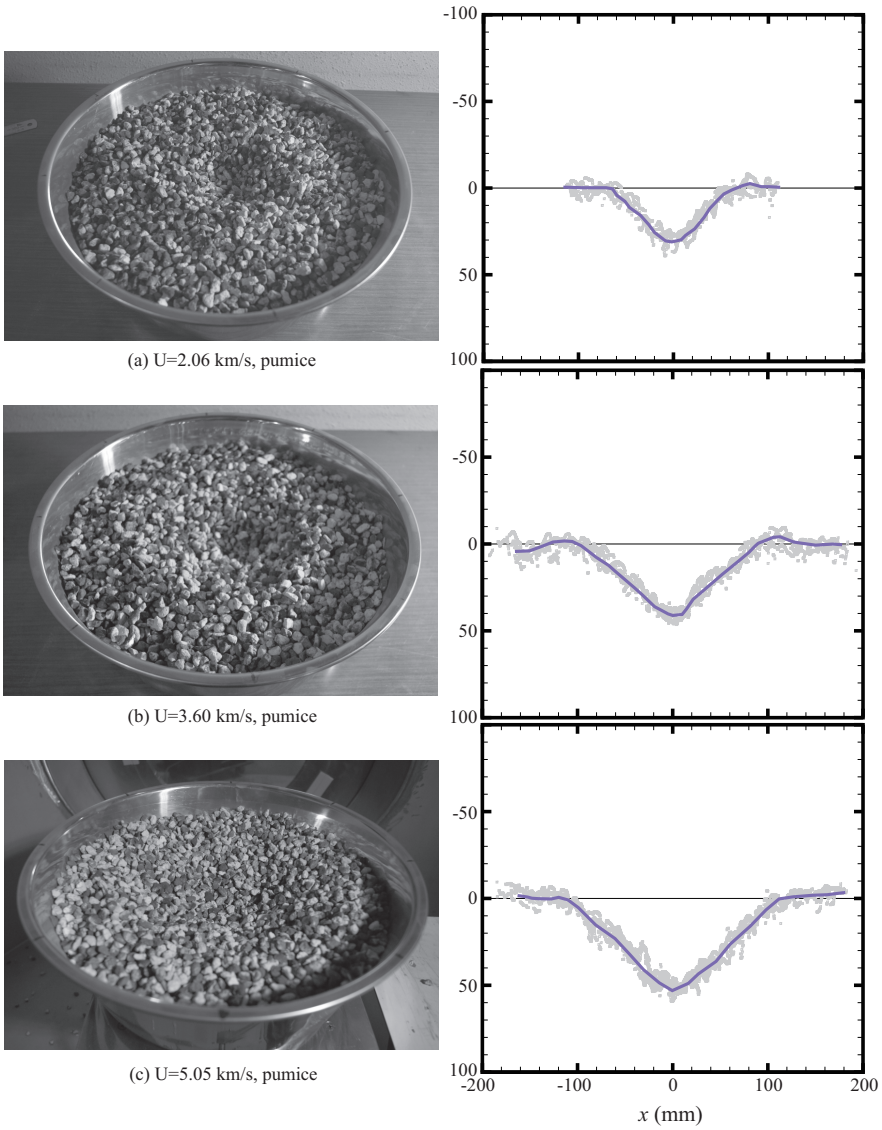

FIGURE 2.12: Craters formed in high energy experiments and their profiles. Target grains are pumice blocks $\sim$ 9 mm in diameter. (a) P203, $m_p = 0.068$ g, $U = 2.06$ km/s, (b) P205, $m_p = 0.068$ g, $U = 144$m/s, (c) P207, $m_p = 0.068$ g, $U = 5.05$ km/s.

because the flow in the excavation stage is similar to the simple crater, modification of the point source in the fracture stage would explain difference of the outcome from the granular sand. As is suggested by Güttler, Hirata, and Nakamura (2012), the final crater diameter might be influenced by the mass ratio of the impactor to the target grain through the momentum conservation law upon impact. Note that the energy conservation is not necessary because it can be lost due to various dissipation processes. Assuming that the impacted target grain move together in a group even after fractured, the velocity of the contacted target grain would be

$$U^* = \frac{(1+\epsilon)}{1+m_t/m_p}U = \Pi U, \tag{2.18}$$

where the coefficient of restitution ϵ . If the target impacted grain and the impactor move together after the collision, the coefficient of restitution is 0, a perfectly inelastic collision. We can assume the $\epsilon \sim 0$ because the target grain would not move faster than the impact velocity immediately after the collision. Thus, cratering on coarse-grained surface should use another coupling parameter C^*:

$$\begin{aligned} C^* &= a^* U^{*\mu} \rho_p^{\nu} \\ &= \Pi^{\mu-1/3} C, \end{aligned} \tag{2.19}$$

where $a^* = a\Pi^{-1/3}$ is the effective impactor diameter. When the size ratio ψ only affect the crater size only through Π, the π scaling for coarse-grained target would be expressed as

$$\begin{aligned} \pi_V^* &= \frac{\rho_t V_c}{(m_p+m_t)} = \mathcal{F}^*[C^*(\Pi), \pi_2^*(\Pi), \pi_3^*(\Pi), \xi(\pi_5,\pi_6,\pi_7), \pi_4], \\ \Pi &= \frac{m_p}{m_p+m_t} = \frac{1}{1+\pi_6^3\pi_7}, \\ \pi_2^* &= \frac{a^* g}{U^{*2}} = \Pi^{-7/3}\pi_2, \\ \pi_3^* &= \frac{\bar{Y}}{\rho_t U^{*2}} = \Pi^{-2}\pi_3, \\ \xi &= \frac{m_p U^2/2}{m_t Q_D^*} = \pi_5^{-1}\pi_6^{-3}\pi_7^{-1}/2 \\ \pi_4 &= \frac{\rho_t}{\rho_p}. \end{aligned}$$

Plotting with these new derived parameters, we obtain the graphs in $\pi_2^* - \pi_V^*$, $\pi_3^* - \pi_V^*$ and $\xi - \pi_V^*$ spaces (Figs.2.13–2.15). Here, we compile our results with the previous results from Güttler, Hirata, and Nakamura (2012) and Holsapple and Housen (2014). When impact energy is too small, i.e., $\xi < 1$, only one or few target grains were fractured or one grain was cratered (Güttler, Hirata, and Nakamura, 2012). However, high

energy impacts appear to follow the formulation using new scaling parameters:

$$\pi_V^* = K_1 \left[\pi_2^* \pi_4^{-1/3} + \pi_3^{*(2+\mu)/2} \right]^{-3\mu/(2+\mu)}, \tag{2.20}$$

where, $K_1 = 0.24$, $\mu = 0.41$ and the effective strength $\bar{Y} \sim 0.1$ MPa. Note that the effective strength is much smaller than the composed material strength such as basalt and soda glass and is comparable to the strength of bulk sand. Thus, the new scaling law yields to the new gravity scaling and the strength scaling as follows,
gravity dominated:

$$\begin{aligned} V_c &= K_1 \left(\frac{m_p + m_t}{\rho_t} \right) \left(\frac{g a^*}{U^{*2}} \right)^{-3\mu/(2+\mu)} \left(\frac{\rho_t}{\rho_p} \right)^{\mu/(2+\mu)}, \\ &= K_1 \left(\frac{m_p}{\rho_t} \right) \Pi^{(6\mu-2)/(2+\mu)} \pi_2^{-3\mu/(2+\mu)} \pi_4^{\mu/(2+\mu)}. \end{aligned} \tag{2.21}$$

material strength dominated:

$$\begin{aligned} V_c &= K_1 \left(\frac{m_p + m_t}{\rho_t} \right) \left(\frac{\bar{Y}}{\rho_t U^{*2}} \right)^{-3\mu/2}, \\ &= K_1 \left(\frac{m_p}{\rho_t} \right) \Pi^{3\mu-1} \pi_3^{-3\mu/2}. \end{aligned} \tag{2.22}$$

It should be noticed that $m_p \gg m_t$ leads to the common π scaling in Sec. 2.3.1. The experimental results are well fitted with the gravity sand scaling in Fig.2.13 in high velocity, i.e., small π_2^* and with the strength scaling of very weak material such as weak rock and dry soil in low velocity, where they are still scattered but this appears to be better fitting than the classical scaling. Thus, the new coupling parameter C^* might represents the point-source of cratering on coarse-grained targets.

Figure 2.15 shows that data follow a single line for each material (glass-beads, pumice, basalt and sintered-glass-beads) over the entire velocity range from 0.2 to 5 km/s and that their slopes are approximately the same. This result strongly suggests that the disruption energy ratio ξ and π_V^* are better parameters to characterize material strength than π_3^*. Moreover, excepting the sintered-glass-beads results, the lines can be categorized into two groups: the angular shaped grains and the smooth (spherical) shaped grains. This difference might result in the difference in K_1, but this hypothesis needs further consideration. In addition, $\xi - \pi_V^*$ space suggests that the armoring effect could be classified into three regimes by its mechanism: (1) the gravity scaling (no armoring): $\psi > 1$ or $\xi \gtrsim 10^4$, (2) the armoring range I involving disruption of target grains: $\psi \lesssim 1$ and $1 \lesssim \xi \lesssim 10^4$, (3) the armoring range Ⅱ without heavy disruption of target grains: $\phi \lesssim 1$ and $\xi < 1$.

Finally, we can rescale the cratering on coarse-grained targets as follows: high velocity impacts (no armoring) follow the new gravity scaling of $\pi_2^* - \pi_V^*$ and less energetic impacts (armoring I) may follow the new strength scaling of $\pi_3^* - \pi_V^*$ or more

likely $\xi - \pi_V^*$. Thus, we obtain the reduction in cratering efficiency, when the energy ratio $\xi > 1$.

$$\chi_V = \pi_V^*/\pi_V = \begin{cases} \Pi^{(6\mu-2)/(2+\mu)} & \text{(gravity regime)} \\ \Pi^{3\mu-1} & \text{(strength regime)} \end{cases}. \tag{2.23}$$

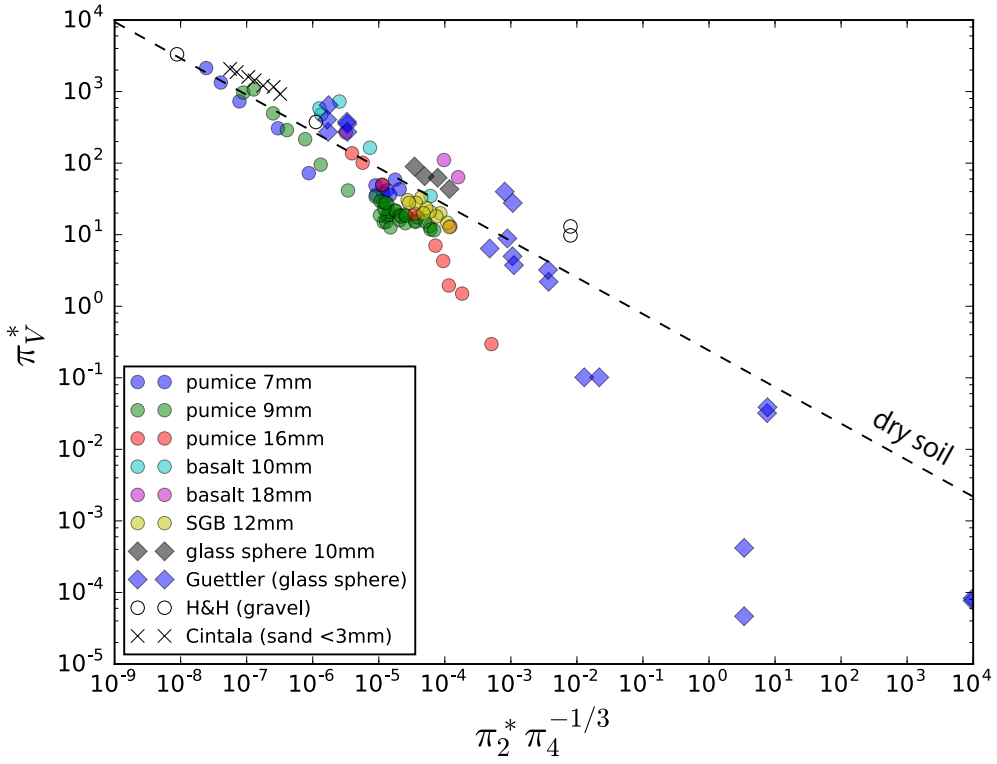

FIGURE 2.13: The new scaling law in the $\pi_2^* - \pi_V^*$ space, compiling with the previous data by Cintala, Berthoud, and Hörz (1999), Güttler, Hirata, and Nakamura (2012) and Holsapple and Housen (2014).

2.6.2 Energy leaking

Even when impact energy is much larger than catastrophic disruption energy for one grain (i.e., $\xi \gg 1$), the cratering efficiency increases with impact velocity. However, impact energy is comparable to the disruption energy for one grain (i.e., $\xi \sim 1$), crater sizes have great scatter. This might be caused by energy leak contact points among grains. If there is no grain to touch the first contacted grain, the collision between the impactor and the grain is completely the same as the disruption experiments for an isolated target body. In other words, the first contacted grain would be disrupted catastrophically when $\xi \sim 1$. However, because in reality the first contacted grain possesses many contact points with neighboring grains, shock wave will transmit to neighboring grains (Fig. 2.16). The mean coordination number of random packing of hard

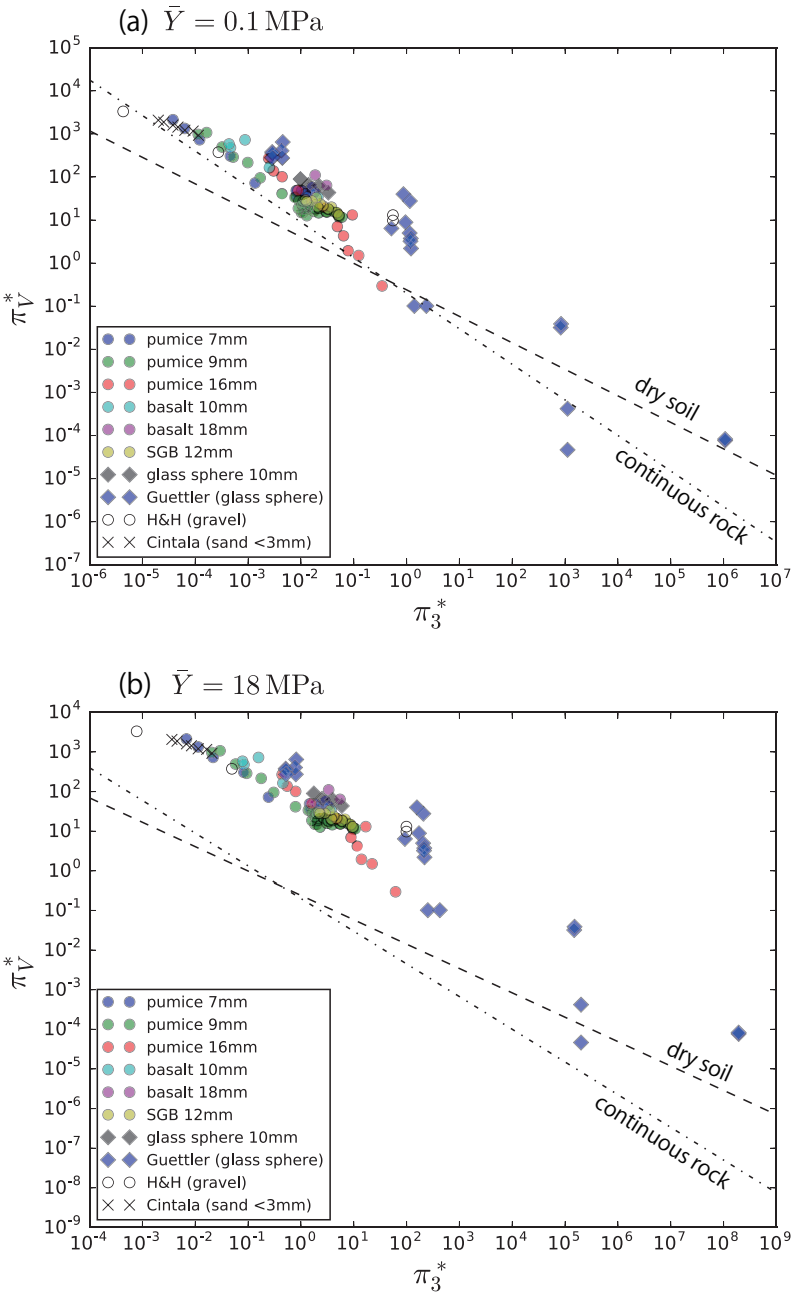

FIGURE 2.14: The new scaling law in the $\pi_3^* - \pi_V^*$ space, compiling with the previous data by Cintala, Berthoud, and Hörz (1999), Güttler, Hirata, and Nakamura (2012) and Holsapple and Housen (2014). We assumed that the effective strength of (a) $\bar{Y} = 0.1$ MPa and (b) $\bar{Y} = 18$ MPa.

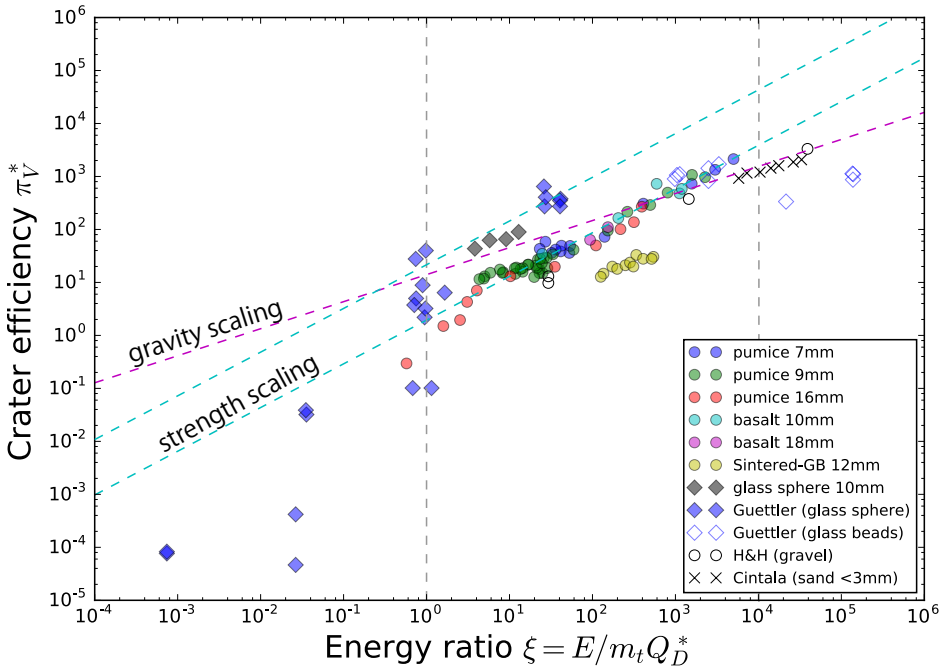

FIGURE 2.15: Experimental results in ξ-π_V^* space. The data are sorted in two lines: one is angular materials and another is spherical material. When the energy ratio $\xi < 1$, only few grains were shuttered or a crater hole was made on a grain (Güttler, Hirata, and Nakamura, 2012).

spheres is estimated to be approximately 6 from both experiments and simulations (e.g. Scott and Kilgour, 1969; He, Ekere, and Cai, 1999). It is well known that closest packings of equal spheres, hexagonal close-packing and cubic close-packing, have the maximum coordination number of 12. Note that non-spherical grains can be touched even more neighboring grains. Assuming that the contacted grain immediately move to the same direction with the neighbors, the effective energy for the contacted grain would be $\sim 1/6$ for randomly packed spheres. This might explain leaking of energy from the contacted grain to the surrounding grains and the effective energy for disruption would be depleted by $\sim 1/6$. This means scattering around $\xi \sim 1$ might be caused by this mechanism.

There is another experimental result shows the energy leaking to neighbors. Durda et al. (2011) conducted impact experiments to both a block resting on sand and a block buried in sand. Even the impact energy was comparable to the catastrophic disruption of the blocks, the damage of the buried blocks were much less than the block rested on a sand surface. Furthermore, the block rested on a sand surface was not fully disrupted though a block suspends in space would be catastrophically disrupted at this level of impact energy. As the touching area of the sand and the block increased, the damage decreased. This observation supports energy leaking to surrounding sand grains. Thus, the effective energy to the first contacted grain would be ~ 6 time smaller than the impactor kinetic energy. The border between the armoring zone I and the armoring zone II could shift to several time larger.

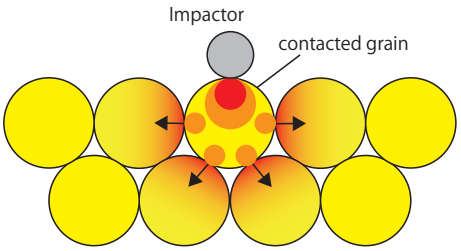

FIGURE 2.16: The schematic image of the energy leaking.

2.6.3 Implication for Itokawa crater retention age

Michel et al. (2009) first estimated the crater age of Itokawa based on two kinds of strength crater scaling, assuming a basalt and a relatively soft rock, and obtained the age as old as 75 Myr – 1 Gyr. However, Itokawa is most likely a rubble-pile asteroid, which is weakly gathered with gravity and cohesion. Our experiments suggest the crater size was much greater than the crater size on a monolithic body, although the armoring may influence crater size significantly depending on the disruption energy ratio ξ. Whenever cratering involving boulder disruption, our results would predict that crater size on Itokawa would be closer to the gravity scale of sand rather than the soft rock strength scaling used by Michel et al. (2009). This suggests the real Itokawa surface age would be much younger than that values by Michel et al. (2009). Thus, we revisited the Itokawa crater retention age estimate using the distribution of the larger crater-like features > 100 m.

For Itokawa, we took the parameters as the bulk density of Itokawa $\rho_a = 1900$ kg/m^3, the impact velocity in the main belt $U = 5.3$ km/s, and the surface gravity $g = 7.5 \times 10^{-5}$m/s^2. Note that the impactor ~ 1.8 m can catastrophically disrupt the 40 m-sized boulder, the maximum size on Itokawa, with this impact velocity. When we see any crater on Itokawa, that indicates the collision $\xi > 1$ happened, otherwise we cannot see any crater $\xi < 1$. We take the characteristic boulder size of 2 m because $P(> 2\mathrm{m}) \sim 0.5$ which means the probability for impactors to hit the surface boulders larger than 2 m is approximately 50 % on Itokawa. Assuming that the Itokawa surface is covered by the characteristic-sized boulder uniformly, we obtain the efficiency reduction coefficient χ_V as:

$$\chi_V = \begin{cases} (1 + (2/D_p)^3)^{-(6\mu-2)/(2+\mu)} & (D_p \gtrsim 1.8\mathrm{m}) \\ (1 + (2/D_p)^3)^{-3\mu+1} & (0.04\mathrm{m} \lesssim D_p \lesssim 1.8\mathrm{m}), \end{cases} \tag{2.24}$$

where, the density of projectile is comparable to the bulk density of a target, i.e., $\rho_p \sim \rho_t$. We choose the average intrinsic collision probability $P_I = 2.86 \times 10^{-18}$ km^{-2} yr^{-1} in the main belt (Bottke et al., 1994) for Itokawa. Although Itokawa is at the near-Earth orbit now, the cratering history reflects the main-belt impacts due to the short dynamical lifetime (i.e., several million years) in the near-Earth orbit. In addition the number of objects are $\sim 1/1000$ times that in the main belt (Stuart and Binzel, 2004). Assuming

that Itokawa is a spherical body with $D_{\rm Ito} = 0.326$km, the frequency that the projectile with D_p in diameter hits Itokawa is

$$p_{\rm Ito}(D_p) = P_I(D_{\rm Ito} + D_p)^2 n_a(D_p)/4, \tag{2.25}$$

where $n_a(D)$ is the number of MBAs with diameter D, and $n_a(D) = {\rm d}N_a(> D)/{\rm d}D$ in definition. Then the possibility that the projectile larger than D_p in diameter hits Itokawa is,

$$\begin{aligned}\mathcal{P}_{\rm Ito}(> D_p) &= P_I(D_{\rm Ito} + D_p)^2 N_a(> D_p)/4 \\ &\sim P_I D_{\rm Ito}^2 N_a(> D_p)/4, \qquad (\because \quad D_{\rm Ito} \ll D_p).\end{aligned} \tag{2.26}$$

Based on the numerical simulation by O'Brien and Greenberg (2005), the number distribution of the small asteroids in the main belt had been estimated because they are too small to be observed directly from the Earth. The slope for number distribution for small asteroids is slightly steeper than that for large asteroids. O'Brien and Greenberg (2005) estimated the cumulative number distribution of the small asteroids in the main belt as

$$N_a(> D) = N_0 D^\alpha = 1.85 \times 10^{13} D^{-2.91}, \qquad (1 < D < 100{\rm m}). \tag{2.27}$$

Thus, the time interval that the impactor larger than D_p hits Itokawa can be calculated as $\Delta\tau = 1/\mathcal{P}_{\rm Ito}(> D_p)$.

$$\Delta\tau(> D_p) = \frac{4}{P_I D_{\rm Ito}^2 N_0 D_p^\alpha}, \tag{2.28}$$

using the non-linear relationship of the impactor and the formed crater including the cratering efficiency reduction:

$$D_c = \chi_V^{1/3} \left[4\pi_V \left(\frac{\rho_p}{\rho_t} \right) \right]^{1/3}, \tag{2.29}$$

which is shown in Fig. 2.17. Larger craters could be retained long time from Itokawa formation age, while smaller ones could be modified or removed easily. On the Itokawa surface, the five largest circular depressions with > 100 m in diameter were observed (Hirata et al., 2009). The minimum age is derived from the gravity scaling of dry sand and the maximum age is from the scaling involving armoring. The crater with the diameter of 100 m yields $D_p \sim 0.7 - 1.4$ m, which corresponds to $\Delta\tau \sim 0.3 - 1.9$ Myr. We can estimate the timescale to accumulate five craters multiplying by five. If they were resulted from impacts, we can estimate the time to accumulate such five large craters without any crater erasure process as long as $5 \times \Delta\tau \sim 0.7 - 14$ Myr including the statistical error.

If the craters were formed in the present orbit, it would take unrealistically longer time. Thus, this crater retention age would be the time in the main-belt region. In other words, even if there were tidal effect during possible encounter(s) with Mars

and/or Earth, the tidal force have not been able to modify drastically or erase the formed craters. Otherwise, Itokawa possibly did not experience any encounter with terrestrial planet involving global resurfacing for a few million years.

Our cratering retention age estimate (0.7 – 14 Myr) is much younger than the previous age estimate (75 Myr – 1G yr) based on the strength scaling for rigid bodies by Michel et al. (2009). Furthermore, the age is rather close to the cosmic ray exposure (CRE) ages of < 8 Myr and ~ 1.5 Myr (Nagao et al., 2011; Meier et al., 2014), the galactic cosmic ray exposure age of $> 3 - 4$ Myr (Nishiizumi, Caffee, and Welten, 2015) and the spectral age < 10 Myr (Koga et al., 2014; Bonal et al., 2015). It should be noted that the CRE ages and the spectral age are estimated for the present orbital stage of Itokawa; they could be several times longer in the main belt because of weaker solar wind there. Taking into account the effect of the distance from the Sun, the CRE ages and the spectral age indicate the same order of ages. Thus, the our crater retention age and the CRE ages may reflect the latest disruption or global resurfacing age of Itokawa, which might have experienced disruption several times because of its short collisional life time with its small size (e.g. O'Brien and Greenberg, 2005). Moreover, since the crater might be preserved from its formation, crater modification by regolith migration appears not too strong to erase larger craters completely, although smaller ones might be influenced as Miyamoto et al. (2007) suggests the fine regolith movement on the Itokawa surface.

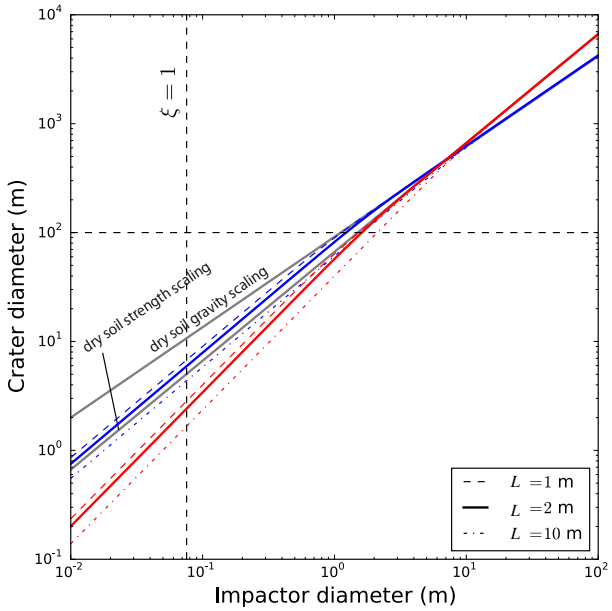

FIGURE 2.17: Crater diameters on Itokawa calculated from eq. (2.24). Gray lines are the classic π scaling (e.g. Holsapple, 1993) and colored lines are proposed scalings in this study with different target grain sizes (L). The colored lines approach to the classic scalings with increasing projectile diameter.

2.6.4 Implications for dynamical evolution of the asteroid main belt.

The size frequency distribution (SFD) of MBAs have evolved by innumerable collisions. Excavation and disruption due to mutual collisions grind asteroids to smaller sizes. A recent theoretical calculation showed this collisional cascade is controlled mainly by cratering (small impacts) rather than catastrophic disruption (large impacts) on collisions (Kobayashi and Tanaka, 2010). Thus, the small asteroids cratering efficiency is very important because the efficiency can change the size frequency distribution of smaller asteroids. Furthermore, smaller asteroids may play as projectiles to the larger asteroids and control the grinding rate of the larger asteroids.

Our experiments strongly suggest that large craters ($D_c > 100$ m) is not influenced by mechanical strength of surface grains; cratering efficiency reduction coefficient $\chi_V \sim 1$. Crater volume of gravity scaling than the crater volume on monolithic bodies. Small asteroids easily lose there masses due to small escape velocities, for example the escape velocity of Itokawa is less than 1 m/s and the most of ejecta wouldn't come back to the body. Crater excavated volume on rubble-piles could be larger by order of magnitude than that on monolithic bodies. This leads to the erosion rate much higher than the estimate in Kobayashi and Tanaka (2010). Thus, the SFD evolution of MBAs might be influenced by inner structure of asteroids. The effective erosion by cratering suggests the high mass loss rate for small asteroids which perform a role as projectiles for larger asteroids. The fast depletion of the small asteroids might result in long-lived large asteroids.

2.7 Conclusions

Many small asteroids are supposed to have rubble-pile structures and relatively coarse surfaces. The gravitational aggregates would behave like continuum medium if the target is very smooth. In reality, however, the surface is covered by large boulders which was observed on Itokawa (Saito et al., 2006; Miyamoto et al., 2007). To understand the cratering mechanism on such boulder-rich surfaces and to evaluate the cratering efficiency, we conducted impact experiments on coarse-grained targets with four kinds of materials, pumice, basalt, soda glass, and sintered-glass-beads. We measured the diameter and depth of craters and found both the size ratio $\psi = D_p/L$ of the impactor to the target grain and the energy ratio $\xi = \frac{1}{2}m_p U^2/Q_D^* m_t$ of the impact energy to the disruption energy of the target grain are important in understanding cratering efficiency reduction, so-called armoring effect. The armoring effect could be classified into three regimes: (1) the gravity scaling (no armoring): $\psi > 1$ or $\xi \gtrsim 10^4$, (2) the armoring range I involving disruption of target grains: $\psi \lesssim 1$ and $1 \lesssim \xi \lesssim 10^4$, (3) the armoring range II without disruption of target grains: $\phi \lesssim 1$ and $\xi < 1$. The armoring comprises two stages, the fracture stage and the excavation stage. The grain disruption stage completes during the very early time in the impact process; the subsequent excavation stage occurs after the disruption and its flow field appears similar to that

of simple crater formation. This observation suggests that the impactor/target size ratio and disruption strength affects only the fracture stage and the modification of the "coupling parameter" to widely used π scaling (Holsapple, 1993) leads to a good fit to our experiment data for coarse-grained targets over a wide range of impact velocities. The modified coupling parameter is calculated from the momentum transfer between the impactor and the contacted grain. The cratering efficiency is larger than half of the efficiency of the gravity scaling whenever the impactor kinetic energy is higher than the disruption energy of the first-contact target grain. Note that a impactor at the average impact velocity in the main asteroid belt catastrophically disrupt a surface grain more than 20 times its own size. Consequently, the armoring effect may not be effective for larger craters, which might be caused by the much larger impact energy than the boulder disruption energy. Thus, when the number density of larger impact craters may not be influenced very much by armoring effect. A gravity scaling may apply for these craters.

Crater retention age of the Itokawa surface on new scaling rule for coarse-grained surface is $0.7 - 14$ Myr, which is much younger than the previous estimated age (75 Myr – 1 Gyr) based on strength scaling rules (Michel et al., 2009). Our age estimate is the accumulation age of five craters > 100 m in the main-belt region, assuming no crater erasure occured. It is noted that forming this many 100 m class craters on in the near-Earth is almost impossible because of its short dynamical lifetime. Thus, the obliteration of craters due to tidal force would be less likely on Itokawa, because this would require even longer residence time of Itokawa in the near-Earth orbit. Moreover, this age is in good agreement with the CRE ages by Nagao et al. (2011) and Meier et al. (2014), the galactic cosmic ray exposure age by Nishiizumi, Caffee, and Welten (2015) and the spectral age by Koga et al. (2014). These lines of evidence strongly suggest that Itokawa may have experienced the global resurface event in its recent history on the order of 10 Myr.

Chapter 3

Crater retention age of Itokawa: Monte Carlo simulation

3.1 Introduction

The possibly features caused by impacts on 25143 Itokawa were observed by the Hayabusa spacecraft, and Hirata et al. (2009) determined the possible impact morphologies. 38 candidates which showed widely diverse in morphologies were identified. If those features were formed by impacts, the crater distribution on Itokawa shows nearly the empirical saturation for larger craters $\gtrsim 100$m, however the smaller craters are far less observed than the saturation level (Fig. 3.1). There are possible reasons for the depletion of the number of small craters: the depletion of small impactors, the crater production rate depletion by armoring, and the excess in crater erasure efficiency. However, the major mechanism to cause the depletion is not revealed yet. We examine those possible effects through the Monte Carlo simulations. Before going into the calculations, the mechanisms are reviewed. The armoring process have been discussed in Chapter 2, we discuss other two possible processes to explain the absence of small craters on Itokawa in following subsections.

3.1.1 Impactor size distribution

Asteroid population in the main belt

The main source of impactors, that cause craters on the surfaces of main-belt asteroids (MBAs), might be other smaller main-belt asteroids. The population of small MBAs ($\lesssim$ 3km) can not be directly determined because they are too small for the detection levels of grand-based observations. Thus, populations of smaller asteroids in the main belt have been estimated by the N-body numerical calculations (Bottke et al., 2005; O'Brien and Greenberg, 2005). They resulted in similar distributions with slightly different slopes (Fig. 3.2).
Bottke et al. (2005) model ($0.1 < D_a < 100$m):

$$\text{(MBAs)} \qquad N_a(> D_a) \sim 1.28 \times 10^{13} D_a^{-2.58}, \tag{3.1}$$

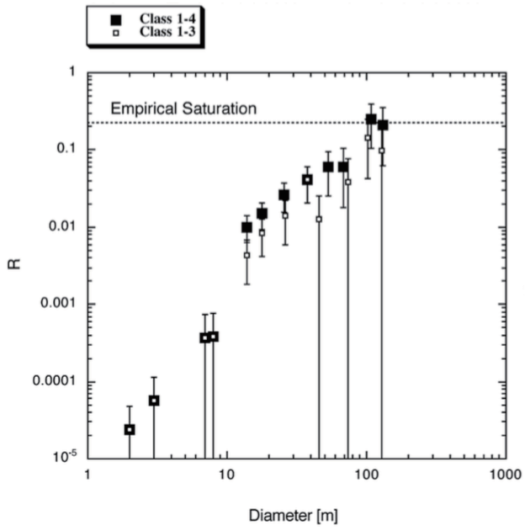

FIGURE 3.1: The crater-like feature size frequency distribution of Itokawa. The R indicates the differential size frequency divided by D^{-3} (Crater Analysis Techniques Working Group, 1979). The circular depressions which are supposed to be impact induced craters with high confidence were labeled as class 1 and those with low confidence were labeled as class 4. (From Hirata et al. (2009))

O'Brien and Greenberg (2005) model ($10 < D_a < 100$m):

$$\text{(MBAs)} \qquad N_a(> D_a) \sim 1.30 \times 10^{13} D_a^{-2.94}, \tag{3.2}$$

where D_a (m) is asteroid diameter.

Asteroid population in the near-Earth orbit

Most NEAs are considered to come from the main belt through resonances where large planets perturb asteroids. In the near-Earth orbit smaller asteroids can be detected because of closer approaches to the Earth than MBAs. Specifically NEOs of ~ 10 m in diameter can be detected, in contrast of the detection limit at a few km in the main belt. From LINEAR survey, the population of NEOs was derived by Stuart and Binzel (2004) with correction of albedo bias. Lunar crater record showed the good fit to this model over crater diameters from 2 to ~ 100 km. The population of NEOs is supposed to be ~ 1000 times less than MBAs (Stuart and Binzel, 2004; Bottke et al., 2005). Considering NEOs come from the main belt, if NEOs are resulted from random sampling of MBAs, the slope of NEO distribution might have similar value as MBAs. Comparing the slope of smaller asteroids in the main belt of ~ -2.94 to -2.58 and the near Earth of ~ -1.95 raises significant difference. This gap is try to explained by the Yarkovsky effect hypothesis, which acts effectively for smaller asteroids to move in radial direction (Bottke Jr. and Vokrouhlický, 2006). However, note that there is still an uncertainty in the population of the smaller asteroids.

Stuart and Binzel (2004) observation of NEOs (100m$< D_a <$ 10km):

$$\text{(NEOs)} \qquad N_a(> D_a) \sim 7.71 \times 10^8 D_a^{-1.95}. \tag{3.3}$$

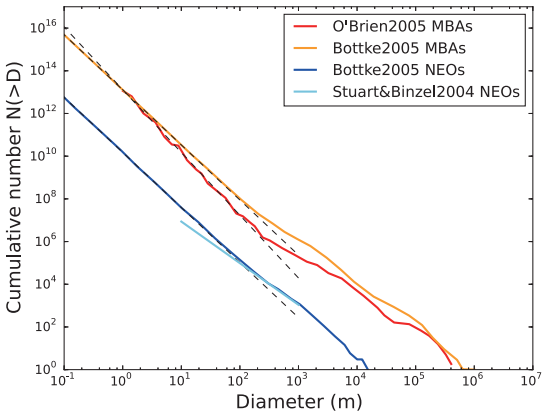

FIGURE 3.2: The estimated population of MBAs and NEOs. The dashed lines are fitted lines. The number of NEOs is ~ 1000 times smaller than MBAs.

3.1.2 Crater erasure process - Seismic shaking

Especially for small bodies, impact-induced seismic shaking would cause degradation and erasure of craters. Seismic effect by large impacts forming complex craters had been recognized on the Moon (Schultz and Gault, 1975). Seismic shaking on asteroids was also suspected on 951 Gaspra, 243 Ida and 433 Eros (Greenberg et al., 1994; Greenberg et al., 1996; Richardson, Melosh, and Greenberg, 2004). Because of small gravity, erasure of craters by seismic shaking is considered to be more effective on small bodies.

Richardson, Melosh, and Greenberg (2004) have developed the seismic shaking model with the constraints from observational evidences on Eros. Starting from the mass conservation on as infinitely small portion of hill-slope (Culling, 1963):

$$\frac{\partial z}{\partial t} = -\left[\frac{\partial f_x}{\partial x} + \frac{\partial f_y}{\partial y}\right], \tag{3.4}$$

where z is the elevation, and f_x and f_y are the flow rates of regolith. The regolith flow rates are linearly proportional to the slope's gradient, assuming the regolith flow is isotropic:

$$f_x = -K_d \frac{\partial z}{\partial x}, \quad f_y = -K_d \frac{\partial z}{\partial y}, \tag{3.5}$$

where K_d ($\mathrm{m^3 m^{-2} s^{-1}}$) is a downslope diffusion constant. Substituting eq. (3.5) into eq.(3.4) gives

$$\frac{\partial z}{\partial t} = K_d \Delta^2 z. \tag{3.6}$$

The general solution of the diffusion equation eq. (3.6) under the axial-symmetric condition is given by

$$z(r,t) = \sum_{k=0}^{\infty} C_k J_0(kr) e^{-K_d h k^2 t}, \tag{3.7}$$

in cylindrical coordinates $(r,\ z)$, where h is the mobilized regolith layer thickness, k is the spatial wave number, and J_0 is a zero order Bessel function of the first kind. However, the diffusive constants can vary discretely over time depending on the impact number and sizes. Thus, eq. 3.7 becomes a function of the number of impacts.

$$z(r,t) = \sum_{k=0}^{\infty} C_k J_0(kr) e^{-K h k^2}, \tag{3.8}$$

$$K = \sum_{i=0}^{n} K_i, \tag{3.9}$$

where n is the number of impacts and K_i is the amount of downslope diffusion per impact. And C_k is determined by the initial topographic form (Melosh, 1989) as:

$$C_k = -\frac{dD_c^2}{128} k^2 D_c^2 e^{-k^2 D_c^2/16}. \tag{3.10}$$

Richardson, Melosh, and Greenberg (2004) assumed that the relaxation term $R = e^{-Khk^2} = e^{-6}$, which gives a depth to diameter ratio (H_c/D_c) of 0.0005, disables the crater to be found. This gives us the condition of erasure of a crater as

$$K \geq \frac{3D_c^2}{8h}. \tag{3.11}$$

This seismic shaking model can explain modification and ambiguity of the craters on small asteroids, however there are many uncertain parameters which have not examined profoundly. In our study, the efficiency of erasure and the crater distribution dependency to the movable regolith depth h will be examined. The large amount of movable regolith depth might cause faster crater erasure.

3.1.3 Boulder distribution on Itokawa

Rocks and boulders on airless bodies often exhibit fractal size distributions; the cumulative size distributions are given by power laws, such as

$$N_b(>L) \propto L^{\alpha}, \tag{3.12}$$

where $N_b(>L)$ is the number of boulders with a diameter greater than L. The same boulder size distribution can be described in an incremental size distribution as $n_b(L)\mathrm{d}L = -\mathrm{d}N_b$. The power-index α on Itokawa was first measured by Saito et al. (2006) for the

boulder size down to 5 m as -2.8 where the maximum size dimension of a each boulder was used as its diameter. Subsequently, Michikami et al. (2008) conducted a more detailed analysis and found that the power-index is $\alpha = -3.1 \pm 0.1$. Further analyses were conducted recently in Mazrouei et al. (2014) and Tancredi, Roland, and Bruzzone (2015), in power-law index among different regions from -4.1 to -2.7 were found .

Tancredi, Roland, and Bruzzone (2015) have analyzed boulder size distributions for several regions with high-resolution images from 0.01 to 0.48 m/pix (Fig. 3.3). Due to the limitation of resolutions, the small particles could not be counted. Tancredi, Roland, and Bruzzone (2015) used a maximum-likelihood fitting method with goodness-of-fit tests based on the Kolmogorov-Smirnov statistic to determine the power-law index and the usable size range of fitting, while the previous studies fitted the exponents by eye. They found that the diameters limiting the power laws were much larger than the cut-off diameter due to artificial incompleteness bias from limitation in resolution. Thus, the cut-off sizes of small boulders are ~ 2 m for the rough terrain and $0.2 - 0.6$ m for the smooth terrain.

Another interesting analysis of the size distribution was done by Tsuchiyama et al. (2011). They measured the size distribution of the samples from Itokawa smaller than 100 micron. The power-law indexes of the samples were -2.8 for $\sim 5 - 30$ micron and -2 for $\sim 30 - 100$ micron. These results suggest the indexes are slightly shallower than the indexes for large boulder distributions the power law might continue from m to μm size and the cut-off size is possibly smaller.

In general, the total number of boulders is derived as

$$N_{\rm total} = N_b(> L_{\rm min}) = C L_{\rm min}^{\alpha}, \tag{3.13}$$

and the average size of boulders is calculated as

$$\bar{L} = \int_{L_{\rm min}}^{L_{\rm max}} L n_b {\rm d}L \quad / N_{\rm total}. \tag{3.14}$$

The $\alpha < -1$ and $L_{\rm min} \ll L_{\rm max}$ lead to

$$\bar{L} \sim \frac{\alpha}{\alpha + 1} L_{\rm min}. \tag{3.15}$$

According to the random packing simulation, the surface size distribution might represent the interior size distribution (Tancredi, Roland, and Bruzzone, 2015, appendix A). The total volume $\theta_{\rm total}$ of boulders that follow the size distribution (3.12) is given

by

$$\theta_{\text{total}} = \int_{L_{\min}}^{L_{\max}} \frac{\pi}{6} L^3 n_b(L) \mathrm{d}L = \begin{cases} -\dfrac{\pi\alpha C}{6(3+\alpha)}(L_{\max}^{3+\alpha} - L_{\min}^{3+\alpha}) & (\alpha \neq -3) \\ \dfrac{\pi C}{2} \ln\left(\dfrac{L_{\max}}{L_{\min}}\right) & (\alpha = -3) \end{cases}. \tag{3.16}$$

Here, we assume that the power-index $\alpha = -3$ and the cut-off sizes are $L_{\min} = 0.1$ m, $L_{\max} = 40$ m for the Itokawa surface. The average size of surface boulder is calculated as 0.15 m. The probability that an impactor with diameter D_p happens to hit a boulder larger than D_p is given in a simple form:

$$P(> D_p) = \frac{\theta(> D_p)}{\theta_{\text{total}}} = \frac{\ln(L_{\max}) - \ln(D_p)}{\ln(L_{\max}) - \ln(L_{\min})}. \tag{3.17}$$

Fig. 3.4 shows the probabilities for different boulder cut-off sizes. The probability that an impactor hits a surface grain larger than 1 m is greater than 50% for $L_{\min} = 0.1$ m. According to the possible small asteroid distribution, the number of smaller projectile might be much greater than larger ones (e.g. Bottke et al., 2005; O'Brien and Greenberg, 2005). It is not rare to achieve the condition $D_p < L$, although the cutoff size is unknown in reality. In such cases, the target grain size would be larger than the impactor size and the armoring potentially works.

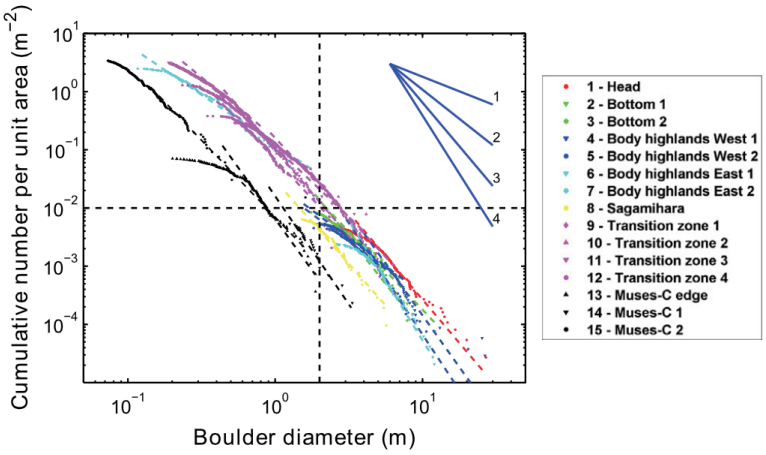

FIGURE 3.3: Cumulative distributions of boulders on different regions. The slopes and cut-off sizes vary over regions on Itokawa. (From Tancredi et al. (2015))

3.1.4 Impact probability among asteroids

Average impact probability and collisional velocity in the main belt have been investigated by dynamical calculations of MBA orbits which were assumed to represent entire

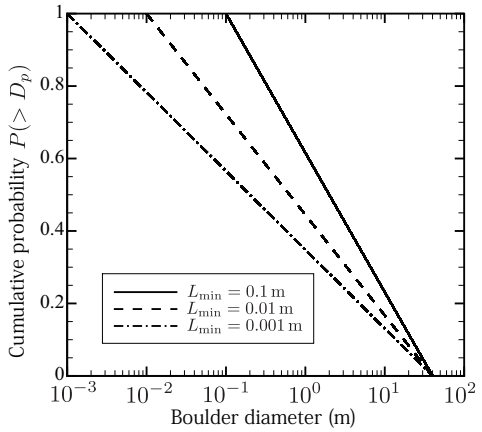

FIGURE 3.4: Probabilities to hit the target grain which is larger than the impactor size for the different minimum cut-off sizes: eq.(3.17).

asteroids in the main belt (Bottke et al., 1994). The total number of collisions in time interval T is

$$N_{\mathrm{col}}(T) = T/4 \cdot \int_{D_{\mathrm{min}}}^{D_{\mathrm{max}}} P_i (D_{\mathrm{Ito}} + D_p)^2 n_a(D_p) \mathrm{d}D_p \tag{3.18}$$

where $n_a(D_p)$ is the number of impactors with diameter D_p and P_i is the intrinsic collision probability (Bottke et al., 1994). Among cratering on the asteroid surfaces, $D_p \ll D_{\mathrm{Ito}}$ is accepted because the threshold for the catastrophic disruption is $D_p < 0.01 D_a$ for small asteroids (Benz and Asphaug, 1999). Thus, eq. (3.18) can be expressed as

$$N_{\mathrm{col}}(T) = T\mathcal{P}_{\mathrm{Ito}}(> D_{\mathrm{min}}) = T P_i D_{\mathrm{Ito}}^2 N_a(> D_{\mathrm{min}})/4 \tag{3.19}$$

We estimate the average interval between impacts (independent to sizes) as

$$\Delta\tau = T/N_{\mathrm{col}}(T) = 4/[P_i D_{\mathrm{Ito}}^2 N_a(> D_{\mathrm{min}})]. \tag{3.20}$$

TABLE 3.1: The mean intrinsic collision probability and the mean collision velocity for MBAs-MBAs, MBAs-NEAs(Apollos), NEAs(all)-NEAs(appolos) (Bottke et al., 1994)

	The intrinsic collision probability P_i ($\mathrm{km^{-2}yr^{-1}}$)	Mean collision velocity $\langle V \rangle$(km/s)
MBA-MBA	2.86×10^{-18}	5.29
MBA-NEA (Apollos)	2.18×10^{-18}	9.76
NEA-NEA (Apollos)	15.34×10^{-18}	17.36

Minimum impactor size for global seismic effects

When is the seismic shaking active? For simplicity the seismic shaking is defined as activated when the seismic accelerations exceed the asteroid's surface gravity (Richardson Jr. et al., 2005). The seismic energy injected by an impactor E_i is given by

$$E_i = \eta E_k = \frac{1}{12}\eta\pi\rho_p U^2 D_p^3, \tag{3.21}$$

where η is an impact seismic efficiency factor, E_k is the kinetic energy of an impactor, ρ_p is the projectile density, U is the impact velocity, and D_p is the projectile diameter. The impact seismic efficiency factor η is estimated with large diversity of $10^{-4} - 10^{-6}$. On the other hand, the total amount of seismic energy E_s necessary to produce $1g_a$ accelerations throughout the asteroid volume:

$$E_s = \frac{\pi G^2 \rho_a^3 D_a^5}{108 f^2}, \tag{3.22}$$

where G is the gravitational constant, D_a is the asteroid diameter, ρ_a is the asteroid density, and f is the seismic frequency. From definition, when E_i equals to E_s, the minimum size of impactor for seismic shaking is derived as:

$$D_p^* = \left[\frac{G^2 \rho_a^3 D_a^5}{9\eta\rho_p U^2 f^2}\right]^{1/3}. \tag{3.23}$$

When $\rho_a = 1900\text{kg/m}^3$, $\rho_a = 2700\text{kg/m}^3$, $U = 5000\text{m/s}$, the minimum impactor size to cause seismic effect is shown in Fig. 3.5. Note that, this model didn't consider the pressure attenuation and relaxation by granular moving, thus the minimum impactor size to cause seismic activity could be larger in reality.

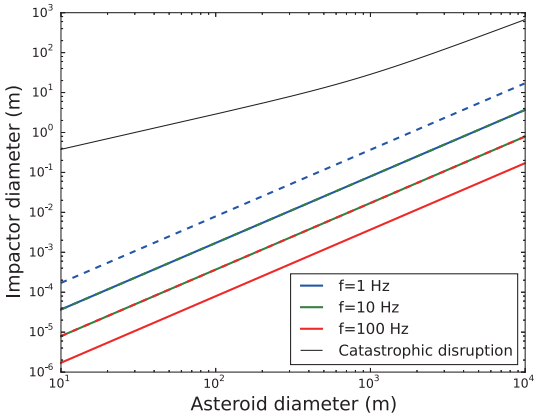

FIGURE 3.5: Minimum impactor size to cause 1 g_a accelerations on a stony asteroid of given diameter. The dashed lines indicate the case of the impact seismic efficiency factor $\eta = 10^{-6}$. The black line is the threshold of catastrophic disruption determined by Benz and Asphaug (1999).

3.2 Crater distribution simulation

In this section, so as to estimate the crater retention age of Itokawa, we employ Monte Carlo method to reproduce the crater distribution. In this study, we assume that the crater-like morphologies found by Hirata et al. (2009) were generated by impacts. Looking at the crater size distribution on Itokawa, the number of crater smaller than 100 m is depleted from the empirical saturation level, although the craters larger than 100 m are reaching the saturation level. Eros was also described the depletion of craters smaller than 100m (Chapman et al., 2002). Two reasons would explain the depletion of smaller craters: one is the low crater production rate from the armoring and the other is excess in crater erasure process. We have estimated the crater retention age of Itokawa from the largest craters production time, ignoring the crater erasure process such as seismic shaking (Richardson, Melosh, and Greenberg, 2004) in Chapter 1. However, as is suggested by previous studies, the regolith and blocks are not stable and have geologically high energy (Miyamoto et al., 2007; Barnouin-Jha et al., 2008; Noguchi et al., 2014; Tancredi, Roland, and Bruzzone, 2015). The seismic shaking process is supposed to be the influential process on the movable substrates, Here, we try to reproduce the crater distribution on Itokawa by Monte Carlo method. We employ the crater erasure condition by seismic shaking (Richardson, Melosh, and Greenberg, 2004) as the threshold of the seismic diffusivity

$$K = \int_{D_p^*} K_i(D) p_{\mathrm{Ito}}(D) \mathrm{d}D \cdot T \geq \frac{3D_c^2}{8h}, \tag{3.24}$$

where D_p^* is the minimum projectile size to cause seismic shaking, T is the time from a crater formation, K_i $\mathrm{m}^3\mathrm{m}^{-2}$ is the downslope diffusion constant per impact and h is the movable regolith thickness. The regolith thickness of Itokawa is not clearly determined, and there may be variance of regolith depth depending on regions. We used the value of ~ 42 cm which was derived by evenly spreading the regolith deposited in the smooth terrain across the entire body (Barnouin-Jha et al., 2008). The minimum projectile size $D_p^* = 0.1$m and the downslope diffusion constant $K_i = K_0 D_p^{1.15}$ where $K_0 = 10$ and $\beta = 1.15$ were used.

Next, the impact classification by the armoring condition should be taken into account. On the Itokawa surface, assuming the boulder size ranges from $L_{\mathrm{min}} = 0.1$m to $L_{\mathrm{max}} = 40$m and the size distribution can be described as $N_b(> L) = CL^{-3}$, from eq.(3.17) the probability of hitting the target grain which is larger than the projectile itself. This condition is the potential armoring zone, and then is divided into no armoring, the armoring range I, and the armoring range IIby the impact energy according to the experimental results (Chapter 2). Once the disruption energy Q_D^* and the impact velocity U are determined, the threshold of the projectile-target size ratio by ξ is given

by

$$\frac{L}{D_p} = \left(\frac{m_t}{m_p}\right)^{1/3} = \frac{U^2}{2\xi Q_D^*}. \tag{3.25}$$

The boundary lines of conditions for no armoring (the gravity scaling), the armoring range I and IIare given by the threshold $d_I = (U^2/2 \times 10^4 Q_D^*)^{1/3} D_p$ and $d_{II} = (U^2/2Q_D^*)^{1/3} D_p$ respectively. Fig.3.6 shows the armoring phases depending on the projectile and the target size ratio used in the numerical simulations.

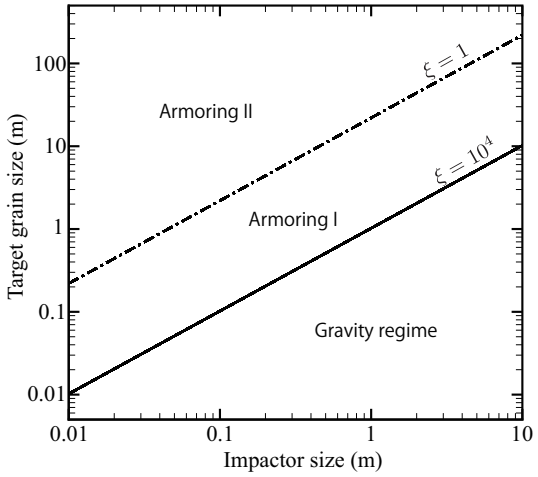

FIGURE 3.6: The condition of armoring we used in numerical calculations sorted by the energy ratio ξ.

For the armoring classification, we took the conditional branching as listed below with a random number X between 0 and 1.

- A projectile hits a target grain smaller than itself: $\psi > 1$
  No armoring happens.
- A projectile hits a target grain larger than itself: $\psi \leq 1$
  - No armoring: $X > P(> d_I)$.
    In this range, the armoring would not happen and the crater size is determined by the gravity scaling of sand, $\chi_D = 1$.
  - The armoring range I: $P(> d_I) > X > P(> d_{II})$.
    The precise estimation for craters can be evaluated by the formulation in Chap. 2, but here for simplicity we used the condition where the size of projectile is slightly smaller than target grain, i.e., $\chi_D = 0.5$.
  - The armoring range II: $X < P(> d_{II})$.
    The previous study by Güttler, Hirata, and Nakamura (2012) gives the cratering efficiency $\chi = (1 + m_t/m_p)^{-\mu/(2+\mu)}$. However, $\xi < 1$ leads to $\psi = D_p/L < 0.04$, that is, the projectile could only make a hole on the target

grain. There would be a slight depression beneath the grain on the substrate, which is reported in Durda et al. (2011), however, they might be very difficult to be found by spacecraft observation; the efficiency $\chi_D = 0$ was applied in this range.

The population of asteroids and the intrinsic collision probability give the projectile size distribution which reduced into the crater distribution with the conditional branching above. And depending on the crater formation time, the erasure of the crater is judged by eq. (3.24). Note that the overlaps of multiple craters are not took into account in our model.

3.3 Results

Fifty Monte Carlo simulation sets of the crater production and erasure for durations of 0.1, 1 and 10 Myr were calculated and finally we obtain the average crater distributions. Fig.3.7 shows the average crater distributions by our model and compares the simulation results with the observational distribution of Itokawa (Hirata et al., 2009). The gray lines in Fig.3.7 indicate the distributions without the crater erasure process by seismic shaking. The smaller craters are affected much by the armoring effect, while the number of the larger craters is not depleted that much. And so, this figure suggests that the distribution of larger craters $D_c \gtrsim 10$ m could be well reproduced by this model between 1 – 10 Myr. The armoring effect could explain the depletion of the crater > 10 m reasonably, however, the smaller craters especially < 10 m could not be explained by the low crater production rate nor the crater erasure process. The depletion of the craters $D_c < 10$ m is possibly observational error due to the difficulty in finding them on such coarse-grained surface with boulders ~ 40 m at most. That is, he meter-sized craters are comparable size of boulders on surface, and so they might be difficult to identify the depressions which could be similar to the gap between boulders and they are possibly overlooked.

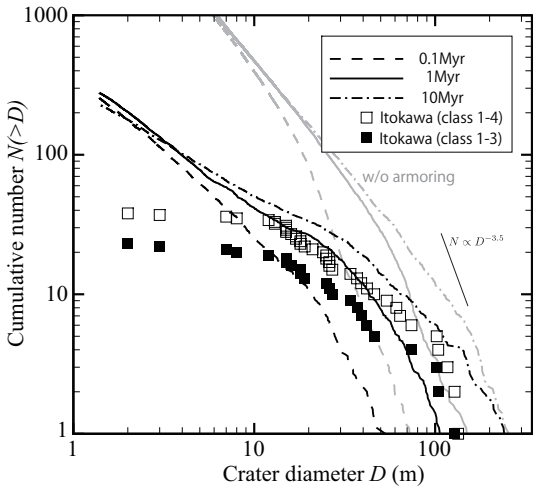

FIGURE 3.7: Comparison of our simulation and the crater size distribution on Itokawa. The black lines indicate the distributions with the armoring effect and the gray lines indicate the distributions without the armoring effect, where $h = 0.42$ m, $D_p^* = 0.1$ m. Without both of the armoring and the seismic shaking, the distribution will be $N \propto D_c^{-3 \sim -3.5}$.

3.3.1 Time dependence and saturation state

The time dependency of the crater distribution is examined here. We conducted the simulations of 0.1 Myr to 100 Myr. Figure 3.8 shows examples of one simulation test for each time interval, not averages of simulation runs. The results of short time durations 0.1 Myr and 1 Myr suggest the armoring effect is decisive for large crater distributions,

TABLE 3.2: The parameters used for our simulations.

Mean diameter of Itokawa	$D_{\rm Ito}$[km]	0.32
Gravity of Itokawa	g_a [m/s^2]	7.5×10^{-5}
Bulk density of Itokawa	$\rho_{\rm Ito}$ [kg/m^3]	1900
Bulk density of projectile	ρ_p [kg/m^3]	2500
Impact velocity	U[km/s]	5.3
Disruption energy for basalt	Q^*_D [J/kg]	1000

but the long time simulations suggest the seismic shaking is decisive. The cumulative distribution is shown in Fig. 3.9, which depicts averages of 50 times simulation runs for each time interval. An important thing is that from 10 Myr to 100 Myr the distributions with armoring and seismic shaking effects show similar shape, that is, crater distribution reaches to saturation state at $\sim$ 10 Myr, although there is still difference in the largest size of craters. This is because the seismic shaking time scale for erasure excesses the production time scale of large craters.

3.3.2 Effect of regolith layer depth

The seismic shaking model (Richardson, Melosh, and Greenberg, 2004) was assuming the migration of regolith on asteroid surfaces. Because this model is highly depending on the regolith thickness h, we examined how the regolith depth affects the crater distributions with the value from 0.01 to 1 m. Figure 3.10 shows the simulation results with a variety of regolith thickness. Small amount of regolith causes erasure of only small craters, while large amount regolith plays decisive role for crater distributions. Figure 3.10 (c) and (d) suggest the erasure rate would be comparable to the production rate with $h \sim 0.42 - 1$ m.

The topography of Itokawa has been characterized in two distinct regions, the rough terrain and the smooth terrain (Miyamoto et al., 2007). The previous papers suggest the movement of small particles on Itokawa (Miyamoto et al., 2007; Barnouin-Jha et al., 2008). However, larger particles are supposed to rarely move. Barnouin-Jha et al. (2008) have estimated the regolith depth of $\sim$ 2.3 m for the smooth terrain. Figure 3.10 (d), showing the calculation with the regolith depth $h = 1$ m, the regolith movement play a great role to erase craters immediately. This result is consistent with the observational fact that few craters were found on the smooth terrain (Hirata et al., 2009).

Richardson, Melosh, and Greenberg (2004) estimated the regolith depth h as best-fit value of 0.1 m for Eros, which was significantly less than the estimate of the regolith thickness on the order of tens meter from the observation. Thus, h does not indicate the real regolith depth, but more likely the movable regolith layer thickness. Moreover, the regolith movability is influenced by many complex factors such as cohesion, adhesion, and gravity. Thus, it is difficult to determine how much should apply for the movable regolith thickness for Itokawa surface, but the thickness $h \sim 0.42 - 1$ m is still

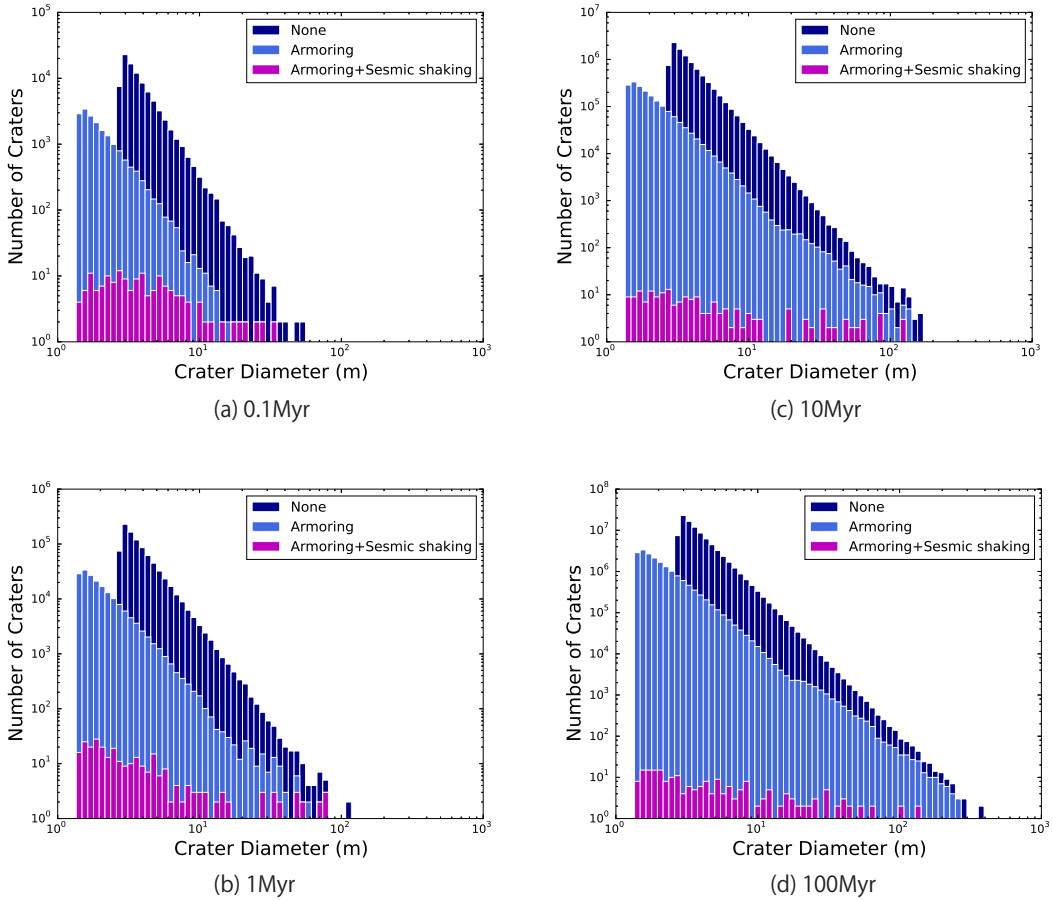

FIGURE 3.8: Examples of Monte Carlo simulation of crater distributions with changing time interval: $T = 0.1$, 1, 10 Myr. Dark blue bars show the gravity scaling crater size on sand without armoring and seismic shaking effects.

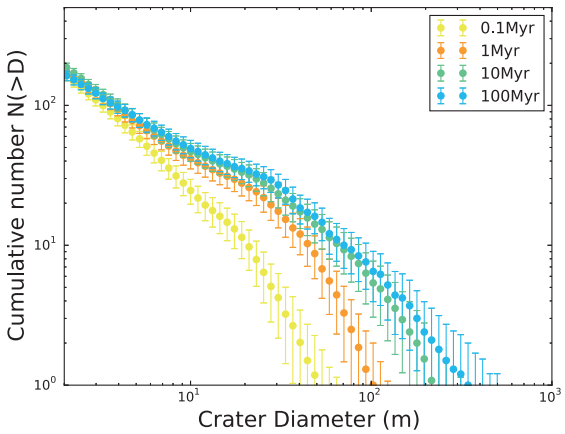

FIGURE 3.9: Cumulative distribution of craters: 0.1, 1, 10, and 100 Myr. For simulations of 0.1, 1, and 10 Myr, the averages of 50 time calculations and for 100 Myr, the average of 10 time calculations are shown, respectively.

reasonable. However, the more movable regolith than Eros seems suitable for Itokawa smooth regions. This suggests that the mobility of Itokawa regolith in smooth terrain has the same level or higher movability than Eros.

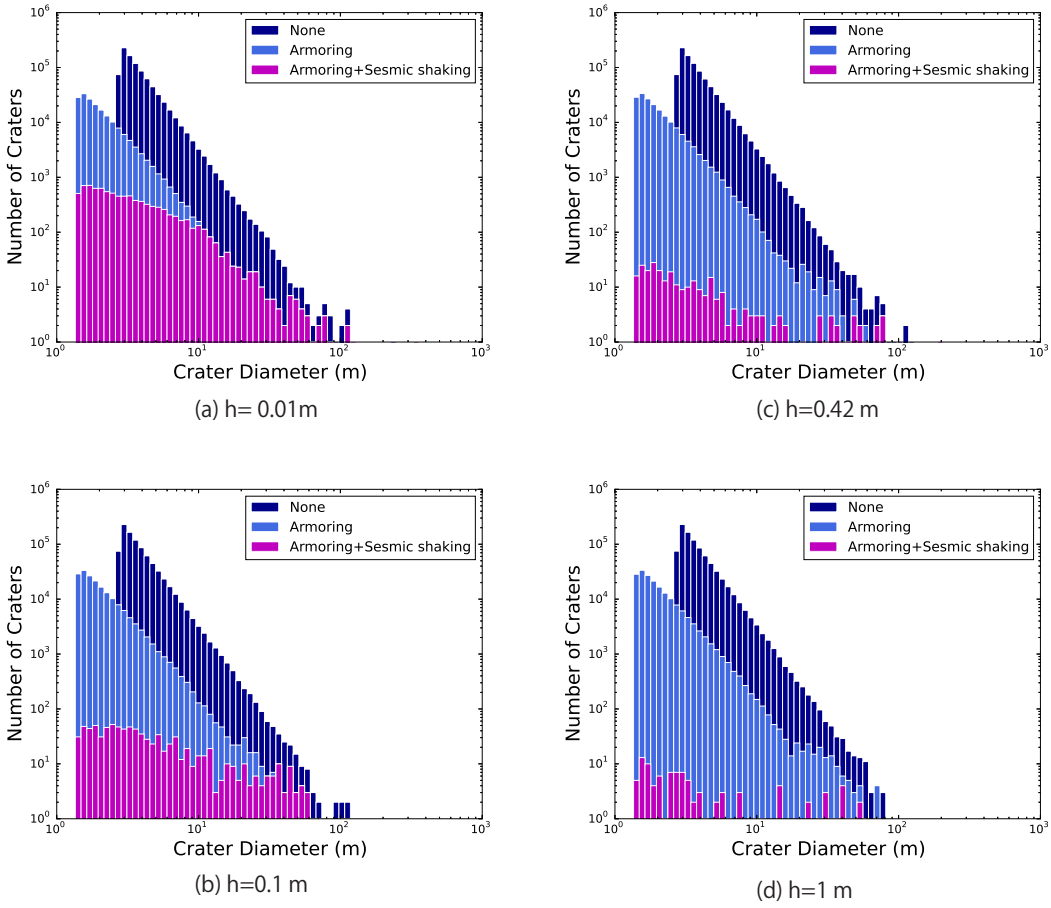

FIGURE 3.10: Monte Carlo simulations of crater distribution with changing the movable regolith thicknesses: $h = 0.01, 0.1, 0.42,$ and1 m. Dark blue bars show the gravity scaling crater size on sand without armoring and seismic shaking effects.

3.3.3 Effect of cut-off boulder size

From eq. (3.17), the cutoff sizes of the power low distribution on Itokawa, the minimum boulder size $L_{\min}$ and the maximum boulder size $L_{\max}$, determine the probability whether the projectile hits the larger boulder or not. Looking at the boulder distributions on Itokawa is shown in Fig. 3.3, $L_{\max}$ can be the largest boulder on Itokawa ~ 40m, but the minimum size would not be determined due to the observational limitation for small grains, likely ranging μm to m. Since the minimum size can change the armoring condition, we examined the influence of $L_{\min}$. Occurrence of the size ratio of a projectile to a target grain is shown in Fig. 3.12. As the dashed lines indicate the boundary of armoring conditions, the case of the cut-off size of 1 m always involves armoring because projectiles >1 m rarely impact during 1 Myr. Figure 3.14

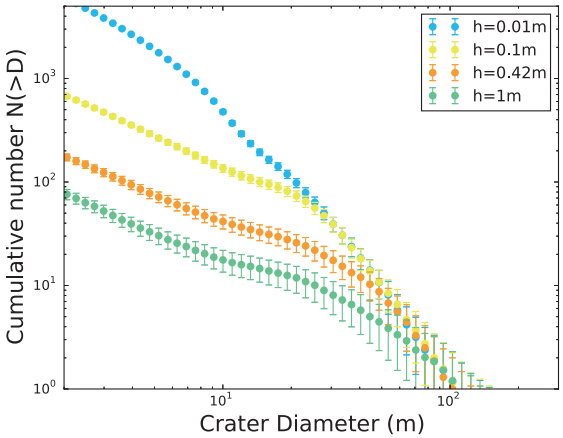

FIGURE 3.11: Cumulative distributions of craters over 1 Myr with the different mobile regolith thicknesses: $h = 0.01$, 0.1, 0.42, and 1 m.

shows cumulative distributions with varying the minimum cut-off size from 0.001 m to 1 m. Smaller craters are affected much by the cut-off size, because they are difficult to be formed due to armors of blocks. However, larger craters ~ 100 m appear not to be influenced so much by the cut-off sizes for $L_{\rm min} > 0.1$ m. Those cases have several impacts which can catastrophically disrupt target grains. The case of the cut-off size $L_{\rm min} = 1$ m in Figure 3.14 shows the similar distribution trend to the observation.

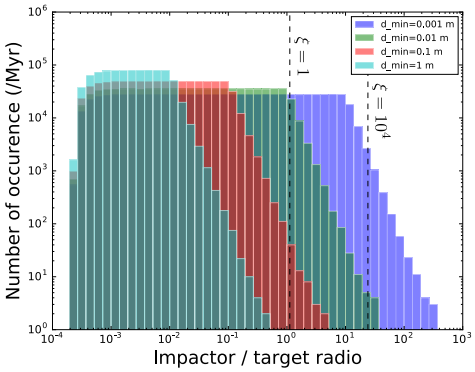

FIGURE 3.12: Occurrence of the size ratio of a projectile to a target grain in 1 Myr. The dashed lines are the boundary of armoring conditions. For the minimum cut-off size $L_{\rm min} = 1$ m, it mostly involves armoring.

3.4 Discussions

3.4.1 Crater frequency of other asteroids

Some of previous space missions have visited asteroids and have taken detailed pictures, which help us to understand how craters are formed on asteroids. The first spacecraft to visit asteroids was the spacecraft Galileo. The Galileo visited two main-belt asteroids 951 Gaspra in 1991 and 243 Ida in 1993 on its way to Jupiter (Belton

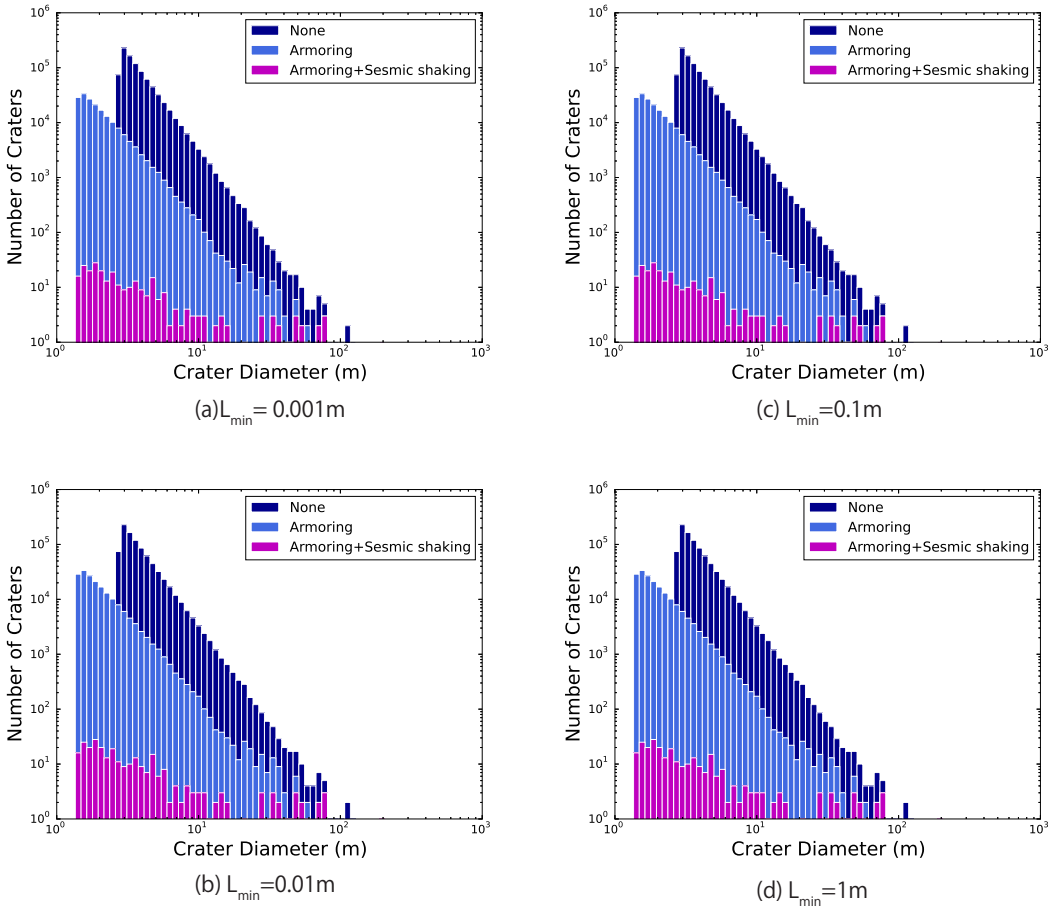

FIGURE 3.13: Examples of Monte Carlo simulation of crater distributions with changing the minimum cut-off sizes: $L_{\min} = 0.001,\ 0.01,\ 0.1,$ and1 m. Dark blue bars show the gravity scaling crater size on sand without armoring and seismic shaking effects.

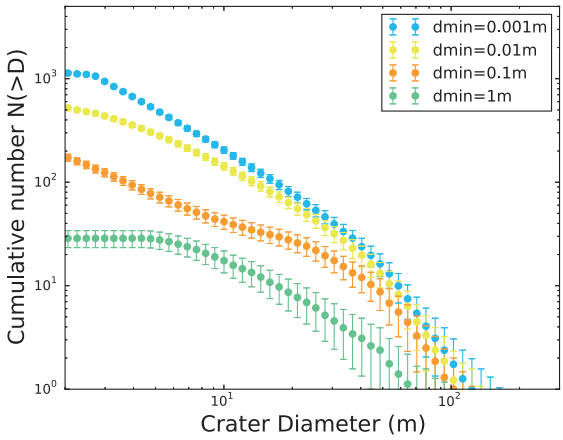

FIGURE 3.14: Cumulative distributions of craters over 1 Myr with the different minimum cut-off sizes: $L_{\min} = 0.001,\ 0.01,\ 0.01,$ and 1 m.

et al., 1992; Belton et al., 1994). Following the exploration by the spacecraft Galileo, the NEAR Shoemaker visited the main-belt asteroid 253 Mathilde in 1997 and the near-Earth asteroid 433 Eros twice in 1998 and 2000 (Veverka et al., 1999; Veverka et al., 2001). The NEAR Shoemaker spacecraft obtained a large number of high resolution images with several band filters. More recently, the fly-by of the main-belt asteroid 21 Lutetia and 2867 Steins by Rosetta was performed on its way to the comet 67P/Churyumov-Gerasimenko on July 10, 2010 (Keller et al., 2010; Sierks et al., 2011). The latest exploration is the dawn mission which orbited the second largest asteroid 4 Vesta in 2011-2012 and the dwarf planet Ceres, the largest object in main belt, from 2015. Furthermore, another near-Earth Asteroid 4179 Toutatis was observed during the fly-by of Chang'e-2 in 2012 (Huang et al., 2013). They obtained very high-resolution images with the highest resolution of ~ 2.25 m/pix because of a close encounter and the detailed features were found. Toutatis is geologically similar to Itokawa, such as a boulder-rich surface and irregular-shaped craters. The physical properties of mentioned asteroids are summarized in Table 3.3.

From those images, the craters on those asteroids have been counted and we summarize the crater frequencies in Fig. 3.15. The line indicates the empirical saturation, $N(> D_c) = 0.2 D_c^{-3}$, which has the similar inclination of impactor distribution. Interestingly, the crater frequencies are seemingly on one line, although the asteroids have different material properties and sizes. And the distribution of craters larger than ~ 0.1 km is reasonably following the empirical saturation $R = 0.2$ that found on the Moon. This saturation mechanism might be same for all these asteroids and even the Moon, that is, the mechanism is possibly independent to sizes, strengths, and impact velocities of asteroids. Seismic shaking is less likely to explain this saturation state, because seismic shaking is significantly influenced by gravity. In contrast, craters smaller than 0.1 km are apparently depleted. This slope is much shallower than the empirical saturation state. We have only few examples for this range, Itokawa and Eros, but these two suggests the less dependence to either size or surface texture; Eros is ~ 50 times larger in diameter and has a much smoother surface. Armoring contributes more on smaller and coarser asteroid and seismic shaking contributes more on larger and smoother asteroid. The different mechanisms influenced the depletion of smaller craters on Eros and Itokawa.

3.5 The rough terrain and the smooth terrain

Because the Itokawa surface is composed by two different textures, rough terrain and smooth terrain, these terrains have possibly different crater production and erasure rates. Most of the craters on the rough terrain and lack of craters on the smooth terrain may imply that erasure process is excessive in the smooth terrain. This suggests that the regolith in the smooth terrain has more movability than the rough terrain and the seismic shaking may play a great role. In contrast, the rough terrain is covered mostly

TABLE 3.3: The explored asteroids.The intrinsic collisional probability and the collisional velocity of the average main-belt asteroids are derived by Bottke et al. (1994) and those of some asteroids are computed: Ida and Gaspra by Bottke et al. (1994), Ceres and Vesta by O'Brien, Sykes, and Tricarico (2011), and Lutetia by Marchi et al. (2012)

	Asteroid	Spacecraft Name	Size (km)	Spectral type (Tholen)	P_i ($km^{-2}yr$)	$\langle V \rangle$ (km/s)
1	Ceres	Dawn	$965 \times 961 \times 891$	C	3.70×10^{-18}	5.3
4	Vesta	Dawn	$573 \times 557 \times 446$	V	2.97×10^{-18}	5.3
21	Lutetia	Rosetta	$121 \times 101 \times 75$	M	4.21×10^{-18}	4.3
243	Ida	Galileo	$59.8 \times 25.4 \times 18.6$	S	3.83×10^{-18}	3.55
253	Mathilde	NEAR Shoemaker	$66 \times 48 \times 46$	C	2.86×10^{-18}	5.3
433	Eros	NEAR Shoemaker	$34 \times 11 \times 11$	S	2.86×10^{-18}	5.3
951	Gaspra	Galileo	$19 \times 12 \times 11$	S	2.80×10^{-18}	5.0
2867	Šteins	Rosetta	$6.7 \times 5.8 \times 4.5$	E	2.86×10^{-18}	5.3
4179	Toutatis	Chang'e-2	$4.6 \times 2.3 \times 1.9$	S	2.86×10^{-18}	5.3
25143	Itokawa	Hayabusa	$0.54 \times 0.29 \times 0.21$	S	2.86×10^{-18}	5.3

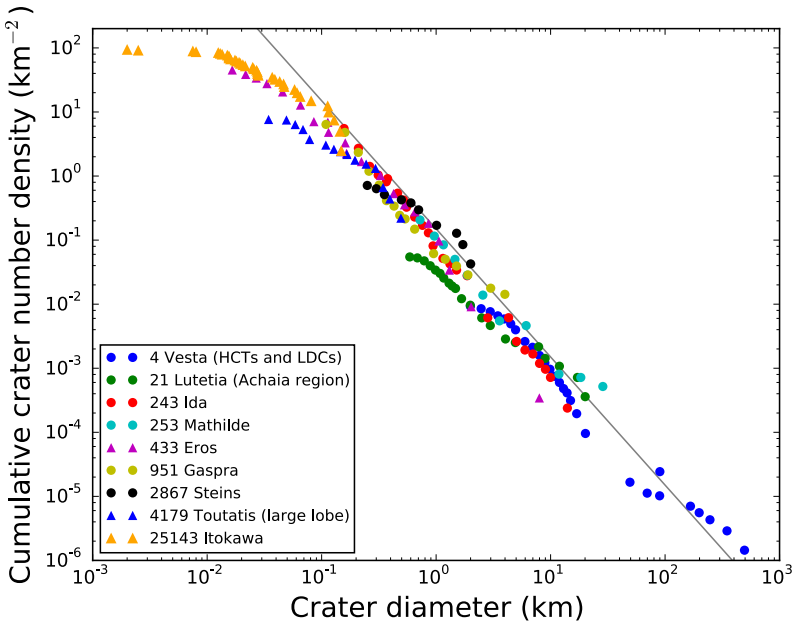

FIGURE 3.15: The crater frequency of the explored asteroids. The gray line indicates the empirical saturation $R = 0.2$ (Crater Analysis Techniques Working Group, 1979).

with m-sized boulders, which suggests armoring may be a major process to prevent formation of craters. More specifically, although the regolith might migrate also in rough terrain, the movability might not larger to erase the crater or the regolith is not enough to fill the craters. Our simulation of the minimum cut-off size $L_{\min} = 1$ m well reproduce the crater distribution on Itokawa and agree with this hypothesis. Therefore, we should have consider the crater distribution separately with the smooth terrain and the rough terrain. Because the ~ 80 % of Itokawa surface is not covered with fine regolith, simulation results suggest larger craters might survive from Itokawa formation time unless there is any other process to deform the Itokawa significantly. That is, the crater retention age 1 - 10 Myr might indicates the Itokawa formation age.

3.6 Conclusions

Crater-like features have been found on Itokawa, and the distribution of these craters exhibits the crater saturation level at large craters ($D_c > 100$ m) and the depletion in small craters (Hirata et al., 2009). Armoring effect has been suspected to be one of the explanations to the deficiency of small craters on Itokawa. Moreover, our experimental results showed the crater efficiency reduction by armoring in the previous chapter. Although in Chap. 2 we estimated the crater retention age of Itokawa, we neglected the smaller craters and assumed the uniform grain size on Itokawa, which is not the realistic condition. Thus, we conducted the crater distribution simulations with Monte Carlo code to examine whether the distribution is reproductive or not by cratering efficiency reduction which was evaluated in Chap. 2. We also have taken into account the seismic activity, which is strongly suggested by the topographical analyses (Miyamoto et al., 2007; Barnouin-Jha et al., 2008). The crater distribution involving the effect of seismic shaking had already examined by Michel et al. (2009), and they found that the small crater depletion could be caused by seismic shaking. However, there seem to be two points where deficiency rate changing, $D_c \sim 100$ m and $D_c \sim 10$ m. If the seismic shaking was the only the cause of the depletion, the slope of the crater distribution would not be changed at two points (Michel et al., 2009). We proposed the cratering model in Chap. 2 which excavates much more effectively and forms larger craters than the model which Michel et al. (2009) applied. We found that the balance between the time scale of crater production with our model and crater erasure by seismic shaking cannot necessarily explain the crater distribution. More specifically, the seismic effect was too small to reproduce the small crater depletion.

Our results suggest that the crater distribution on Itokawa could be explained by the crater production with armoring effect and the crater erasure with seismic activity. Our simulations suggest the crater retention age of Itokawa may be $1 - 10$ Myr, or possibly older due to saturation, in main belt. However, there are some parameters which have not been constrained enough to determine the decisive effect of crater distributions on blocky asteroids.

- Effect of movability
  The seismic shaking is largely influenced by the thickness of movable regolith. The small regolith thickness change significantly the number of small craters by orders of magnitude, but larger craters can retain the information of crater production. In contrast, the large regolith thickness could erase the larger craters immediately, which is consistent with absence of craters on the smooth terrain of Itokawa. This movable regolith thickness might be influenced by many factors, such as cohesion, adhesion, and surface gravity. However, the rough terrain of Itokawa appears to possess less regolith and might retain the craters from the Itokawa formation time.

- Effect of boulder distribution
  The probability that an impactor hits a target grain larger than the impactor is determined by the boulder distribution on an asteroid. Because Itokawa is such a blocky asteroid, the results suggest the largest craters may be significantly influenced. If the asteroid is dominated by meter-sized boulders, crater distribution would be changed from the regolith dominated surface and the age estimation will be changed by a few times. The distribution trend with $L_{\min} = 1$ m is similar to that of Itokawa. The cut-off size estimate by Mazrouei et al. (2014) is $L_{\min} \sim 2$ m in the rough terrain. This implies that armoring effect by surface boulders is decisive in the crater distribution on the rough terrain.

We found important to consider the formation and erasure of craters in the rough terrain and the smooth terrain apart on Itokawa. The result might change with the crater efficiency χ_D and further parametric study is needed to find the most plausible parameters. However, it appears possible to reproduce the crater distribution on Itokawa with our cratering model. If the movability of regolith was very high, that is the larger crater erasure rate excesses the production rate, the crater retention age do not exhibit the real exposed age; the age might be a lower limit. However, the rough terrain is less possible to have such large movability and more likely to retain the craters from Itokawa formation. Furthermore, the larger craters ($D_c > 100$ m) are less influenced by armoring as long as the case of Itokawa, the age estimate would not change so much with the minimum cut-off size.

Chapter 4

Local space weathering on Itokawa inferred by spectroscopy analyses

4.1 Introduction

Spectral analyses provide us with direct information of mineralogical and chemical characterizations. Space weathering is one of the most important information from spectral analyses to understand the surface evolution of asteroids. Space weathering is the common term of the processes which modify the optical spectral reflectances when the body exposed to the space environment over time. Although the mechanism of space weathering is not fully understood, irradiation by cosmic ions and bombardment by inter planetary dust are believed to induce space weathering. Thus, space weathering is observed on the surface of airless bodies, such as Mercury, lunar and asteroids. The effects of changing spectra by space weathering certainly depend on the original mineralogical properties. With courteous analyses, the chemical compositions and the mineral abundance of Itokawa samples proved to be consistent with those of LL chondrites (Nakamura et al., 2011; Tsuchiyama et al., 2013). Moreover, the samples had been thermally annealed and were similar to LL5 and/or LL6 chondrite (Nakamura et al., 2011; Yurimoto et al., 2011). Ordinary chondrites have rather similar characteristics of space weathering to lunar space weathering. Itokawa must be suffered by space weathering on its surface depending on the exposure time in space. We can speculate that the newly formed craters or recently moved features should have a lower degree of space weathering.

In previous chapters, the global crater retention age of Itokawa has been estimated. However, what the crater age means, in other words, when the crater age clock had started is not quite obvious. The local relative oldness could be evaluated from the view of space weathering, thus the chronological order of impact craters can be investigated. AMICA (Asteroidal Multi-band Imaging CAmera) was on board the Hayabusa spacecraft, and has taken images of the same perspectives with seven different bands in succession. Analyzing those image sets reveals the degree of space weathering (Ishiguro et al., 2007; Koga et al., 2014), and we can interpret the degree of space weathering as time exposed on surface. Thus we can evaluate the crater production rate as the

function of the time. Excavations by meteorite impacts are expected to make the heterogeneity of degree of space weathering on the asteroid surface. What the crater age indicates would be constrained, due to the crater production rate changing through the main belt and the near Earth orbit. In this chapter, the chronological order of craters is investigated using spectra analyses before discussing what the crater retention age derived in the previous section suggests.

4.1.1 Lunar space weathering

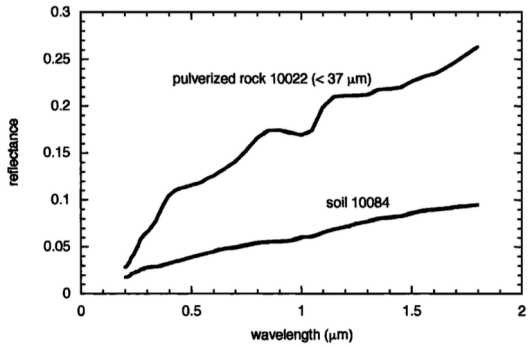

FIGURE 4.1: Reflectance spectra of Apollo 11 lunar soil sample 10084 and lunar rock 1022 pulverized to $< 37\mu$ m. The regolith is redder and darker. (From Hapke (2001))

Lunar space weathering has been well investigated and had documented in many papers. One of these important studies was the examination of the reflectance spectra of the samples from the Apollo missions (e.g. Adams and McCord, 1971). These are the first samples which had been exposed in real space environment and had not been damaged by atmosphere entry. With increased weathering, the spectra of lunar mature soils exhibited darker and redder compared with the bedrock fragments (Fig. 4.1), although they have the same mineral compositions. The sputtering of nanophase iron from iron-bearing silicates by solar wind and heating by micro-meteorite impacts on the surface of lunar soil grains are supposed to be the principle factor of spectral changes (Shkuratov et al., 1999; Pieters, Taylor, and Noble, 2000). In fine-grained mature soils, most grains were observed to have npFe^0 in the surface layer with 100 nm (Keller et al., 2000). The thickness of layer was found to be well explained by the penetration depth of solar wind ions (Loeffler, Dukes, and Baragiola, 2009).

4.1.2 Asteroids space weathering

Since the first asteroid colors and albedos were obtained in the early 1970s, the reflectance spectral mismatches between most popular meteorites, ordinary chondrites (OCs), and S-type asteroids had been puzzling (e.g Gaffey, 1976). However, conceived by lunar space weathering, space weathering became to be considered as possible explanation of the difference and maturing of the surfaces of S-type asteroids. Recently

Q-type asteroids which have apparently ordinary-chondrite-like spectra were discovered among small near-Earth asteroids and the transformation from Q-type spectra to S-type spectra as aging was proposed (Binzel et al., 2004; Nesvorný et al., 2005).

The space weathering on S-type asteroids is apparently similar to the lunar space weathering because of the similarity of the compositions, however asteroid regoliths are thought to be dominated by grains of different sizes and have more mobility due to smaller gravities. Thus, the degree and the timescale of space weathering on asteroids is not necessarily same as the Moon.

Many resent papers about spacecraft observation reported the appearance of space weathered asteroids. Color variation on the surface of asteroids was first directly observed on Gaspra and Ida by the Galileo spacecraft (Helfenstein et al., 1994; Sullivan et al., 1996). The color difference was attributed to exposure by impact cratering. More detailed investigation has taken place about S-type asteroid Eros which was observed by multi spectral imager on the NEAR-Shoemaker spacecraft (e.g. Murchie et al., 2002). The variation of spectra in Psyche crater on Eros was explained by space weathering and enhanced troilite (simulating optical effects of shock), comparing with the experimental observed spectra which simulate other possible mechanisms to change the appearance (Clark et al., 2001).

Compared with S-types, understanding of space weathering on C- and X-types is still incomplete. Nesvorný et al. (2005) presented that the slope would be negative correlation with age. By contrast, Lazzarin et al. (2006) showed the variance of spectral slope between S- , C- and X-types (Fig. 4.2) and concluded that all those types were redden and darken by space weathering, which is the opposite conclusion of Nesvorný et al. (2005). The slope dependencies of C- and X- types to the exposure time are much more moderate than S-types, and moreover they exhibit large scatters. Thus, space weathering on C- and X-types is still controversial.

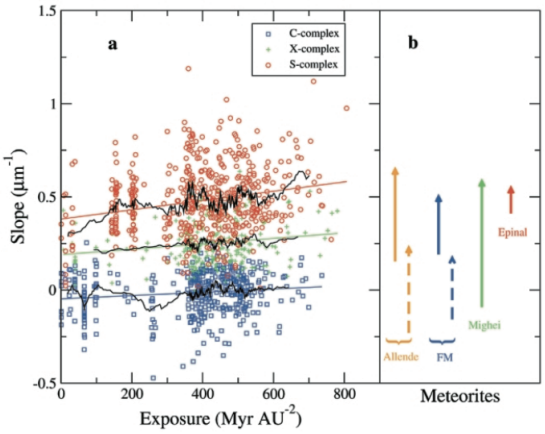

FIGURE 4.2: Spectral trends for MBAs. (a) The relationship of slope and exposure of three major asteroid groups. The slopes are all increasing with exposure age. (b) The experiment results of ion-irradiated (solid line) and laser-irradiated (dashed line).(From Lazzarin et al. (2006))

Carbonaceous Chondrites (CCs) have similar spectral shape and have been suggested as possible fragments from C-types. Both laser irradiation experiments and ion irradiation experiments indicated darkening and reddening of CCs (Moroz et al., 2004; Lazzarin et al., 2006), although the changes of spectra were not as significant as that of OCs. These results may support the observational result from Lazzarin et al. (2006) ,that suggests space weathering make the spectra of C-types redden and darken.

4.1.3 Experiments of space weathering

Space weathering was recognized by the spectral difference between lunar soils and bedrocks. In order to reproduce the spectral changes, darkening and reddening, some laboratory experiments have been performed by laser and ion irradiation which simulate two different space weathering mechanisms; solar wind implantation and micrometeorite bombardment.

The micro-meteorite bombardments were simulated by laser experiments (e.g. Yamada et al., 1999; Sasaki et al., 2001). They used the a pulse laser to simulate space weathering by high-velocity dust impact and irradiated pellet samples of olivine and pyroxene. From the olivine irradiated samples, nanophase iron particles within the amorphous vapor-deposited rims, which are similar to those observed in the rims of space-weathered lunar soils, are found.

Ion irradiation experiments had been conducted using mainly H^+ and He^+ ions at keV energies to simulate space weathering by solar wind (e.g. Hapke, 2001) in the early phase. In these studies, when a nonporous, solid surface was bombarded by ions, no darkening or reddening was observed, but when loose porous Fe-bearing powders were bombarded, spectral darkening and reddening was observed. More recent experiments which simulated solar wind heavy particle irradiation, such as Ar^+ and Ar^{++} ions, have been performed and suggested the efficiency of space weathering by heavy ion bombardments is more significant than that by the most abundant 1 keV protons (Strazzulla et al., 2005; Brunetto and Strazzulla, 2005). (Loeffler, Dukes, and Baragiola, 2009) conducted He^+ ion irradiation experiments and concluded that the two different types of space weathering, vapor redeposition and ion sputtering, result in similar NIR spectral changes.

4.1.4 Timescale for space weathering

The laboratory experiments mentioned above estimate the timescale of space weathering caused by two main processes, solar wind implantation and micrometeorite bombardment. They have different timescale: a relatively short timescale of $10^4 - 10^6$ yr for solar wind implantation (Hapke, 2001; Strazzulla et al., 2005; Loeffler, Dukes, and Baragiola, 2009) and a longer time scale of $10^7 - 10^9$ yr at 1 AU for micrometeorite impacts (Sasaki et al., 2001; Brunetto et al., 2006b). However, the ion flux and the dust flux in space have not fully quantitatively determined, for example, and so determining the

main mechanism in transforming the spectra can not be constrained straightforwardly. Moreover, since the surfaces of asteroids are not stable, such as ejecta blanket and excavation by impacts, and the irradiated orientation of grains would change, applying the experimental results. The resurfacing processes could slower the space weathering, and so estimating the timescale comparing the experimental data and the spectra directly is found to be very difficult (Brunetto et al., 2006a). The experimental approachs are important to understand fundamental phenomena in space weathering, such as the size effect of npFe included in rims (e.g. Noble, Pieters, and Keller, 2007). The smaller npFe particles (< 5 nm) redden the spectra while the larger npFe particles (> 10 nm) darken the spectra.

Thus, the timescale of space weathering has tried to be evaluated by the other methods based on the ground-based spectra observations. For example, Pieters, Taylor, and Noble (2000) determined the timescale of space weathering on the lunar as 100 – 800 Myr, using the colors of craters which were dated by radiometry and cosmic ray exposure ages. Recently to estimate of the timescale for asteroid space weathering, the relationship between the ages of asteroid families and their colors was investigated. The asteroid family ages are dated based mainly on orbital elements and size-frequency (e.g. Nesvorný et al., 2002). The characteristic timescale for space weathering was estimated as $\sim 10^9$ years from the relationship of spectral principal components and the asteroid families age (Jedicke et al., 2004). The ages of those families are summarized in Appendix C. However, recently asteroid families younger than 1 Myr were dated and very rapid transformation of spectra in the beginning was reported (Vernazza et al., 2009). They concluded that the transformation of OC-like spectra to S-type spectra would take less than 10^6 years, possibly due to solar wind. S-type asteroids change their spectra slowly afterwards. This timescale is much shorter than the lunar space weathering.

4.2 The evidence of space weathering on Itokawa

Space weathering on Itokawa has been studied through both sample analyses and spectroscopic observations. Both of them indicate that Itokawa has been space-weathered, although the timescale of space weathering is still controversial.

4.2.1 Itokawa particles analyses

The returned samples from Itokawa were analyzed in many institutes all over the world. The first and the one of the most noticeable results is the connection between LL chondrites and S-type asteroids. The Itokawa particles which are the first samples directly from spectroscopical S-type asteroid are composed mainly by olivine and pyroxene and are consistent with the composition of LL chondrites (Nakamura et al., 2012). This result suggested that the S-type asteroid spectra are certainly matured from the OC-like spectra as expected by the previous studies (e.g. Hapke, 2001).

The first measurement of noble gas isotopes in Itokawa particles was performed by Nagao et al. (2011). Large amounts of solar helium, neon and argon were observed trapped in the grains indicated the irradiation history of cosmic rays and solar wind on Itokawa surface. Measurements of cosmic-ray exposure ages of Itokawa particles revealed the surface age as young as < 8 Myr (Nagao et al., 2011) and ~ 1.5 Myr (Meier et al., 2014).

Returned samples from Itokawa revealed not only chemical components but also micro-scale morphological changes by space weathering. The existence of sulfur-bearing Fe-rich nanoparticles in a thin surface layer on olivine, low-Ca pyroxene, and plagioclase of some of the Itokawa particles was confirmed (Noguchi et al., 2011), which is analogue structure of the Apollo soil samples. Further study based on observations by STEM suggested the rapid transformation of space weathering by solar wind rather than by micrometeorite impacts (Noguchi et al., 2014). Recently formation of cosmic ray exposure tracks and solar flare particle tracks were investigated by Berger and Keller (2015). These morphological properties strongly suggest space weathering by cosmic ray irradiation and solar flare on Itokawa.

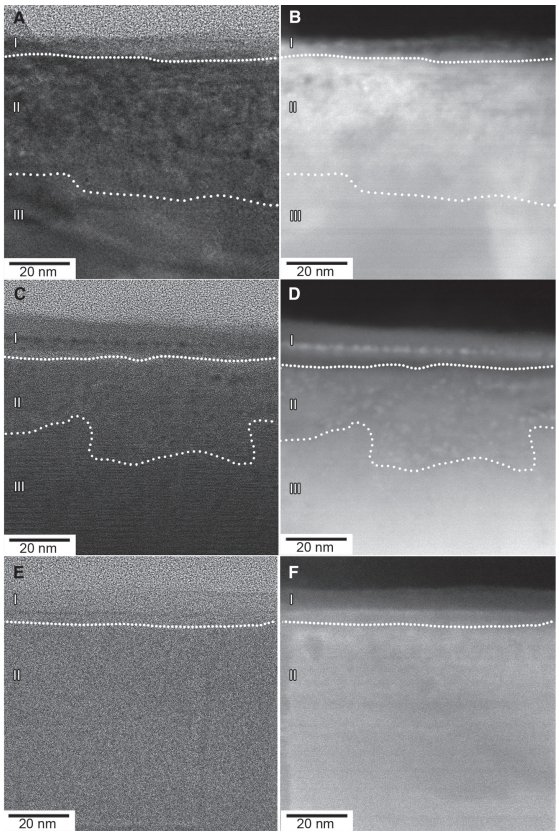

FIGURE 4.3: Edge-on BF-STEM and HAADF-STEM images of (A and B) olivine, (C and D) low-Ca pyroxene and (E and F) plagioclase in the rims of Itokawa particles. Zone I and II contain abundant nanophase iron. (From Noguchi et al. (2011))

4.2.2 Spectroscopic observation

Space weathering on Itokawa was first suggested by Binzel et al. (2001) from ground-based observation. The difference of spectra from ordinary chondrite meteorites was pointed out and was explained by the lunar-type space weathering.

The detailed study on space weathering from spectra was conducted after Hayabusa reached Itokawa and obtained high resolution images with multi-band filters. The map of space weathering index (C_v) had been presented by Ishiguro et al. (2007) using those images.

$$C_v = \frac{1 - R_v/R_w}{\lambda_w - \lambda_v} - \frac{R_v/R_w - R_b/R_w}{\lambda_v - \lambda_b}, \tag{4.1}$$

where R_x and λ_x are reflectance and effective wavelength for x-band, respectively. The C_v is derived by the comparison with laser radiation experiments for ordinary chondrites empirically (Hiroi et al., 2006). The map showed the larger heterogeneity in space weathering on Itokawa, compared with other asteroids such as Eros, Ida and Gaspra.

A more systematic way to illustrate the space weathering map was proposed by Koga et al. (2014). They applied the principal component analysis (PCA) to high dimensional data composed of six bands, and revealed the most meaningful component of Itokawa spectra. From PCA, the first principal component was turned out to indicate space weathering. This method much more sensitively showed the local change of space weathering.

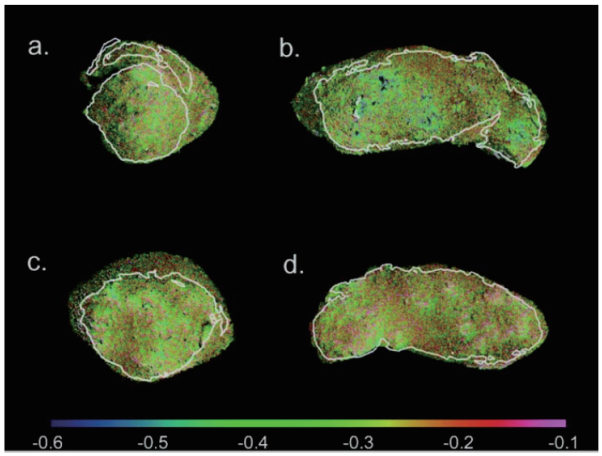

FIGURE 4.4: Space weathering index (C_v) map overlaying a w-band image (From Ishiguro et al. (2007)).

4.3 AMICA

The Asteroid Multi-band Imaging Camera (AMICA) of the Hayabusa mission to the asteroid 25143 Itokawa obtained 1662 images during the mission (Saito et al., 2006). The detailed specifications of AMICA are described by Ishiguro et al. (2010). AMICA is a CCD camera with a refractor telescope consisting of cosmic radiation-resistant and

antireflection-coated lenses. AMICA has an eight-filter system, seven of which are compatible with the Eight Color Asteroid Survey (ECAS) (Zellner, Tholen, and Tedesco, 1985). The transmittance of AMICA seven band filters (ul, b, v, w, x, p) is shown in Fig. 4.5. The effective field-of-view (FOV) was $5.83^\circ \times 5.69^\circ$, which is converted by 1024×1000 pixels, so that the instantaneous FOV corresponded to 20.490"/pixel. Thus, the resolution of ~ 70 cm/pixel is accomplished from home position, 7 km away from Itokawa.

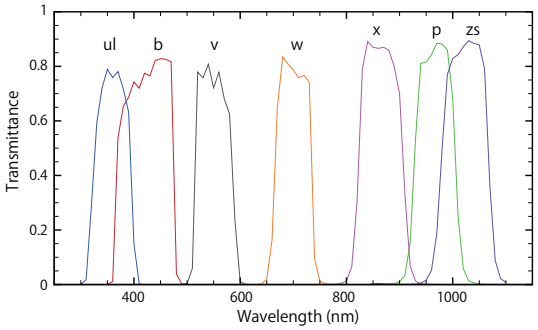

FIGURE 4.5: The transmittance of AMICA seven band filter.

TABLE 4.1: Bandpass filters used in AMICA.

band	effective wavelength μm	FWHM μm
ul	0.381	0.045
b	0.429	0.108
v	0.553	0.072
w	0.700	0.070
x	0.861	0.081
p	0.960	0.075
zs	1.008	0.066

4.4 Methods and data sets

Data sets

Close encounter of Hayabusa to Itokawa provides numerous detailed images of morphological features and color properties. AMICA raw data is archived by NASA/Planetary Data System (PDS). We used the data sets from HAY-A-AMICA-3-HAYAMICA-V1.0 (Saito et al., 2010).

To investigate the relationship between the crater-like morphologies, especially small depressions and possibly disruptions, and space weathering, we used the high resolution images. However, the number of image sets with the same place, the same resolutions and multiple band images are quite limited. Furthermore, there are no place that has all seven band images in very high resolution images (< 1 m/pixel) and we had to

use image sets with only four band images (b, v, w, p). We revisited the data used in Koga et al. (2014) with the resolution of ~ 1.6 m/pixel as well. The image sets used for analyses are listed in Table 4.2.

4.4.1 Methods

Calibrations

For the four global image sets (G1–G4) which are used in Koga et al. (2014), we conducted the calibrations steps described in Ishiguro et al. (2010) and Ishiguro (2014). The removal of halo, which is the outcome of the light scattering, and the absolute reflectance tuning are conducted for the images. The effect of halo is larger in longer wavelength, such as p- and zs-band. Ishiguro et al. (2010) deduced conversion factors from count value to radiance. In the same way, we calculated the factors from the image sets as the average spectral reflectances are the same value of the absolute ground-based observations by Binzel et al. (2001) and Lowry et al. (2005). However, the calibration steps for close-up image sets (a-f) have not been established, thus, we used the same scale factor for correction of linearity as the global image sets and the scattered light is not taken into account.The scattered light problem is more serious to long wavelength. However, the scattered light almost equally affects excepting the boundary between Itokawa and blank space, and so we can discuss the relative contribution of space weathering from spectra analyses in each image.

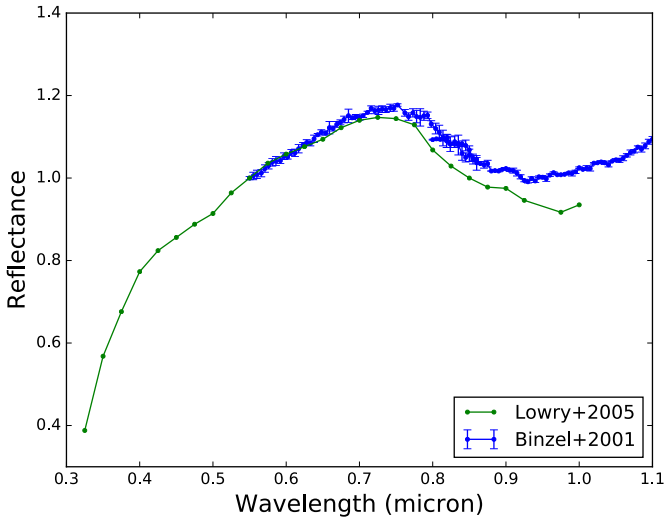

FIGURE 4.6: Reflectance spectra of Itokawa obtained by ground observation Binzel et al., 2001; Lowry et al., 2005.

Coregistration

Because of the shift of the spacecraft during changing the filters one another, the images have to be coregistrated each other between the different band filters. We took

TABLE 4.2: Data sets used for analyses. (HAY-A-AMICA-3-HAYAMICA-V1.0 from Planetary Data System)

	Image file name	Date	Filter bands	Resolution (m/pix)
G1	ST_2385540425, ST_2385559680, ST_2385578902, ST_2385598109, ST_2385617364, ST_2385655809	2005/09/17	ul, b, v, w, x, p	~ 1.6
G2	ST_2390397770, ST_2390417026, ST_2390436248, ST_2390455454, ST_2390474726, ST_2390513155	2005/09/19	ul, b, v, w, x, p	~ 1.5
G3	ST_2406708286, ST_2406717897, ST_2406727508, ST_2406737168, ST_2406746796, ST_2406766067	2005/09/25	ul, b, v, w, x, p	~ 1.4
G4	ST_2407399514, ST_2407409109, ST_2407409109, ST_2407428397, ST_2407438008, ST_2407457296	2005/09/25	ul, b, v, w, x, p	~ 1.3
a	ST_2486640220 ST_2486649845 ST_2486659453 ST_2486669110	2005/10/24	b, v, w, p	~ 0.5
b	ST_2487331445 ST_2487335302 ST_2487339240 ST_2487343619	2005/10/24	b, v, w, p	~ 0.5
c	ST_2516090882 ST_2516129281 ST_2516167681 ST_2516206081	2005/11/03	b, v, w, p	~ 0.2
d	ST_2516282879 ST_2516321279 ST_2516359695 ST_2516398095	2005/11/04	b, v, w, p	~ 0.1
e	ST_2566178777 ST_2566271576 ST_2566361188 ST_2566401631	2005/11/19	b, v, w, p	~ 0.1
f	ST_2491939184 ST_2491942076 ST_2491945018 ST_2491947926	2005/10/25	b, v, w, p	~ 0.5

two steps of coregistrations: the first step is the rough coregistration with SIFT (Scale-Invariant Feature Transform) algorithm and the second step is the presice coregistration with the minimum deviation between two images.

To find the matching points between images, the algorithm SIFT is employed. SIFT was presented by Lowe (2004) for extracting distinctive invariant features from images that can be invariant to image scale and rotation. This algorithm provides quite robust matching across as substantial range of affine distortion, change in viewpoint, addition of noise, and change in illumination. SIFT is commonly used for image matching problem. Due to the shift of the spacecraft for each image, we employ SIFT algorithm implemented in OpenCV library to determine the shift distances between the images with different filters. An example of image matching is shown in Fig. 4.7. The red circles bound by lines are the detected features with high scores in correlation between two images.

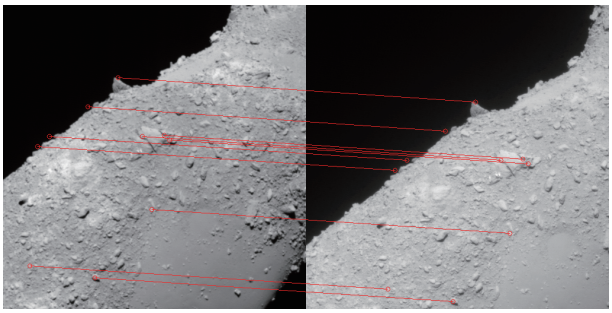

FIGURE 4.7: An expamle of SIFT matching results. These two images taken by the different band filters, and so the FOV was slightly shifted during changing the filters. The red circles are detected features with high scores in correlation between two images.

After approximating the shift distances of images, the absolute differences of two shifted images are calculated and find the point where the difference is minimized. Unless using filters or splitting pixels, images can be shifted by one pixel because image pixels are discrete. We would not like to use filters because the blur of images are not avoidable and the spectra would be mixed with nearby pixels. Each pixel is split in 4 pixels with the same value and the images can be shifted by 0.5 pixel seemingly because the shift distances calculated by SIFT algorithm are always float numbers. So the images apparently had two times higher resolutions.

Principal component analysis

Principal component analysis (PCA) is one of the most valuable analyses to reduce a complex data set to a lower dimension to reveal the simplified mechanisms that often underlie it. The main idea of principal component analysis is to compute the most meaningful basis to re-express a noisy, garbled data set. This new basis will be expected to filter out the noise and reveal hidden dynamics. In other words, the goal of PCA is

to determine which is the most important dimension. Determining this factor allows us to discern which mechanisms are important and which are redundant or noise.

Each data sample is a vector in m-dimensional space, where m is the number of measurement types, in our case, the number of band-filters. We have to use data sets with a linear combination of this set of unit length basis vectors. PCA is limited to re-expressing the data as a linear combination of its basis vectors. Let $\boldsymbol{X}$ and $\boldsymbol{Y}$ be $m \times n$ matrices related by a linear transformation $\boldsymbol{P}$. $\boldsymbol{X}$ is the original data set and $\boldsymbol{Y}$ is a re-expressed data set.

$$\boldsymbol{P}\boldsymbol{X} = \boldsymbol{Y} \tag{4.2}$$

The transformation matrix $\boldsymbol{P}$ will be determined as the covariance matrix $\boldsymbol{S}$ is optimized.

$$\boldsymbol{S} = \frac{1}{n-1}\boldsymbol{X}\boldsymbol{X}^T. \tag{4.3}$$

The ij-th element of the matrix is the inner product between the vectors of i-th and j-th components. The covariance matrix describes the correlations between all possible pares of measurements. Optimized $\boldsymbol{S}$ would be expected to have off-diagonal terms as zeros. PCA assumes the directions with the largest variances are the most important or most principal. So, PCA first selects a normalized direction in m-dimensional space along which the variance in $\boldsymbol{X}$ is maximized and it saved as PC1 ($\boldsymbol{p}_1$). Again it finds another direction along which variance is maximized in the orthogonal condition to PC1. This procedure will continue until m directions are selected.

$$\boldsymbol{P} = \begin{bmatrix} \boldsymbol{p}_1 \\ \boldsymbol{p}_2 \\ \vdots \\ \boldsymbol{p}_m \end{bmatrix}, \tag{4.4}$$

where $\boldsymbol{p}_m$ is the m-th principal component.

Principal component analysis has been widely used for spectra of asteroids mainly in order to categorize the asteroids such as S- and C-types (Tholen, 1984; Bus and Binzel, 2002a) (See Chapter 1). PCA has been performed for four global image datasets of Itokawa (Koga et al., 2014). They concluded that the first principal component might indicate the degree of space weathering.

TABLE 4.3: Correlation matrix for the five-band reflectances of Itokawa pixel spectra normalized by v-band.

	ul	b	w	x	p
ul	1	0.546	-0.200	-0.242	-0.166
b	0.546	1	-0.201	-0.291	-0.237
w	-0.200	-0.201	1	0.690	0.483
x	-0.242	-0.291	0.690	1	0.743
p	-0.167	-0.237	0.483	0.743	1

TABLE 4.4: Statistical properties of Itokawa pixel spectra normalized by v-band.

	ul	b	w	x	p
mean value	0.676	0.824	1.00	1.15	1.05
median value	0.675	0.824	1.00	1.15	1.05
standerd deviation	0.018	0.017	0.022	0.036	0.047

4.5 Results

The principal components derived from four global image sets (G1–G4) are shown in Fig. 4.8. The explained variance ratios are 0.52, 0.25, 0.11,0.9, and 0.04 PC1, PC2, PC3, PC4, and PC5, respectively. Itokawa surface spectra is mostly explained by PC1 and PC2 vectors, their total explained variance ratios are $\sim 80\%$. The sensitivity to the removal of halo is examined, and the PC1 and PC2 appeare to be insensitive to the existence of the halo in our analyses (Appendix B). The coefficients of PC1 are increasing with wave length and this trend is consistent to the space weathering tendency as redder as Koga et al. (2014) suggested. Inner product of this PC1 vector and the discrete spectra leads to PC1 scores for all Itokawa pixels. However, the higher resolution datasets only have the bands of b, v, w, and p and we had to use reduced PC1 skipping the information of ul and x bands. From Fig. 4.8, the reduced PC1 vector (PC1′) may still represent the trend of the component.

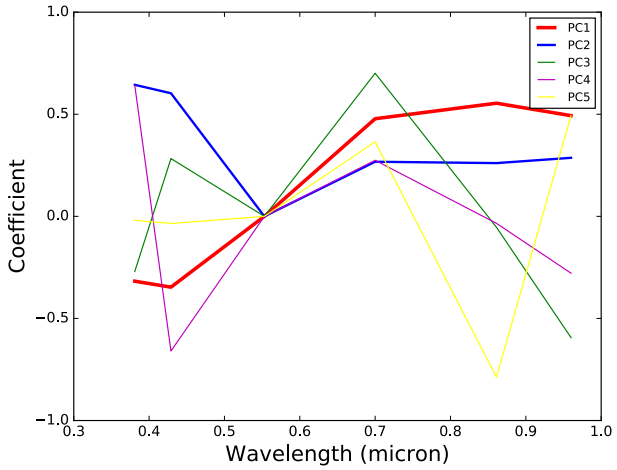

FIGURE 4.8: The principal components of Itokawa spectra. The first principal component (red) shows reddening trend.

We re-calculated the PC1 scores for four global data sets as Fig. 4.10 and the PC1′ scores with four bands and local high resolution data sets as Fig. 4.11. Note that the high-resolution local maps only indicate the relative value of PC1 score because calibrations need global views of Itokawa in the images. Thus, that we cannot compare the absolute value between two different images.

4.5.1 The first principal component (PC1)

The PC1 of Itokawa appears to indicate redding trend, which might strongly relate to space weathering. Moreover, Fig. 4.12 shows the clear inverse proportional correlation between the v-band reflectances and the PC1 scores of pixels. Space weathering is also known to darken the spectra and this negative correlation of the v-band reflectance

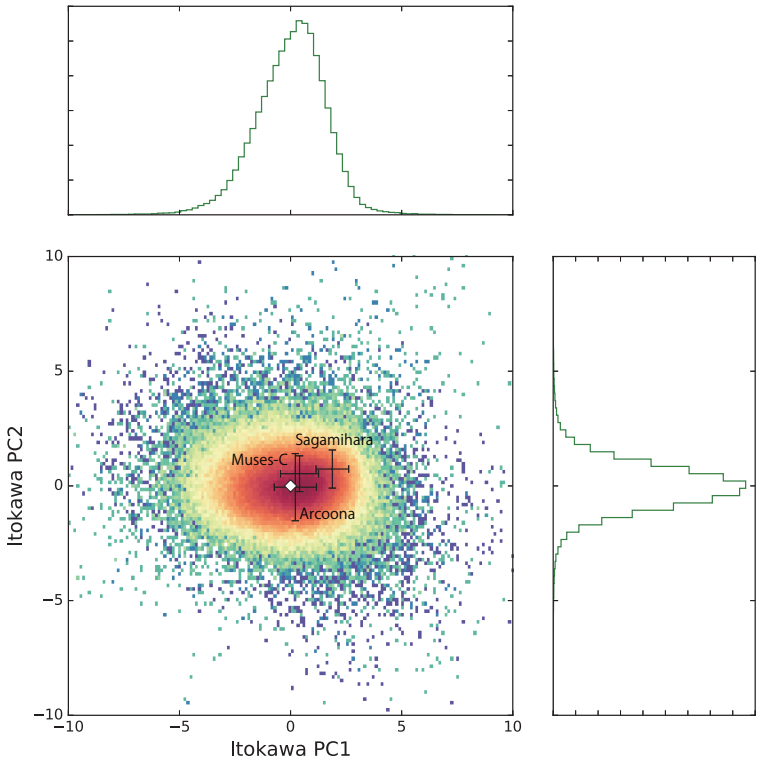

FIGURE 4.9: The distribution of PC1 and PC2 scores of all pixels. The diamond symbol indicates the average score of Itokawa. Sagamihara regio shows relatively higher PC1 score.

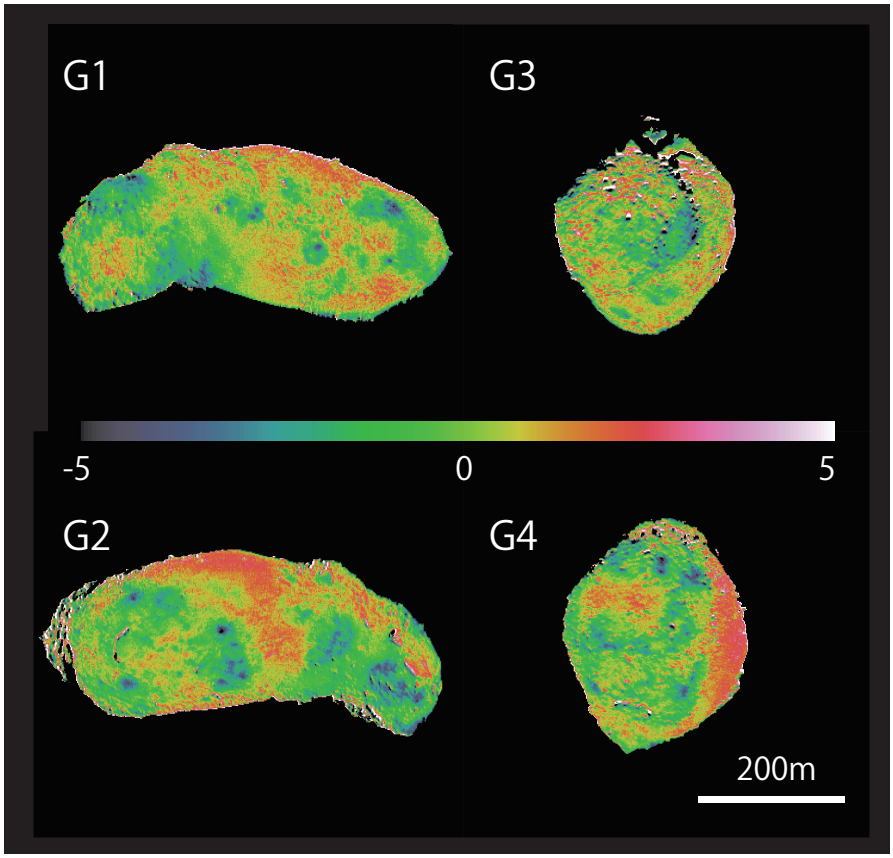

FIGURE 4.10: Global Itokawa PC1 score maps for four data sets (G1–G4). Redder surface is relatively older and bluer surface is younger.

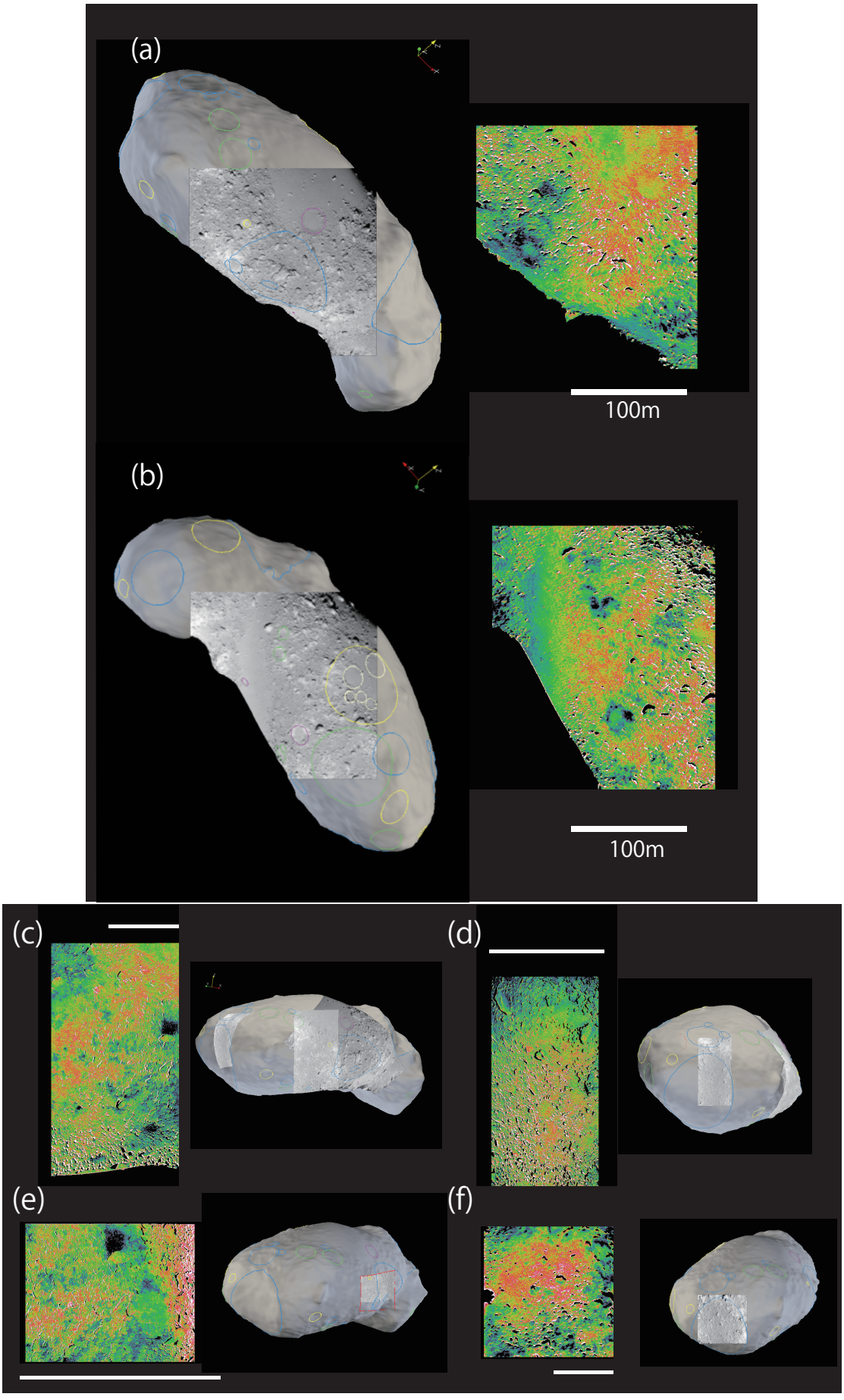

FIGURE 4.11: Local Itokawa PC1′ score maps for data sets (a-f) and corresponding 3D model perspective views. (a, b) Circles are crater candidates suggested by Hirata et al. (2009).

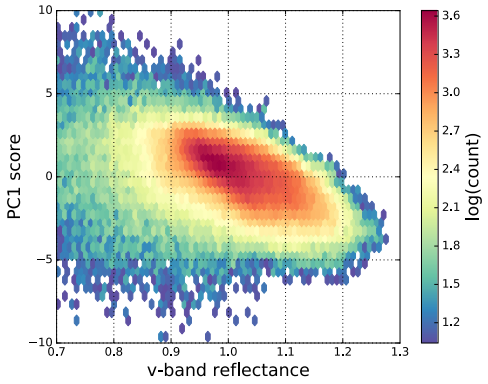

(A) PC1 score

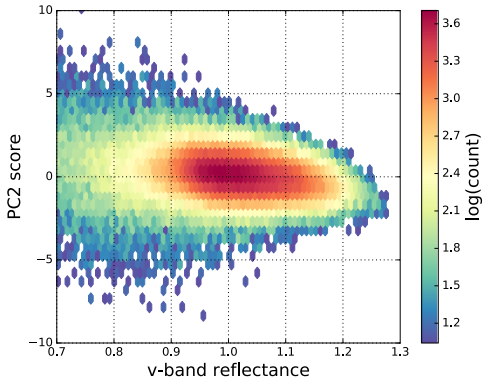

(B) PC2 score

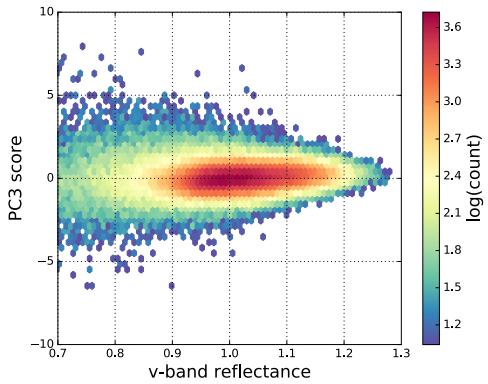

(C) PC3 score

FIGURE 4.12: Dependences of PC scores to the v-band reflectance. The v-band reflectance is normalized by the average v-band score of all pixels. The PC1 score shows clear dependence to the v-band reflectance.

and the PC1 score is consistent with space weathering trend too. Thus, the more PC1 score indicates the more space weathered surface on Itokawa. However, the lower v-band reflectances, which suggest darker and possibly older, have significant scatter of PC1 scores. The PC1 score might reflect the earlier trend of space weathering and the later stage would not be characterized by PC1. The experimental results which simulate the space weathering by laser irradiations are plotted on the Itokawa PC1-PC2 space (Fig. 4.13). Both laser and ion irradiation experiments shows the primary change in irradiated spectra along the Itokawa PC1, excepting the Epinel (H5) ion irradiated experiment by Strazzulla et al. (2005). The 60 keV Ar^{++} ion used by Strazzulla et al. (2005) had much smaller penetration depth than the observed layer width including $npFe^0$ in Itokawa samples. This might caused the difference of the trajectory in the PC1-PC2 space. In addition, as is suggested by Koga et al. (2014), in ECAS PC space the spectra of Itokawa was seen elongated from the Q-type spectra (OC-like spectra) to the S-types (see Appendix A). They argued this might be the evidence of the spectra changing from OCs to S-types by space weathering because the composition of Itokawa is similar to LL chondrites.

4.5.2 The second and third principal components (PC2 and PC3)

On the other hand, PC2 and PC3 scores have little correlation with the v-band reflectance (Fig. 4.12). In the same way as the PC1, scatters are large in the low v-band reflectances. The spectra of both the laser irradiated experiments and the ion irradiated experiments are plotted on the Itokawa PC2-PC3 space (Fig. 4.14). We chose the data of analogue samples of ordinary chondrites for comparison. This figure illustrates clear correlation between PC2 and PC3 for laser irradiated samples, while the ion irradiated samples do not show a clear trend. Suppose that the space weathering on itokawa was dominated by the vaporization caused by micrometeorite impacts, the PC1 of the Itokawa should have included the effects of PC2 and PC3. However, the PC1 of Itokawa excludes the part of the effects of space weathering which is driven by the similar mechanism to laser irradiation. Thus, the space weathering on Itokawa is not fully explained by the vaporization, but other mechanisms such as sputtering could be inferred from this figure. The sample analyses also describes the two different layers in the weathered rim which might suggest the different two mechanisms of space weathering on Itokawa (Noguchi et al., 2011).

The explain values of the PC2 and PC3 are a few times smaller than that of the PC1, but are not negligible values and might have physical meanings. The PC2 possibly represents the difference between two major space weathering mechanism, micrometeorite impacts and solar wind particle implantation. However, we don't have clear explanations for the PC2 and PC3, and the interpretations of the PC2 and PC3 are still open question. The near-infrared spectral data obtained by NIRS on Hayabusa may help understanding the meaning of the PC2 and PC3. And this would be a future study.

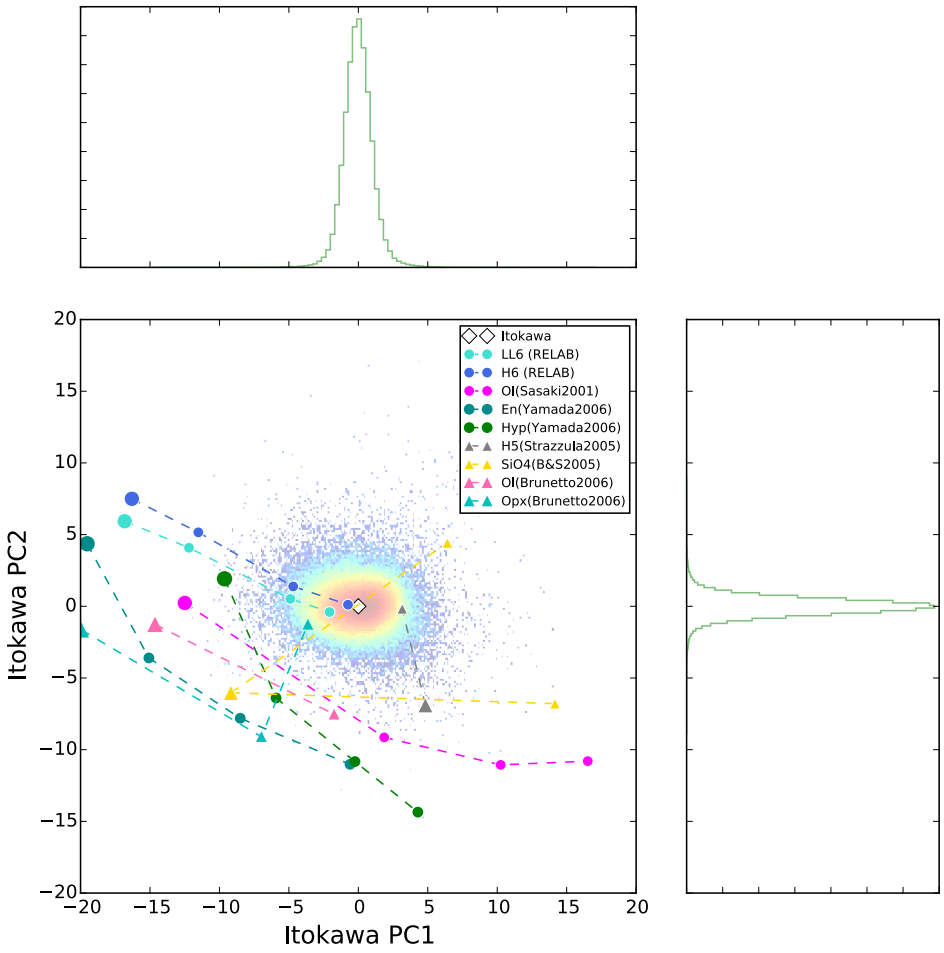

FIGURE 4.13: The previous experimental results plotted on the Itokawa PC1-PC2 space. The background color and the histograms indicate PC1 and PC2 score distribution of Itokawa spectra of pixels. The circles are the spectra of laser irradiated samples and the triangles are those of ion irradiated samples. The large markers show the untreated states of samples.

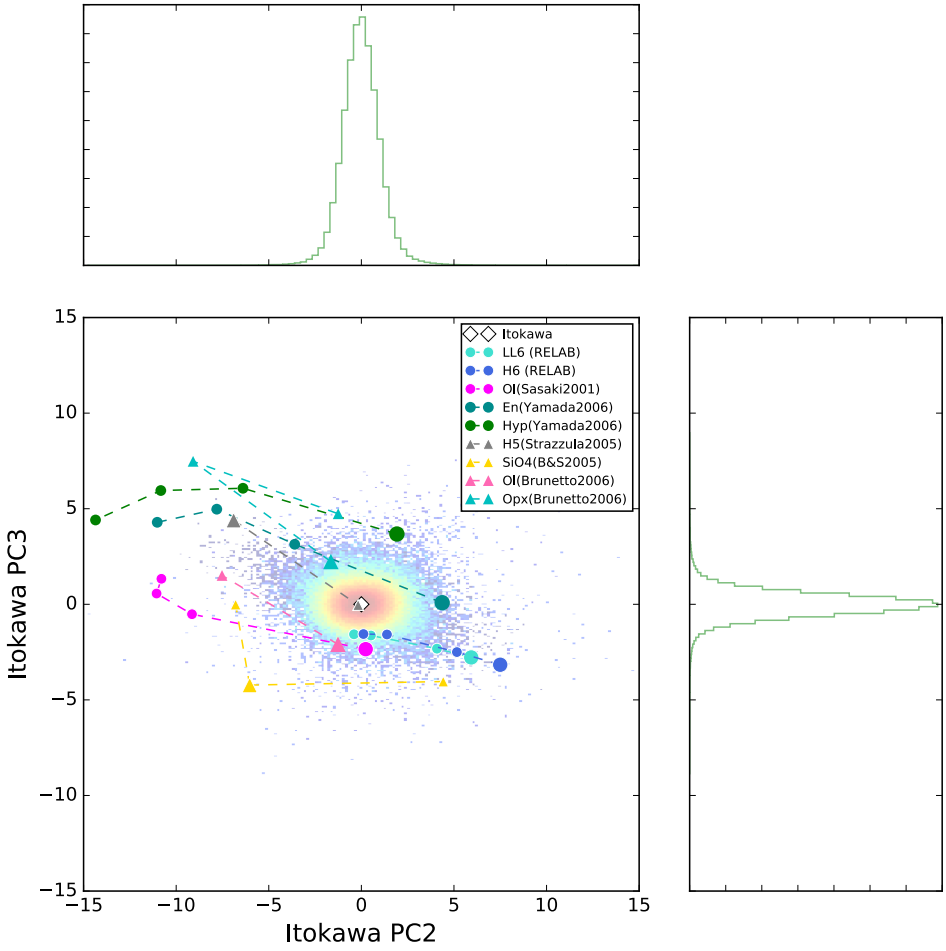

FIGURE 4.14: The previous experimental results plotted on the Itokawa PC2-PC3 space. The background color and the histograms indicate PC2 and PC3 score distribution of Itokawa spectra of pixels. The circles are the spectra of laser irradiated samples and the triangles are those of ion irradiated samples. The large markers show the untreated states of samples.

4.6 Relationship between crater-like morphologies and the PC1 score

4.6.1 Gravitational potential

We could find the relation of the gravitational potential and the PC1′ score. One of the largest circular depressions Arcoona which may be an impact crater filled with fine particles inside might present gravitationally-induced regolith migration. Data set (f) depicts the location of Arcoona, which is highly possible impact crater suggested by Hirata et al. (2009) (Fig. 4.15). From the PC1′ map in Fig. 4.16, the rim of Arcoona suggests relatively lower PC1′ score indicating shorter space-weathered time and the inside of Arcoona with higher PC1′ score indicating longer space-weathered time. High gravitational potential of the rim and low gravitational potential of the floor readily explain the consistent regolith migration from the rim to the floor. This might suggest the landslide-like regolith migration from high-potential zone to low-potential zone with gravitational slope on Itokawa surface. This gravity-induced migration is consistent with other morphological characteristics as Miyamoto et al. (2007) suggested. Consequently, after the formation of Arcoona, the regolith might move towards lower potential but the relatively large blocks on the rim stay, which implies any force to move only fine particles.

Other than Arcoona, many of craters were reported that their floors were partially and fully filled with fine particles (Hirata et al., 2009). The mobility of fine regolith appears greater than that of coarse grains since the m-sized blocks consisting the rim did not move towards the floor. Large mobility of regolith can explain the absence of craters in the smooth terrain.

Muses-C has similar relation, the gradients of gravitational potential and the PC1′ score. However, because the center of the mass of Itokawa has not been quite determined yet and the gravitational potential field on Muses-C could highly depends on the center of the mass, we do not discuss it here.

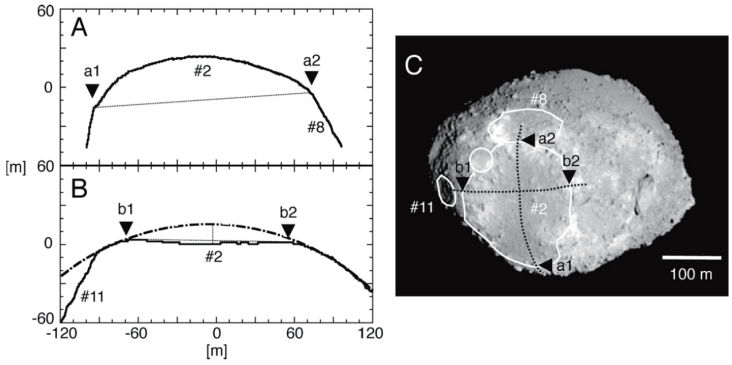

FIGURE 4.15: Cross sections of a circular depression, Arcoona, along a longitudinal line (A) and a latitudinal line (B) extracted from shape model. The floor of Arcoona is lower than the age along the line b1-b2. (From Hirata et al. (2009))

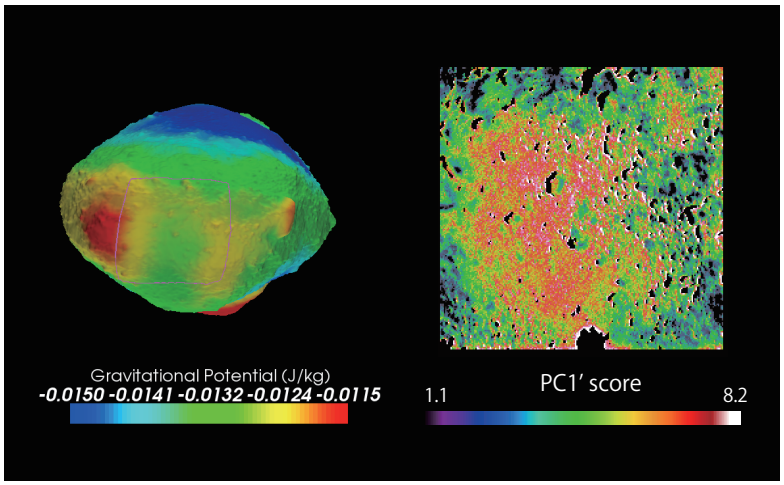

FIGURE 4.16: The gravitational potential map and PC1′ map of a possible crater, Arcoona. The left image is gravitational potential map and the square indicates the analyzed region. The right image is the PC1′ map (f) enhanced the gradation of Arcoona. The gravitationally high region corresponds to the low PC1′ region and vise versa.

4.6.2 Crater classification by PC1 score

As is depicted in the previous section, crater deformation could happen gradually by fine regolith, and so some of old craters might have old floors depositing regolith for long time. Using the global PC1 maps (Fig. 4.10), we classify the possible craters Hirata et al. (2009) into three types, R: the PC1 score of the rim is lower than that of the floor (the rim-fresh crater), F: the PC1 score of the floor is lower than the rim (the floor-fresh crater), and E: the PC1 scores of the rim and floor are homogeneous (the equally-fresh crater) (Table 4.5). The category R features possibly have been modified, while the category F features are young craters or have not deformed. Moreover, we measured the PC1 scores of crater floors and rims. The PC1 score of the floor for each crater-like feature is taken the representative score for the crater formation age, although the score only indicates the lower limit of the age since the regolith particles might have moved on the surface.

Figure 4.17 shows the histogram of the representative PC1 scores of the crater-like features. The crater-like features of F-types are dominant in lower PC1 score and those of R-types are dominant in higher PC1 score, suggesting the F-types are newer and the R-types are formed earlier. This is reasonably consistent with crater modification process by seismic shaking (Richardson, Melosh, and Greenberg, 2004). The relationship between the crater diameters and the PC1 scores is shown in Fig. 4.18. Most of newer crater-like features (PC1 score < 0) are smaller than 60 m and F-types. The lack of F-types in PC1 score > 0 implies that small craters take relatively short time to be modified and turn into E- and R-types. Most of larger crater-like features ($D_c > 60$m) are categorized into R-types. If the crater-like features were formed by impacts, the accumulation of R-type large craters suggests that craters are able to survive longer than

the large crater production interval. If the crater number was saturated, the production and the erasure rate would be almost the same and the PC1 score of craters are homogeneously distributed, however, the PC1 scores for larger features tends to accumulate in older distributions. The number of craters on asteroid Itokawa appears to have not reached the saturation yet.

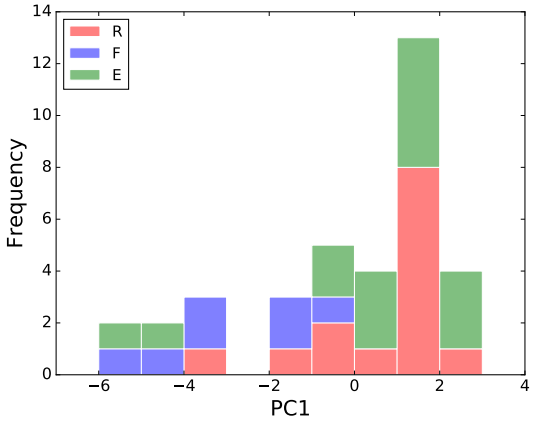

FIGURE 4.17: The PC1 score frequency among crater-like features. F-types dominate lower PC1 score and R-types dominate higher PC1 score.

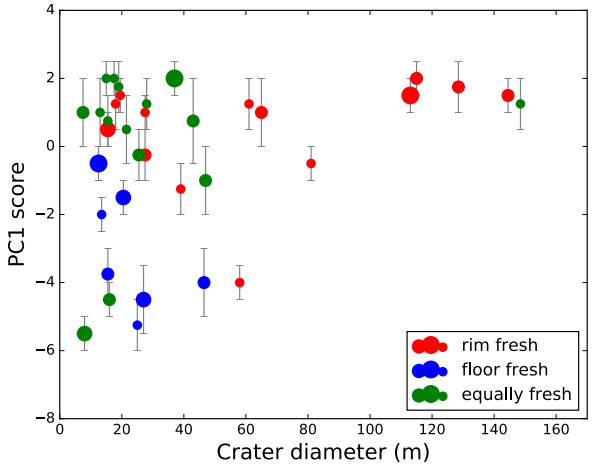

FIGURE 4.18: Crater diameters and PC1 scores. The symbol size corresponds to the confidence classification of Hirata et al. (2009) and the larger symbols are more confident based on morphological analysis.

4.7 Discussions

4.7.1 Comparison of smooth terrains

It is interesting to compare the difference among two smooth terrains, Sagamihara regio and Muses-C regio. Their PC1 scores are significantly different; Sagamihara regio has

TABLE 4.5: Crater classification by PC1 scores. The PC1 scores of craters are represented by the score of floor. The IDs correspond to the crater candidates in Hirata et al. (2009).

ID	Diameter (m)	PC1 classification	PC1 Score (floor)		PC1 Score (rim)		confidence classification
			min	max	min	max	
1	148.5	E	0.5	2	−0.5	1.5	4
2	144.5	R	1	2	−2.5	−1	2
3	128.5	R	1	2.5	−0.5	0.5	4
4	113	R	1	2	−2.5	−1	3
5	115	R	1.5	2.5	−4	0.5	2
6	81	R	−1	0	−2.5	−1.5	2
7	65	R	0	2	−1	0	4
8	61	R	0.5	2	−3	−1	4
9	58	R	−4.5	−3.5	−5.5	−4.5	4
10	46.5	F	−5	−3	−0.5	0.5	3
11	47	E	−2	0	−2	0	3
12	39	R	−2	−0.5	−0.5	0.5	3
13	37	E	1.5	2.5	1.5	2.5	1
14	43	E	−0.5	2	−0.5	2	3
15	27.5	R	−1	0.5	−3	−2	1
16	27	F	−5.5	−3.5	−1.5	−0.5	2
17	27.5	R	0.5	1.5	0	1	4
18	28	E	0.5	2	0.5	2	4
19	25.5	E	−1	0.5	−1	0.5	3
20	25	F	−6	−4.5	−4	−3	4
21	21.5	E	−0.5	1.5	−0.5	1.5	4
22	20.5	F	−2	−1	1	2	2
23	19.5	R	1	2	−1	0	2
24	18	R	0.5	2	−3.5	−2.5	3
25	19	E	1	2.5	1	2.5	4
26	17.5	E	1.5	2.5	1.5	2.5	4
27	16	E	−5	−4	−5	−4	3
28	15	E	1.5	2.5	1.5	2.5	4
29	15.5	F	−4.5	−3	−2	0	3
30	15.5	R	0	1	0	1	3
31	15.5	E	0	1.5	0	1.5	4
32	13	E	0	2	0	2	4
33	13.5	F	−2.5	−1.5	−2.5	−1.5	4
34	12.5	F	−1	0	−1	0	1
35	8	E	−6	−5	−6	−5	2
36	7.5	E	0	2	0	2	3

an older surface and Muses-C regio has a younger surface. There might be two possible explanations: the difference in formation ages and the difference in resurfacing rates.

Formation age They appear to have similar surface textures with relatively small grains (mm-cm). If they have the same mechanism of space weathering and resurfacing, the difference in PC1 scores may suggests the difference in formation age. They were less likely to be formed by tidal force, YORP spin-up and the accumulation of Itokawa itself. Muses-C might formed when the two bodies were combined together.

Resurfacing rate If they are formed at the same time, the difference in resurfacing rate may contribute the PC1 score difference. Since thermal condition and impact condition are supposed to be similar, fragmentation of surface grains due to thermal fatigue and rapture by impacts are less likely to make the difference. However, the regolith mobility difference due to such as geological potential difference and regolith depth difference might change regolith migration rates.

4.7.2 Spectral age

Assuming that the first principal component of Itokawa indicates the degree of space weathering, one of the oldest regions on Itokawa is Sagamihara regio, PC1$\sim 1.0 - 2.7$. Less craters were found in Sagamihara regio and the PC1 score appears homogeneous, which supports that the mobility of regolith is higher in fine particles and the crater elevations have been attenuated with short time. The age of Sagamihara regio might be the lower limit of the Itokawa formation age because in reality the regolith possibly moves and rolls over and so the surface rejuvenile in some rate. The various surface ages of several Itokawa particles which were sampled from Muses-C regio have been estimated. The cosmic ray exposure ages were $10^6 - 10^7$ years (Nagao et al., 2011; Meier et al., 2014) and the solar flare track ages were $10^4 - 10^5$ years (Berger and Keller, 2015). Since the solar cosmic rays are able to penetrate $\sim$ cm-to-m depth of the surface, the cosmic ray exposure ages reflects the residence time of the particle at $\sim$ cm-to-m depth and we cannot detect the orientation changes. In contrast, the solar flare tracks were generated much less deeper than the cosmic rays and the density slope could tell the stable time in orientation. Space weathering can influence only uppermost surface of the particles and the rotation of regolith could reset the spectra. Thus, the solar flare track time are highly plausible to indicate the exposure ages of the touch-down sight, which suggests very fast transition of spectra by space weathering. The spectra transitions of olivine and ordinary chondrites simulated by laser radiation experiments simulating micrometeorite impacts (Sasaki et al., 2001, RELAB spectra database) are presented in Fig. 4.21. The space weathering simulations by laboratory experiments are well fitted along the PC1 axis. Moreover the degree of space weathering on Itokawa is still on the way of maturing, because the figure shows that the more matured states pass through the PC1 scores of Itokawa. All the experiments show the deceleration of transition rate

as time (Fig. 4.19). According to the several laser radiation experiments, the relationship of irradiated energy and shift distance in PC1 score is obtained empirically:

$$\Delta PC1 = 16.1 \log_{10}(E[\mathrm{mJ}]) - 6.34 \qquad (\mathrm{R}^2 = 0.88). \tag{4.5}$$

Irradiated energy might be proportional to exposure time, $E = kt$ where k is a constant, and the empirical equation above will be

$$\Delta PC1 = 16.1 \log_{10}(t) + C. \tag{4.6}$$

The average PC1 and PC2 scores and the average v-band refrectances for Muses-C and Sagamihara regios are in Table 4.6 and both Sagamihara and Muses-C regios are plotted in the PC1-PC2 space in Fig. 4.9. Since we know the relationship of the shift distance in PC1 score and the age by Itokawa particles, the age of Sagamihara regio is suggested to be ~ 1.23 times older than that of Muses-C regio. Importantly, this result suggests the ages all over Itokawa might be in the same oder. One of the oldest region Sagamihara appears also still young as on the order of $10^4 - 10^5$ yr (solar flare track ages), even though Itokawa has heterogeneously-space-weathered surface.

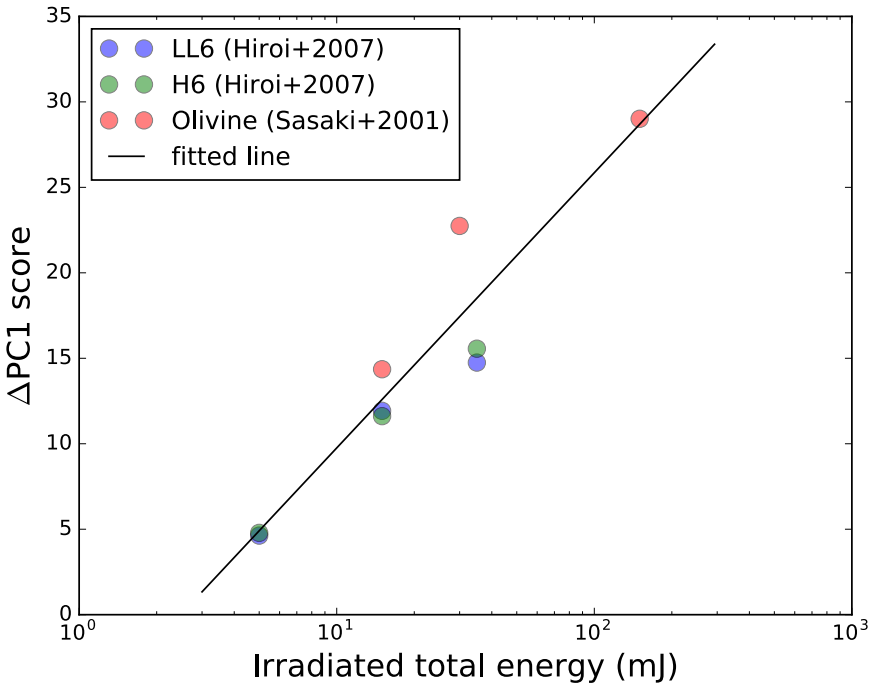

FIGURE 4.19: The relationship between irradiated total energy to samples and shift distance of PC1 score.

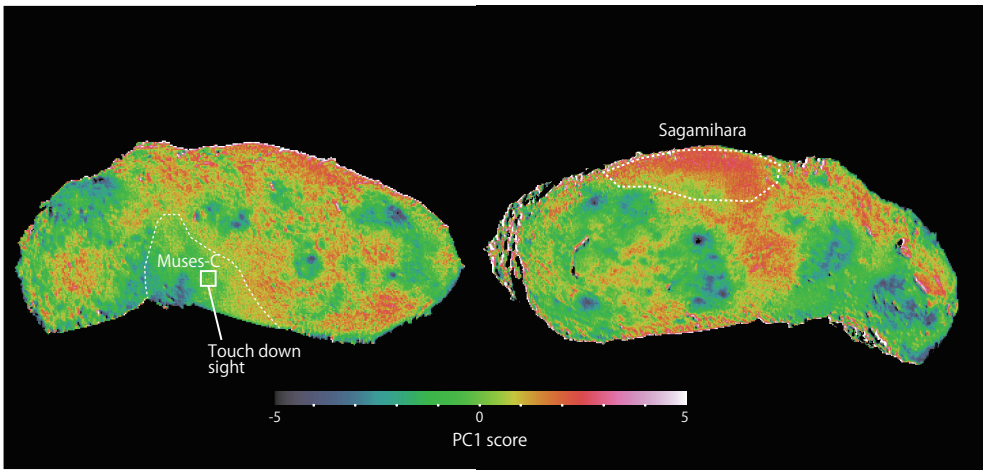

FIGURE 4.20: Touch-down sight of Hayabusa space craft and Sagamihara region.

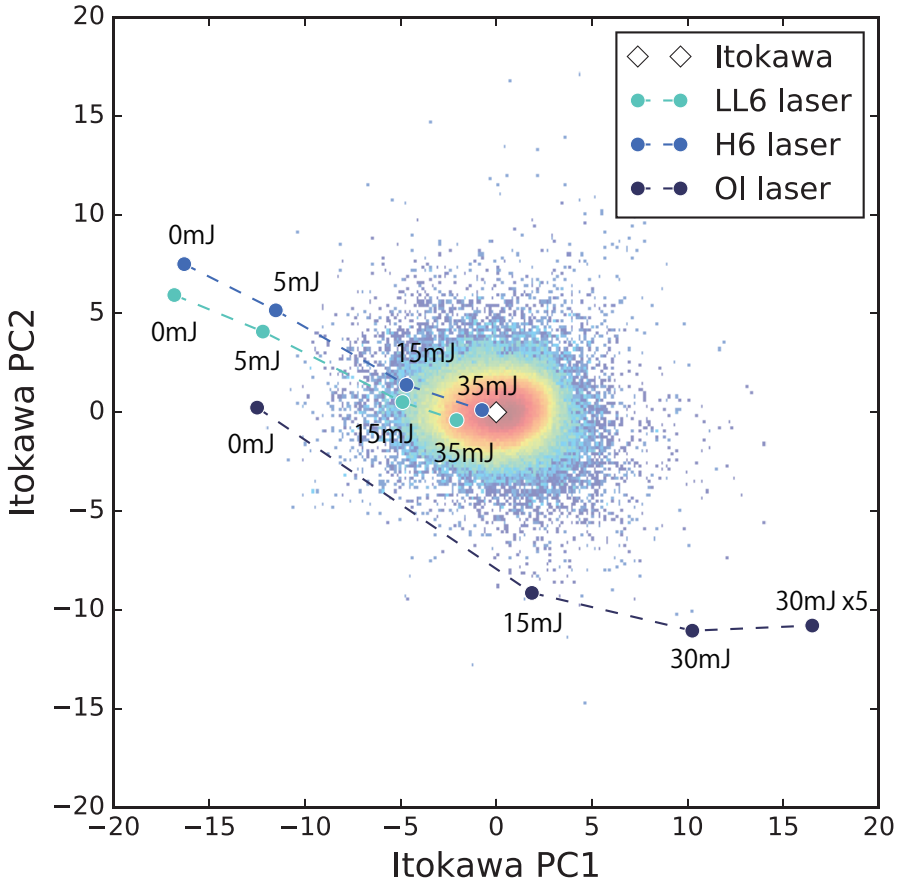

FIGURE 4.21: The transition of spectra from laboratory experiments in Itokawa PC1-PC2-space. Laser radiation experiments (dark blue circles: Sasaki et al. 2001; other circles: Hiroi et al., 2007) simulating micrometeorite impacts. The colored dots in background indicate the PC1 and PC2 score of each pixel.

TABLE 4.6: The PC1, PC2 scores and the v-band reflectance of Muses-C and Sagamihara. Global averaged v-band reflectance is 1.

Regio name	PC1 score	PC2 score	v-band
Muses-C	0.40 ± 0.78	0.53 ± 0.86	0.97 ± 0.04
Sagamihara	1.88 ± 0.83	0.61 ± 0.74	0.94 ± 0.03

4.7.3 Impact rate change

Assuming that the rate of space weathering did not change in time, eq. (4.6) leads to convert the PC1 score into relative exposure time (Fig. 4.22). It is noted that relative exposure time is 1 at PC1score equals to 0. The crater distribution in diameter and relative exposure time plane (Fig. 4.22) shows the absence of large younger craters. The craters larger than 60 m in diameter have relatively old floors with fresh rims, wile the smaller ones have a variety of PC1 scores. We can propose one hypothesis that the absence of large younger craters indicates change in impact rate. That is, the distribution may reflect the impact rage change through migration from MB to NE. Impact rage may decrease significantly, because the population of asteroids in MB is ~ 1000 times larger than that of NE (e.g. Bottke, 2002). Thus, we can estimate the migration age from the inflection point.

From eq. (3.20), we can estimate the time interval of crater production both in the main belt and the near-Earth region. For simplicity we assume no armoring happens, that is, the crater size would be gravity-scaling on sand targets. Also we assume that a projectile density is comparable to a bulk target density. The intrinsic collision probability and the mean collisional velocity among NEOs are 15.34×10^{-18} km^{-2}yr^{-1} and ~ 17 km/s (Bottke et al., 1994).

$$
\begin{aligned}
D_c &= \frac{1.18}{2^{0.83}} (32 K_1)^{1/3} \left(\frac{g}{U^2} \right)^{-0.17} D_p^{0.83}, \\
&= \begin{cases} 122 D_p^{0.83} \\ 181 D_p^{0.83} \end{cases} .
\end{aligned} \tag{4.7}
$$

Thus, the crater production intervals $\Delta\tau \propto D_c^{3.5}$ are shown in Fig. 4.23. Time intervals to form a crater larger than 100 m in diameter are ~ 0.4 Myr for the main belt and ~ 17 Myr for the near-Earth region. Assuming that the orbital migration of Itokawa occurred at 1 in relative exposure time, there are four craters larger than ~ 40 m. Again, the time intervals to form a crater larger than 40 m in diameter are ~ 0.01 Myr for the main belt and ~ 0.7 Myr for the near-Earth region. Thus, four of them may take ~ 2.8 Myr in near-Earth region. Note that this age is derived from gravity-scaling, and so if the armoring works, the age would be a few times larger. The residence time in the near-Earth region on the order of 1 Myr is compatible with the CRE ages (Nagao et al., 2011; Meier et al., 2014) and the spectral ages (Koga et al., 2014; Bonal et al., 2015). This suggests that the transition from MB to NE might occur in the order of 1 Myr.

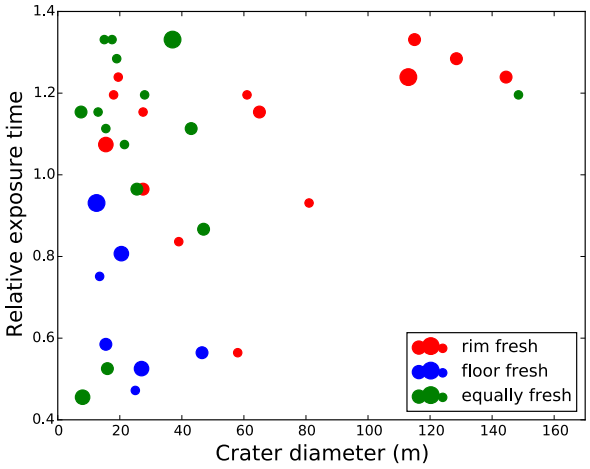

FIGURE 4.22: Relative exposure time of circular feature floors. The absence of large young features is found. Large features are populated in old age.

It is emphasized that the distribution of craters in time strongly suggests the change in impact rate, and so two phases, MB phase and NE phase, should be considered separately and totally the age of Itokawa nay be a few to a few tens million years. This result is still consistent with the CRE ages and the spectral ages. In consequent, the CRE ages and the spectral ages could be interpreted into both the total age and the residence time in NE.

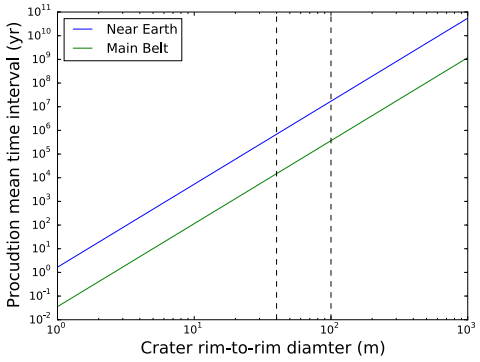

FIGURE 4.23: Time interval for crater production on a sand target. The dashed lines indicate 40 m and 100 m, respectively. In the near-Earth region it takes more than 40 times of in the main belt to accumulate a crater of the same size.

4.8 Conclusions

The relationship between crates and space weathering is mainly investigated in this chapter. We conducted principal component analyses for the global image sets and

the local high resolution image sets up to ~ 0.1m/pixel of Itokawa taken by AMICA as Koga et al. (2014) did. The first principal component correlated to the v-band reflectance strongly suggests spectral reddening and darkening by space weathering, as is suggested by Koga et al. (2014). The second principal component could also indicate space weathering, since there are two major processes of space weathering, solar wind implantation and micrometeorite impacts. However, the second principal component also appears the similar trend with changing grain size of olivine samples. Thus, what the second principal component really means is open question for now.

Using the index of the PC1, relatively newer and older places can be depicted. We found the landslide-like regolith migration in Muses-C and inside of a large crater-like feature, Arcoona, along the gravitational slope. If it is a impact crater, this suggests that crater deformation certainly happens on the rubble-pile asteroid Itokawa and the time scale is as long as the gradient of the degree of space weathering comes out.

We classified the possible craters which were topographically identified by Hirata et al. (2009) into three types: the rim fresh craters (R-types), the floor fresh craters (F-types) and the equally fresh craters (E-types). Among the crater-like features which are topographically plausible craters (confident class 1–3 in Hirata et al. (2009)), the first type dominates the old and large crater-like features ($D_c > 60$m)and the second type dominates the young and small crater-like features. All type features are mixed in small features and the modification from F-types to R- and E-types was implied by R-type populating in larger PC1 score in Fig. 4.18.

If the circular features were formed by impact events, the circular feature diameter-PC1 score of the floors relation possibly gives us chronological information. If the craters were at the saturation state and the crater production and crater erasure was equivalent, the crater would be formed uniformly in time and both small craters in PC1 score. However, the absence of young craters was found in larger craters > 60 m, which suggests the change in crater production rate. The population of NEOs is 1000 times less than that of MBAs (Bottke, 2002), and so the orbital change could trigger this change. This inflection point might be on the order of million years, which is compatible with the short CRE ages (Nagao et al., 2011; Meier et al., 2014) and spectra ages (Koga et al., 2014; Bonal et al., 2015). This result may indicate the larger craters were formed in the main belt and were retained despite of the dynamical orbital change. The larger craters are populated in quite short interval in the diameter-PC1 plane. This can be also explained by the orbital transition. The speed of space weathering is accelerated in the near-Earth orbit because the solar wind is supposed to mainly cause space weathering on Itokawa in proportional to the square of the distance from the Sun. In contrast, the chance of impacts is ~ 1000 times less in near-Earth region. Thus, the difference in PC1 score of craters formed in the main belt was degenerated in the strong space-weathering effect in the near-Earth region. If the hypothesis that the inflection point of crater distribution indicates the transition age is correct, the large old craters indicate the residence time in the main belt $\mathcal{O}$(1 Myr)–$\mathcal{O}$(10 Myr) and the relatively

young small craters may reflect the residence time in the near-Earth orbit: $\mathcal{O}$(1 Myr).

Chapter 5

Implications for dynamical evolution of Itokawa

5.1 Introduction

We have investigated impact cratering, which is one of the crucial phenomena reforming the surface morphologies especially on the rubble-pile asteroids with small gravities and cohesions. The impact experiments and the spectra analyses were conducted to explain the cratering and resurfacing process on the asteroid 25143 Itokawa. The surface of Itokawa is probably not very stable and many phenomena to modify the surface conditions have been discussed in many papers. In this chapter, we are discussing the dynamical evolution of Itokawa comprehensively from various effects and timescales which are depicted by this study and also by the previous papers. First, we review the possible resurface processes on Itokawa and the various age estimates from different methods. Finally, we summarize the results we obtained in previous chapters and discuss possible scenarios for the dynamical evolution of Itokawa.

5.2 Possible resurface processes on Itokawa

Due to the very small surface gravity, the mobility of the asteroidal regolith is considered to be much higher than those of terrestrial planets and the Moon. The surfaces of asteroids can be modified through its beginning to the end by many processes, such as dust levitation, impact-induced shaking, tidal force, fragmentation of regolith, YORP spin-up and impact gardening. These processes might cause a difference in maturity rates and the regolith deposition time (space weathering time) depending on their effective depths.

5.2.1 Dust levitation

Compared to the Moon or Mercury, Itokawa less fine particles on their surface, in particular < 100 micron. Bodies exposed to solar radiation and solar wind acquire the high electrical energetic state, which have been observed on the Moon and artificial satellites. Electrostatic dust levitation could raise the mobility of dust and fine regolith

on the surface. On asteroids the surface dust levitation was hypothesized to explain loosing their fine regolith (Lee, 1996). From the ground-based observational point of view, the thermal inertia is an indicator of the coarseness of the surface and suggests most asteroids have coarser surfaces than the Moon. Especially small asteroids smaller than 100 km in diameter might have coarse surface (Delbo ' and Tanga, 2009). The direct observation was conducted by the spacecraft Hayabusa, and its high-resolution images revealed the block size distribution on Itokawa and the cut-off at the small particle size was relatively large as mm to a few meters (Mazrouei et al., 2014). Indirect evidence for dust levitation was suggested by the samples from Itokawa. The spacecraft Hayabusa had been planned to collect ejected samples by shooting its surface, but the impactors were not fired and it was unsuccessful (Yano et al., 2006). Thus, the returned samples smaller than 180 micron were considered to be caught lofting around Itokawa (Tsuchiyama et al., 2011). That is, any process to excite dusts on Itokawa was implied, and one of the possible mechanisms can be dust levitation by electrical force (Nagao et al., 2011). However, it should be noted that the direct measurement did not prove for the presence of dust levitation on asteroids including Itokawa. Lee (1996), the early theoretical estimation, suggested the particles up to $\sim 10^{-2} - 10^{2}$ mm might be subjected to electrostatic transport. A numerical model showed that the micron-sized particle on Eros could keep levitating and possibly caused the ponds (Colwell et al., 2005). The electrostatic lofting could raise the movability of regolith on Itokawa too, however, the size range of most probable movable particles is estimated from cm to a few ten cm (Hartzell and Scheeres, 2011). That is, the craters on the rough terrain of Itokawa which is mostly covered by meter-sized boulders cannot be resurfaced by dust levitation. On the other hand, the spectral time and the regolith motional time can be affected by this process.

5.2.2 Tidal force by planetary encounters

With the growing spectral datasets, the more Q-type asteroids, which have been associated as spectral analogues to ordinary chondrites, were discovered among the NEOs, while the Q-types are rare in the main-belt samples (Bus and Binzel, 2002a; Binzel et al., 2004; Mothé-Diniz and Nesvorný, 2008). The NEOs were found to populate the Q-type region and the intervening spectral component space between the S- and Q-types (Fig. 1.4). Thus, the S-type spectra were suggested to transform from Q-types possibly by space weathering. Binzel et al. (2004) has shown the great size dependence of the spectral slope and the asteroids smaller than 5 km were found to have small dependence. Smaller objects have shorter collisional lifetimes, suggesting that the smaller asteroids have younger and less redder surfaces. However, this explanation appeared to be less likely because the lifetimes for km-sized asteroids are supposed to be longer than the space weathering timescales order of million years (Bottke et al., 2005). From the analysis of the minimum orbit intersection distance, Q-types were found to be a class of asteroids that show a strong correlation (a statistical confidence level of more than 99%)

with orbital history and encounter the Earth within the past few hundred thousand years (Binzel et al., 2010). Their favorable explanation for formation of Q-type spectra is a close Earth encounter that produces tidal stress and causes slight modification and deformation probably undergo seismic shaking. This encounter timescale leads the consistent short space-weathering rate from Vernazza et al. (2009). The encounter distance threshold of resurfacing was estimated range of 5 – 20 Earth-radii depending on the space weathering timescale (Binzel et al., 2010; Nesvornỳ et al., 2010). Tidal force may contribute to modify the surface structures significantly if Itokawa closely encountered with the Earth, Mars and/or Venus.

5.2.3 Fragmentation of surface regoliths and blocks

Two principal mechanism of fragmentation of regolith are suggested: collisional disruption by meteorite impacts and thermal fatigue fragmentation. Usually larger objects should have finer regolith owing to fragmentation of regoliths and blocks on their surface for longer lifetimes. The observation of thermal inertia of asteroids agreed on this relationship (Delbo ' and Tanga, 2009). The fragmentation of surface blocks was first suggested and related to meteorite impacts on lunar (e.g. Shoemaker, 1971; Gault, Hörz, and Hartung, 1972; Hörz et al., 1975). Micrometeoroids operate on two different scales and results in single particle abrasion and catastrophic rupture. Both help to generate newer surface and finer regoliths. The model calculation done by Hörz et al. (1975) estimated the survival time at which 50% of original 10 cm rocks were destroyed is on the oder of 10 Myr and 500 Myr for the 4 m rocks on the moon. The survival lifetime of surface boulders on the moon were investigated also in observational way. The measurement of the ejecta rock size distribution on several crater rims showed a correlation with the crater ages (Basilevsky, Head, and Horz, 2013). The lunar rocks ≥ 2 m in diameter were found to survive 40 – 80 Myr. This result was relatively faster than the timescale extrapolated by the model simulation of Hörz et al. (1975). Of coarse, smaller rocks takes shorter time to be ruptured, for example, a 1-cm rock require ~ 2 Myr on NEOs and ~ 20 Myr on MBAs.

A resent experimental study suggested another mechanism to generate finer regoliths: thermal fatigue fragmentation (Delbo et al., 2014). Cyclic diurnal temperature variations cause mechanical inner stresses to the boulders on asteroid surfaces. These stresses were estimated to be capable to induce thermal fatigue growth on both a carbonaceous chondrite and an ordinary chondrite based on laboratory experiments (Delbo et al., 2014). Their measurements reported that the pre-existing cracks grew in length at a rate of about 0.5 mm/yr in the near-Earth orbits. Thus, the rate suggested a 1-cm rock on the surface of NEOs could fragment into smaller in ~ 20 yr, arguing much faster fragmentation than by micrometeoroid impacts with a few Myr. In addition, in the main-belt , thermal fatigue fragmentation would still play a great role despite the lower temperature. Thermal fatigue fragmentation could be the main mechanism to

generate fine (< 1 cm) regoliths, but this mechanism is less likely to cause the fragmentation of m-sized blocks because the longer-lived m-sized boulders on the moon was reported in the Apollo mission (Basilevsky et al., 2015). Furthermore, the rejuvenating rate by fragmentation might not as fast as Delbo et al., 2014 suggests because the regolith on Sagamihara regio have been maturing. if thermal fatigue fragmentation were dominant to generate finer regolith, the spectral difference between Sagamihara and Muses-C, which are the main parts of smooth terrains, should not be observed.

Moreover, these processes might be driven homogeneously on asteroid surfaces, and so could not explain the heterogeneity of the surface maturity of Itokawa.

5.2.4 YORP spin-up

The YORP (Yarkovsky-O'keefe-Radzievskii-Paddack) effect is on of possible explanation to produce geologically high-energy environment on the surface of small objects and yields the regolith escape and/or migration. The YORP effect is well-known process to alter the spin rate of small bodies by sunlight (e.g. Rubincam, 2000). The difference of reflection and absorption of sunlight causes YORP torque. Thus, YORP torque due to the asymmetrical shape of an asteroid can spin the prograde rotator up and the retrograde rotator down for long time.

The YORP effect may spin some of asteroids up faster and faster, and they might undergo transformation and even fission (Walsh, Richardson, and Michel, 2008). Especially, rubble-pile asteroids may modify their shape into symmetrical shapes because of their weakness (Holsapple, 2007; Sánchez and Scheeres, 2014).

On Itokawa, the effect was susceptible to the center-of-mass offset which even changes the sign of the effect (Scheeres and Gaskell, 2008). Based on the long-term telescopic observation, the YORP spin-up of $(3.54 \pm 0.38) \times 10^{-8}$ rad day^{-2} was detected by Lowry et al. (2014). Although the centrifugal force is the most effective on the equatorial region, we could observe fine particles in Arcoona regio which is placed on the equator of Itokawa. This might suggest that the centrifugal force is not large enough to release at least cm-sized particles which has more mobility than larger ones. Moreover, if the YORP spin-up is responsible for resurfacing of Itokawa, the degree of space weathering must vary depending on the distance from the spin-axis, that is, the further place from spin-axis, such as Arcoona regio, should have the newer surface and the close place from spin-axis, such as Muses-C regio, should have the older surface. The dependence on locations does not appear and the YORP effect likely to be weak on global resurfacing.

5.3 Analyses of Itokawa particles

5.3.1 Particle shapes and space weathered rim

The grains returned by Hayabusa were divided into two groups: angular and rounded samples (Tsuchiyama et al., 2011; Tsuchiyama et al., 2013). Sharp steps formed by mechanical fracturing were observed on angular surfaces, while faint or no steps were observed on rounded surfaces. The edges of Itokawa particle surfaces are usually angular but the presence of rounded samples should be highlighted. The rounded shapes might indicate continuous motion of particles and geologically high-energy environment on Itokawa.

The rims of Itokawa particles were supposed to formed by space weathering, ranging 30 – 60 nm, which was consistent with the rims of lunar soils by the Appollo missions (Noguchi et al., 2011). The rims were categorized into three textural types: redeposit (thin amorphous rims: Fig. 5.1 A, B), composite rims (redeposit and partially amorphous containing npFe: Fig. 5.1 C, D), and composite vesicular rims (redeposit and partially amorphous containing npFe: Fig. 5.1 E, F) (Noguchi et al., 2014). The redeposit rims do not include $npFe^0$, which induces the spectral modification of materials, while the composite rims are containing npFe (Noguchi et al., 2014). Moreover, these rims were composed of two zones: a redeposition zone (Zone I) and a partially amorphized zone (Zone Ⅱ). The very thin layer of Zone I was suggested to be formed by recoil mixing of elements by implanted solar wind ions, deposition of sputtered material from other grains, and impact-generated, while Zone Ⅱwhich lay under Zone I was suggested to be generated by solar wind implantation (Noguchi et al., 2011; Noguchi et al., 2014). The spectral effect of npFe can be different by size. The abundance of small npFe (1 – 2 nm) in Itokawa particles might cause the reddening of the spectra, while large ones ($>$ 50 nm) cause darkening (e.g. Keller and McKay, 1997; Noble, Pieters, and Keller, 2007). In addition, vesicles observed just above the unaltered part were probably formed by condensation of He^+ ions in implanted solar wind, suggesting that the particles have been saturated by He^+ (Noguchi et al., 2014).

5.3.2 Mineral composition

The compositions of particles fall within the compositional range of LL chondrites: mainly olivine, high- and low-Ca pyroxene and plagioclase (Nakamura et al., 2011, 2012; Tsuchiyama et al., 2011, 2013; 2014; Yurimoto et al., 2011). The measurement of oxygen isotopic compositions also suggested the relation of LL chondrites with Itokawa samples (Yurimoto et al., 2011).

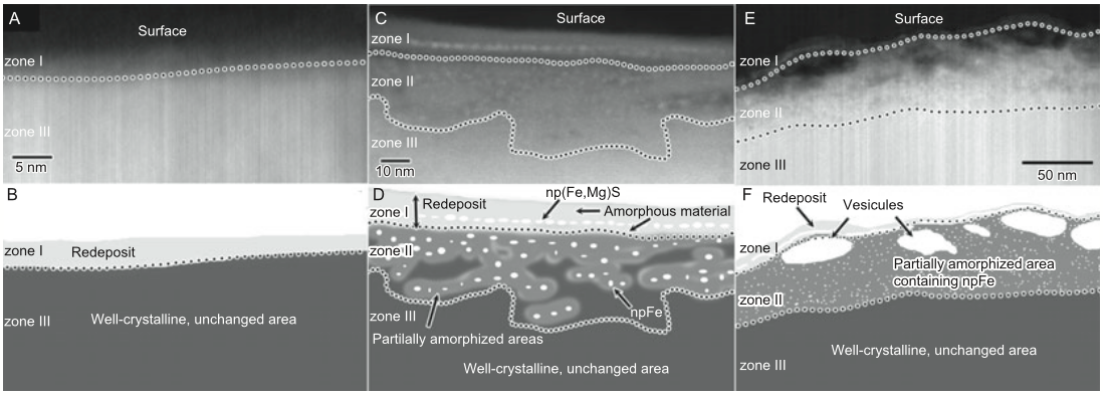

FIGURE 5.1: Three types of rims: thin amorphous rim (redeposit) (A, B), redeposit and partially amorphized rim containing npFe (C, D), and redeposit, and partially amorphized area containing npFe and vesicles (E, F). (From Noguchi et al. (2014))

5.4 Time scales

5.4.1 Rim formation and solar flare tracks

The major mechanism of space weathering on Itokawa was supposed to be caused by solar wind, especially He^+ (Noguchi et al., 2014; Christoffersen and Keller, 2015). Loeffler, Dukes, and Baragiola (2009) obtained the characteristic time of space weathering for S-type asteroids as 5000 yr at 1 AU. Considering that space weathering on Itokawa is still ongoing, the solar wind directly irradiated time might be less than 5000 yr. Noguchi et al. (2014) suggested a fluence of 3×10^{16} He^+ ions cm^{-2} takes less than a few hundred years to form npFe in Itokawa particles at 1.3 AU. These age are consistent with the solar wind direct implantation ages of $\sim 150 - 550$ years suggested by the abundance of Ne (Nagao et al., 2011), suggesting the residence time in uppermost layers.

The density of solar flare tracks recorded the history of irradiation to the solar wind. Not for all particles had the solar flare tracks, densities of a few particles were obtained and the exposure times were estimated (Noguchi et al., 2014; Berger and Keller, 2015). The track densities varied across particles, and suggested the timescale of $10^3 - 10^5$ yr (Noguchi et al., 2014; Berger and Keller, 2015). Moreover, while Noguchi et al. (2014) reported random directions of solar flare tracks about one grain, Berger and Keller (2015) reported two particles out of three preserved the well-defined solar flare track gradients, which implied they had stable orientations for $\sim 10^4 - 10^5$ years.

All these short timescales for rim configurations suggest the geologically energetic state for fine regolith on Itokawa. The fine particles on Itokawa surface could easily have moved and changed their orientations with the timescale ranging 10^2 to 10^5 years.

5.4.2 Spectral age

Koga et al. (2014) performed the principal component analysis for the datasets of 6-band images obtained by AMICA; this is similar analysis that we conducted in Chap. 4. They estimated the surface average age by the shift distance in PC1 score from the spectra of ordinary chondrites, comparing with the spectra change by 40 keV heavy ions Ar^{++} irradiated experiment of Strazzulla et al. (2005), and found < 10 Myr is possible.

Not only the global spectral age but also the spectral ages for returned sample particles were estimated by Bonal et al. (2015). They measured Visible-NIR reflectance spectra of three Itokawa particles. Two out of three particles show compatible spectra with the ground-based observation by Lowry et al. (2005), while one particle has a significantly redder spectrum (red line in Fig. 5.2). Using the space weathering model of Hapke (2001), they inferred 2×10^6 yr for two particles and 8×10^6 yr for one redder particle, considering only heavy ion implantations and they could be shorter. Note that, in any case, because the relative timescale difference remains the same in this model, the redder particle had been exposed ~ 4 times longer than the other two.

Those age estimates are upper limits because other ion particles in solar wind might accelerate space weathering and the timescale would be much shorter. The reflectance spectra also show the variation of exposure times between particles.

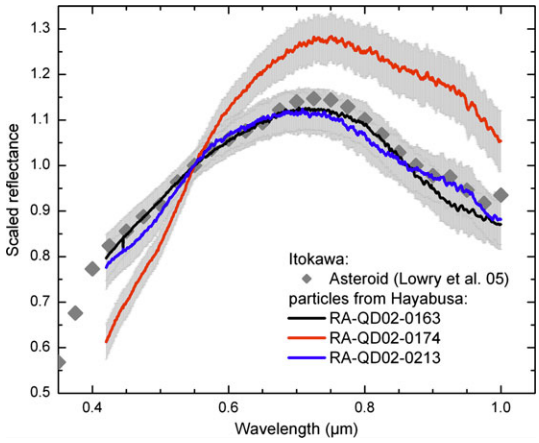

FIGURE 5.2: The spectra of Itokawa particles compared with the ground-based observation by Lowry et al. (2005). (From Bonal et al. (2015))

5.4.3 Solar and galactic ray exposure

Solar cosmic rays (SCRs) are composed of more energetic solar particles of $1 - 100$ MeV/nucleon than solar wind of $\sim$ keV and even higher for galactic cosmic rays (GCRs) of > 0.1 GeV. SCRs can penetrate several centimeters and GCRs can penetrate up to 1 m or more beneath the surface. Interaction with the energetic particles produce many kinds of cosmic nuclides with various half-lives (e.g. Marti and Graf, 1992; Leya et al., 2000; Eugster et al., 2006). Especially low energy nuclear reactions

produces noble gases with characteristic isotopic compositions which are distinguishable from solar wind particles. Nagao et al. (2011) measured the Ne concentrations and ^{21}Ne/^{22}Ne isotope ratios of three Itokawa particles to determine the cosmic ray exposure (CRE) ages as $< 8 - 66$ Myr at 1.3 AU. Other studies for the CRE ages by measuring Ne and He of Itokawa particles followed and they also resulted in young age of $0.6 - 9$ Myr (Meier et al., 2014; Busemann et al., 2015). These ages suggests the residence time for the regolith particles in a few cm depth of the Itokawa surface.

On the other hand the concentration of other isotopic compositions ^{10}Be and ^{26}Al generated by GCR were measured by Nishiizumi, Caffee, and Welten (2015). Note that the production rate of GCR-induced nuclides does not change by distance from Sun, while SCR-induced ones depend on the orbit. The concentration age of ^{10}Be is longer than 3 – 4 Myr because the ratios of ^{10}Be were saturated (Nishiizumi, Caffee, and Welten, 2015). Thus, the residence time in a few meters of regolith particles is supposed to be longer than 3 – 4 Myr.

5.4.4 ^{40}Ar/^{39}Ar age

The radiogenic ^{40}Ar is the product of the decay of ^{40}K. The abundance of ^{40}Ar increases with the time, unless heating causes the crystal structure degradation and release of trapped argon and other gases. Thus, the ratio ^{40}Ar/^{39}Ar indicates the heating history of samples. Solar heating and impacts are thought to be major mechanisms to lose ^{40}Ar, although the closure temperatures vary with minerals. The closure temperature is estimated higher than 375 K and Turner, Enright, and Cadogan (1978) gave an average closure temperatures for chondrites of 488 ± 120 K. Gombosi et al. (2015) reported that the diurnal variations in temperature from 123 K to 393 K leads to lose large amount of ^{40}Ar in small glass spherules on the Moon. The orbit of Itokawa shows the temperature could rise higher than 400 K within a few Myr with small perihelia, however, currently the temperature at perihelia is estimated as ~ 350 K (e.g. Marchi et al., 2009; Michel and Delbo, 2010). Although these estimated temperatures are comparable to the closure temperature, there is small possibility to keep the near-Earth orbit such a long time of a few tens Myr (Bottke et al., 2005).

Impacts could rather possibly play a role for the release of ^{40}Ar. The impact-induced shock itself cannot lead to the loss of argon, but the hot ejecta blankets cause post-shock degassing (e.g. Bogard, 1995).

Three Itokawa particles were dated by the ^{40}Ar/^{39}Ar method and showed the age of $\sim$ 1.3 Gyr (Park et al., 2015). There is still little possibility that the Ar-Ar age shows the closer approach to the Sun, but the orbital simulation tells us the close encounter and heating up to 400 – 450 K within a few Myr did not cause argon degassing (Yoshikawa, 2002). Moreover the present orbit of Itokawa cannot account for solar heating as high as resetting temperature. Therefore, the resetting time of ~ 1.3 Gyr is possibly the catastrophic disruption age of the parent body.

5.5 Dynamical evolution of Itokawa

Based on our experimental results in Chapter 2, the crater retention age on Itokawa have been estimated as 0.7 – 14 Myr in main-belt region, which is more than one order of magnitude shorter than that of previous study, 75 Myr – 1 Gyr (Michel et al., 2009). The great difference in their calculation and in ours is that they used the strength scaling of rigid body for the crater size estimation which causes a much smaller crater for a certain impactor size. Our experiments showed that the cratering efficiency vary significantly by the collision condition of an impactor and a target grain sizes and strengths. However, an impactor can fully disrupt a target grain of 20 times larger than itself in diamter because the average impact velocity among MBAs are as high as ~ 5.3 km/s. Moreover, the m-sized boulders are dominant on Itokawa surface, the large craters which were formed by large impactors wouldn't be influenced by the armoring much, while the number of small craters were possibly depleted by the armoring effect. Note that the craters on Itokawa were suggested to be formed in the main belt, since the collisional probability in the near-Earth orbit is ~ 1000 times less (Stuart and Binzel, 2004; Bottke et al., 2005).

Spectral analyses found that the first principal component (PC1) of Itokawa agrees with the tendency of space weathering, that is, reddening and darkening. The exposure ages of crater-like features on Itokawa, which were indicated by the PC1 score, seem to argue in favor of the unsaturated crater distribution as discussed in Chapter 4. Moreover, the lack of young and large craters suggests the change in impact flux. If the crater had not been saturated, the crater age was as young as on the order of 1–10 Myr with the collision rate in the main belt and it is unrealistic to accumulate all craters in current orbit due to the low impact probability.

Various ages estimated so far are summarized with the intend depths in Fig. 5.3. We note that there are two types of ages, estimated time in the main-belt (dark blue) and in the near-Earth (red). The CRE ages and the spectral ages indicate relatively shallow ages than crater ages. Consequently, the circumstances could easily change and we can not identify their meaning.

Two scenarios are possible to explain these ages:

Scenario 1 The parent body of Itokawa was heavily disrupted ~ 1.3 Gyr ago, which was suggested by Park et al. (2015) from argon degassing age, and formed rubble-pile bodies. The rubble-pile body would be at least the second-generation asteroid. Asteroids could experience several time of disruption to become smaller, so-called collision cascade (e.g. Kobayashi and Tanaka, 2010). The parent body of Itokawa experienced at least two times of disruptions, and the the latest disruption and formation were $\sim 1-10$ Myr which corresponds to the crater retention age calculated in Chapter 2 and 3. The reason why the argon degassing age did not reflect the latest disruption age could be rapid shock wave attenuation from the impact sight due to the porous granular body.

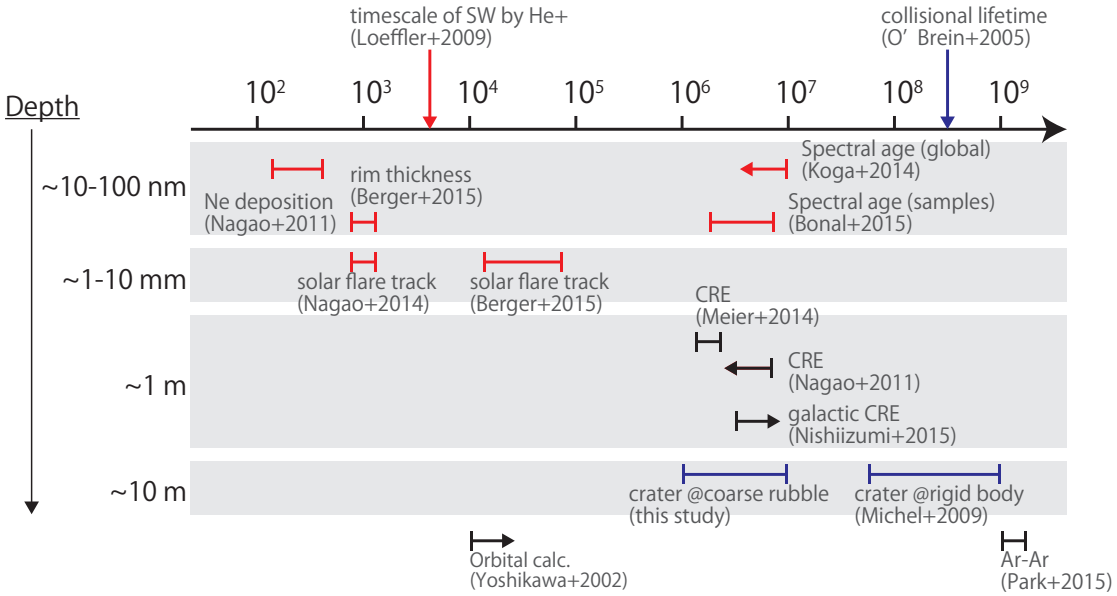

FIGURE 5.3: Various ages and timescales obtained so far are summarized. The estimated times in the main-belt are depicted with dark blue and those in the near-Earth are red.

Although crater ejecta could resurface globally, the escape velocity on Itokawa is less than 1 m/s due to its small gravity and resurface by ejecta is less possible. Moreover, there is statistically little chance to survive ~ 1 Gyr (the argon radioisotopic age), avoiding a collisional disruption since the collisional lifetime of an Itokawa-sized asteroid is estimated to be a few hundred million years (O'Brien and Greenberg, 2005). The formation of the current shape of Itokawa might be the start point of the CRE ages (Nagao et al., 2011; Meier et al., 2014; Nishiizumi, Caffee, and Welten, 2015). Retaining the craters formed in the main belt, Itokawa migrated to the near-Earth orbit through the μ_6 resonance or the Mars crossing orbit (Michel and Yoshikawa, 2006). However, the uppermost surface $\sim$ mm depth was deformed or moved and the spectral ages and the solar flare track ages was reseted, possibly tidal force by encountering with the terrestrial planets. The change in collision rate suggested by the crater distribution in diameter and PC1 score in Chapter 4 indicates the time in near-Earth orbit as the order of 1 Myr which corresponds to crater retention time of PC1 score $\lesssim 0$, which means Itokawa is newly came to near-Earth region. This age is compatible with the CRE ages (Nagao et al., 2011; Meier et al., 2014), the spectral ages (Koga et al., 2014; Bonal et al., 2015), and the orbital calculation residence time (Yoshikawa, 2002).

Scenario 2 The idea that the current Itokawa was formed after at least two disruption is the same as Scenario 1. When the migration from the main-belt to the near-Earth orbit, the global resurface surly happened and lost the regolith at the depth of $\sim$m which can reset the CRE ages but cannot reset the crater retention age with the depth of $\sim 1 - 10$ m. If so, the crater distribution with less smaller craters is compatible. Thus, the CRE ages and the spectral ages indicate the time in the near-Earth region so far.

The short time of the spectral age and the solar flare track ages suggest the intermittent movement of regolith which are possibly triggered by impacts, that is, the high rate of impact gardening is deduced to make the surface apparently younger compared with its formation age.

Note that the resurface by thermal fatigue appears not to be efficient that much. The preservation of different degree in space weathering between Muses-C regio and Sagamihara regio which are similar smoothness suggests the resurface by thermal fatigue did not occur as fast (< 20 yr) as estimated before (Delbo et al., 2014) and might not excess the space weathering rate.

Both of the scenarios are plausible. The CRE ages and the schematic Scenario 1 is depicted in Fig. 5.4. The spectral ages are multiplied by 4 because of change in the distance from the Sun. However, the penetration depth of galactic cosmic rays is supposed to be $\sim$ m, and this is similar to the depth of the craters. Although we cannot necessarily reject the Scenario 2, Scenario 1 appears more favorable for now.

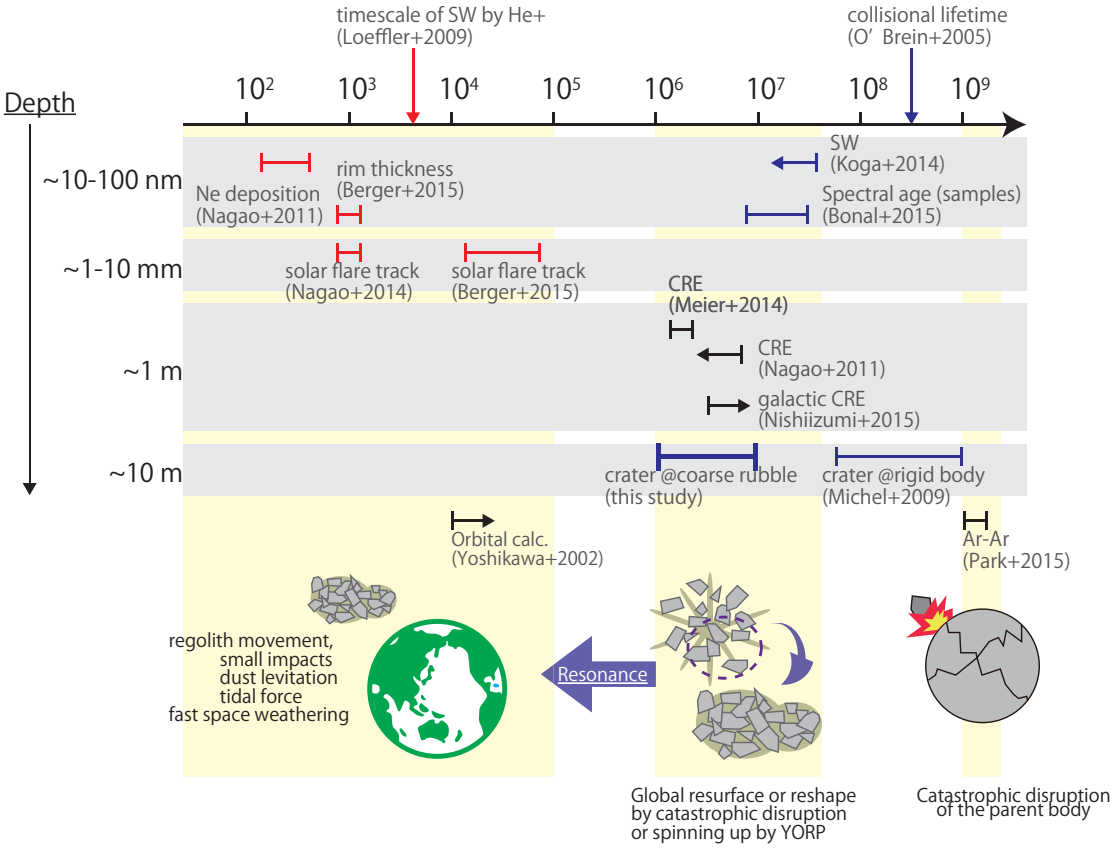

FIGURE 5.4: Various ages of Itokawa and their intend depths. The CRE ages are modified as in the main-belt region. Red ages were estimated as the residence time in the near-Earth and blues were the age in the main-belt. The schematic drawing summarizing the possible evolution of Itokawa: Scenario 1.

Chapter 6

Conclusions

Scaling of cratering on coarse-grained surfaces

We conducted impact experiments on coarse-grained targets to scale crater sizes on rubble-pile asteroids which are loosely combined by small cohesions and gravities. From quarter-space experiments, cratering was found to be divided into two stages, fracture and excavation. The target grains are heavily fractured in the very close vicinity of contact sights, which means very fast attenuation of pressure. In the excavation stage, target grains are rarely disrupted due to slow flow and crater shapes result in similar to simple craters. Modification of the coupling parameter based on momentum transfer from a projectile to a contacted grain allows us to scale the experimental results. There are three cratering modes classified by the energy ratio ξ; when $\xi > 10^4$, energy dissipation by shuttering target grains can be negligible and crater size is as large as the craters on sand targets; when $1 < \xi < 10^4$, energy dissipation would matter and crater size is smaller depends on the size ratio (mass ratio); when $\xi < 1$, a projectile dose not have enough energy to fully disrupt a target grains and results in making a strength-dominated crater on a grain or disrupting only few grain. In the last case, any crater would not be found on the direct observation by spacecrafts.

Crater distribution on Itokawa

Monte Carlo calclations, which take the cratering model on coarse-grained targets and the seismic shaking model (Richardson, Melosh, and Greenberg, 2004) into account, allows us to simulate the crater distribution on Itokawa. The larger crater distribution was replicable with 1 – 10 Myr by our model, in contrast, the smaller craters, especially smaller than 10 m, is not reproduced with the most plausible parameters for the boulder distribution and the regolith depth. Specifically, the smaller craters exceeded on our simulation by an order. However, considering the boulder distribution on the rough terrain, where the minimum cut-off size is reported as $\sim$ 2 m (Mazrouei et al., 2014), due to the armoring effect the production of smaller craters can be suppressed and the crater distribution would be similar to that on Itokawa. In reality, crater deficiency in the smooth terrain was found. Thus, the simulation results suggest two

different regions on Itokawa, the smooth terrain and the rough terrain, might have different crater production and erasure rates. We should infer that another possibility is the small crater erasure event such as the tidal force by encountering terrestrial planets.

Space weathering of craters on Itokawa

We conducted the principal component analysis for discrete spectra of Itokawa from image sets obtained by AMICA on Hayabusa, in the mostly same way as (Koga et al., 2014). Because the first principal component (PC1) is subject to reddening trend and even corresponds to the v-band reflectance, the first principal component is suggested to represent the degree of space weathering. The larger PC1 means the greater in space weathering, that is, the more exposure time. The geologically found crater-like features are correlated with the PC1 distribution. Because the regolith is not stable and moves towards low potential sights (e.g. Miyamoto et al., 2007; Barnouin-Jha et al., 2008), the PC1 score on the floors of craters would indicate the oldnesses of craters. We obtained the PC1-score distribution of craters and translated the PC1 scores to relative ages based on laser irradiation experiments (Sasaki et al., 2001; Hiroi et al., 2007). Thus, the impact rate of Itokawa was found to change from high to low, as any young and large crater is absent. This distribution suggests Itokawa migrated from the frequently-impacted main belt to the moderate near-Earth orbit.

Dynamical evolution of Itokawa

Assumed that the impact rate change is caused by the migration from the main belt to the near-Earth region, the large craters accumulation times are $1 - 10$ Myr in the main belt and > 2 Myr in the near-Earth, respectively. This estimate implies three dynamical hints to Itokawa. First, the retention of craters from the main belt suggests that Itokawa did not encounter terrestrial planets close enough to deform the large craters with depth ~ 10 m. Second, because of the high mobility of regolith, the cosmic ray exposure ages (Nagao et al., 2011; Meier et al., 2014; Nishiizumi, Caffee, and Welten, 2015) and the spectral ages(Koga et al., 2014; Bonal et al., 2015) could be interpreted as either the formation age or the residence time in the near-Earth orbit. Third, considering the collisional life time of a few hundred million years, Itokawa might be more than second generation body as the first catastrophic disruption was ~ 1.3 Gyr ago (Park et al., 2015).

Appendix A

Principal component analysis for ECAS data

TABLE A.1: Bandpasses used in ECAS.

band	effective wavelength μm	FWHM μm
s	0.337	0.047
u	0.359	0.060
b	0.437	0.090
v	0.550	0.057
w	0.701	0.058
x	0.853	0.081
p	0.948	0.080
z	1.041	0.067

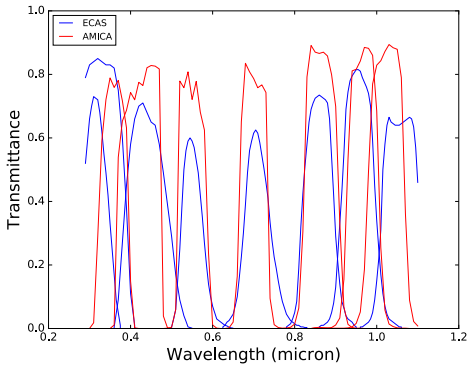

FIGURE A.1: Comparison of transmittances of the filters of ECAS and AMICA.

TABLE A.2: Correlation matrix for the five band reflectances of 534 spectra normalized by v-band.

	u	b	w	x	p
u	1	0.954	-0.725	-0.424	-0.224
b	0.954	1	-0.803	-0.555	-0.376
w	-0.725	-0.803	1	0.789	0.625
x	-0.424	-0.555	0.789	1	0.901
p	-0.224	-0.376	0.625	0.901	1

TABLE A.3: Statistical properties of 534 spectra normalized by v-band.

	u	b	w	x	p
mean value	0.772	0.914	1.088	1.099	1.093
median value	0.831	0.945	1.078	1.098	1.092
standerd deviation	0.175	0.094	0.081	0.093	0.108

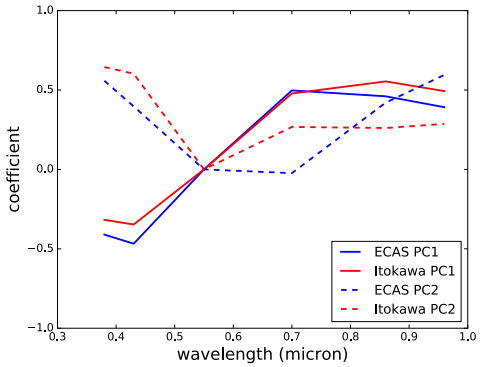

FIGURE A.2: The comparison of the principal components of ECAS data and Itokawa datasets taken by AMICA.

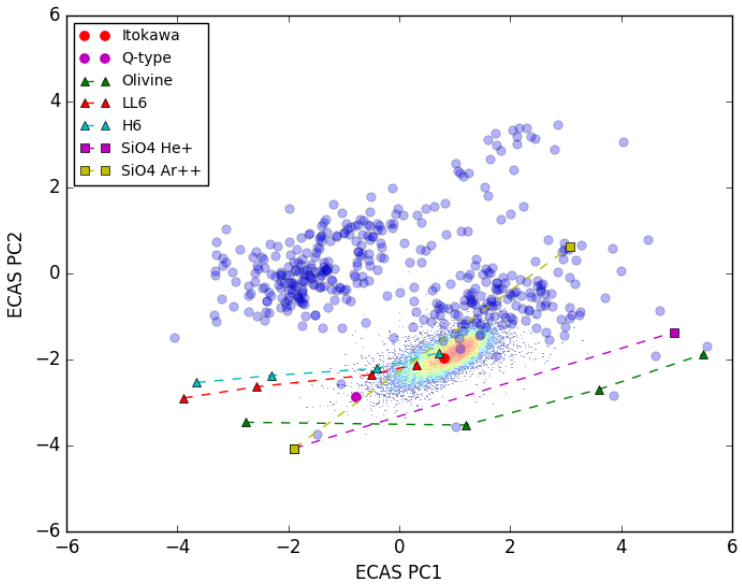

FIGURE A.3: The first principal component and the second principal component space of ECAS data.

Appendix B

Comparison of PCA results of before and after the noise and scattered light removal.

In order to evaluate the robustness of PCA results to the caliblation, we compare the results of before and after noise and scattered light removal. We conduct the PCA for the Itokawa global image set G1 with the same procedure. The longer wavelength is affected by the scattered light (Ishiguro et al., 2014). Figure B.1 compares the noise and scattered light effect for p-band. Before the removal of noise and scattered light, the smear spreads widely to the radial direction, while after the removal of noise and scattered light, the effect is reduced and the image of Itokawa seems clear. Note that before the removal of the scattered light, the image looks brighter due to the accumulation of scattered light from surrounding pixels. Here we evaluate the robustness of the result of PCA by comparing the PCA of those two datasets with and without removal. The results of PCA show the very small difference between before and after the noise and scattered light removal. The correlations of before and after the noise and scattered light removal are 1.000 and 0.979 for PC1 and PC2 respectively, although the smaller principal components have different coefficients because they are more sensitive to the noise and scattered light due to their smaller eigenvalues. The scattered light seems to affect almost uniformly to the pixels inside itokawa area and make the pixels brighter uniformly. However the brightness (intensity) is tuned by the scale factors which are derived for each image set (Table. B.1) and the brightness would be cancelled out.

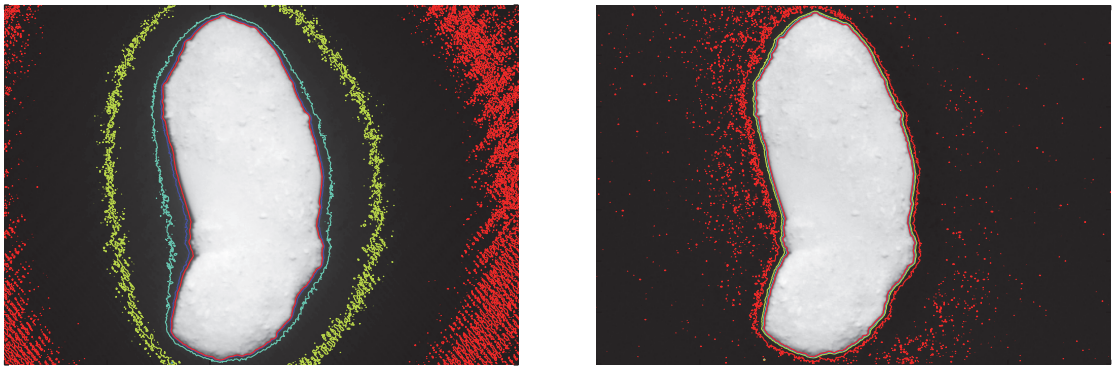

FIGURE B.1: Comparison of the p-band images before (left) and after (right) removal of noise and scattered light. The contour lines indicate the intensity of the noise and scattered light, 1, 5, 10, 15, and 20 % of the Itokawa's average intensity.

TABLE B.1: Scale factors to tune the reflectance intensity to fit the absolute spectrum investigated by the ground-based observations, Binzel et al. (2001) and Lowry et al. (2005).

band	scale factor		difference
	before	after	
ul	6.46	6.67	3.2 %
b	1.23	1.21	-1.6 %
v	1.00	1.00	-
w	0.647	0.647	0.0 %
x	0.636	0.664	4.4 %
p	1.79	2.08	16.2 %

TABLE B.2: Correlation matrix for the five band reflectances of 534 spectra normalized by v-band.

	u	b	w	x	p
u	1	0.954	-0.725	-0.424	-0.224
b	0.954	1	-0.803	-0.555	-0.376
w	-0.725	-0.803	1	0.789	0.625
x	-0.424	-0.555	0.789	1	0.901
p	-0.224	-0.376	0.625	0.901	1

TABLE B.3: Statistical properties and the principal components of Itokawa pixel spectra normalized by v-band.

	before					after				
	ul	b	w	x	p	ul	b	w	x	p
median value	0.676	0.823	1.151	1.054	1.018	0.677	0.823	1.151	1.053	
standerd deviation	0.012	0.016	0.018	0.028	0.045	0.014	0.017	0.020	0.030	0.040
PC1	-0.354	-0.379	0.468	0.539	0.471	-0.358	-0.347	0.477	0.542	0.480
PC2	0.630	0.576	0.284	0.275	0.340	0.601	0.620	0.339	0.261	0.265
PC3	0.192	-0.243	-0.703	0.007	0.640	-0.071	0.011	0.657	0.045	-0.749
PC4	-0.644	0.676	-0.279	0.172	0.141	0.710	-0.702	0.048	0.006	-0.034
PC5	0.164	-0.089	-0.357	0.778	-0.483	-0.045	-0.038	0.472	-0.797	0.371
eigenvalue	0.55	0.24	0.10	0.08	0.03	0.53	0.23	0.10	0.09	0.05

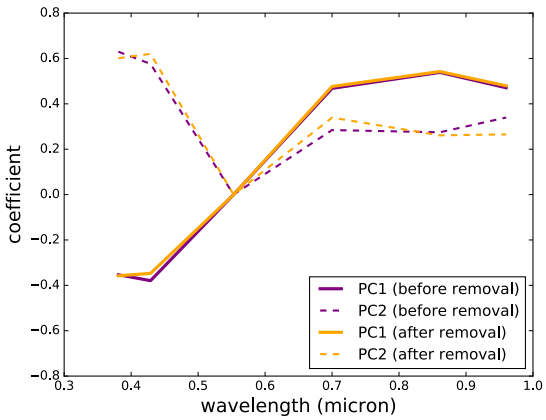

FIGURE B.2: The comparison of the first and second principal components of before and after removal of noise and scattered light.

Appendix C

Ages of S-complex asteroids and their spectra

The disruption ages of several asteroid families have been estimated. On collision, fragments of an asteroid form group and scatter with their fragmentation speed and the YORP effects. The distribution of the asteroids in a family constraints the disruption age of the parent body. S-type families are listed in Table C.1. We plotted the spectra of those families' primary members in principal-component spaces in order to see if there are correlation between the principal components of both ECAS and Itokawa (Figs. C.3 and C.4). The strong correlation were not found. This might be because we did not assesses other members of families. Average values of the member spectra are needed for quantitative analyses. However, we note that Eros has different feature, that is, small absolute value in PC2 and large value in PC1, in the Itokawa PC1–PC2 space, while other spectra are all in positive space in PC2.

TABLE C.1: S-complex asteroid families and estimated age of disruption. (a: Jedicke et al., 2004; Nesvorný et al.; b: 2006a; Nesvorný and Vorouhlický, 2006; c:)

Primary asteroid No.	Primary asteroid name	Age (Myr)	a (AU)	q (AU)	e	H
15	Eunomia	2500 ± 500 a	2.64	2.15	0.187	5.28
20	Messalia	300 ± 100 a	2.41	2.06	0.143	6.50
158	Koronis	2500 ± 1000 a	2.87	2.72	0.052	9.27
170	Maria	3000 ± 1000a	2.55	2.39	0.063	9.39
221	Eos	2000 ± 500a	3.01	2.70	0.105	7.69
606	Brangane	50 ± 40a	2.59	2.02	0.220	10.3
808	Merxia	500 ± 200a	2.75	2.40	0.126	9.8
832	Karin	5.8 ± 0.2a	2.87	2.64	0.078	11.18
847	Agnia	200 ± 100a	2.78	2.52	0.095	10.29
1270	Datura	0.45 ± 0.05 b	2.23	1.77	0.208	12.5
1272	Gefion	1200 ± 400a	2.78	2.36	0.153	12.9
1644	Rafita	1500 ± 500a	2.55	2.15	0.155	11.82
4652	Iannini	2.5 ± 2.5a	2.64	1.82	0.311	13.5
14627	Emilkowalski	0.22 ± 0.03c	2.60	2.21	0.148	13.6
16598	1992 YC2	0.15 ± 0.1c	2.62	2.04	0.220	14.5
21509	Lucascavin	0.55 ± 0.25c	2.28	2.02	0.112	14.8

TABLE C.2: S-complex asteroids which have been explored by spacecrafts and estimated crater retention ages.

Asteroid No.	Asteroid name	Age (Myr)	a (AU)	q (AU)	e	H
21	Lutetia	~ 3600 (a)	2.43	2.03	0.16	7.35
243	Ida	750 ± 250 (b)	2.86	2.74	0.041	9.96
433	Eros	400 ± 200 (b)	1.46	1.13	0.223	11.16
951	Gaspra	~ 65 or ~ 1000 (b)	2.21	1.83	0.173	11.46
2867	Steins	$O(100) - O(1000)$ (c)	2.36	2.02	0.145	12.5
4179	Toutatis	$\sim 1600 \pm 300$ (d)	2.53	0.94	0.6301	15.30

a: (Marchi et al., 2012), b: (O'Brien, Greenberg, and Richardson, 2006), c: (Marchi et al., 2010), d: (Jiang et al., 2015)

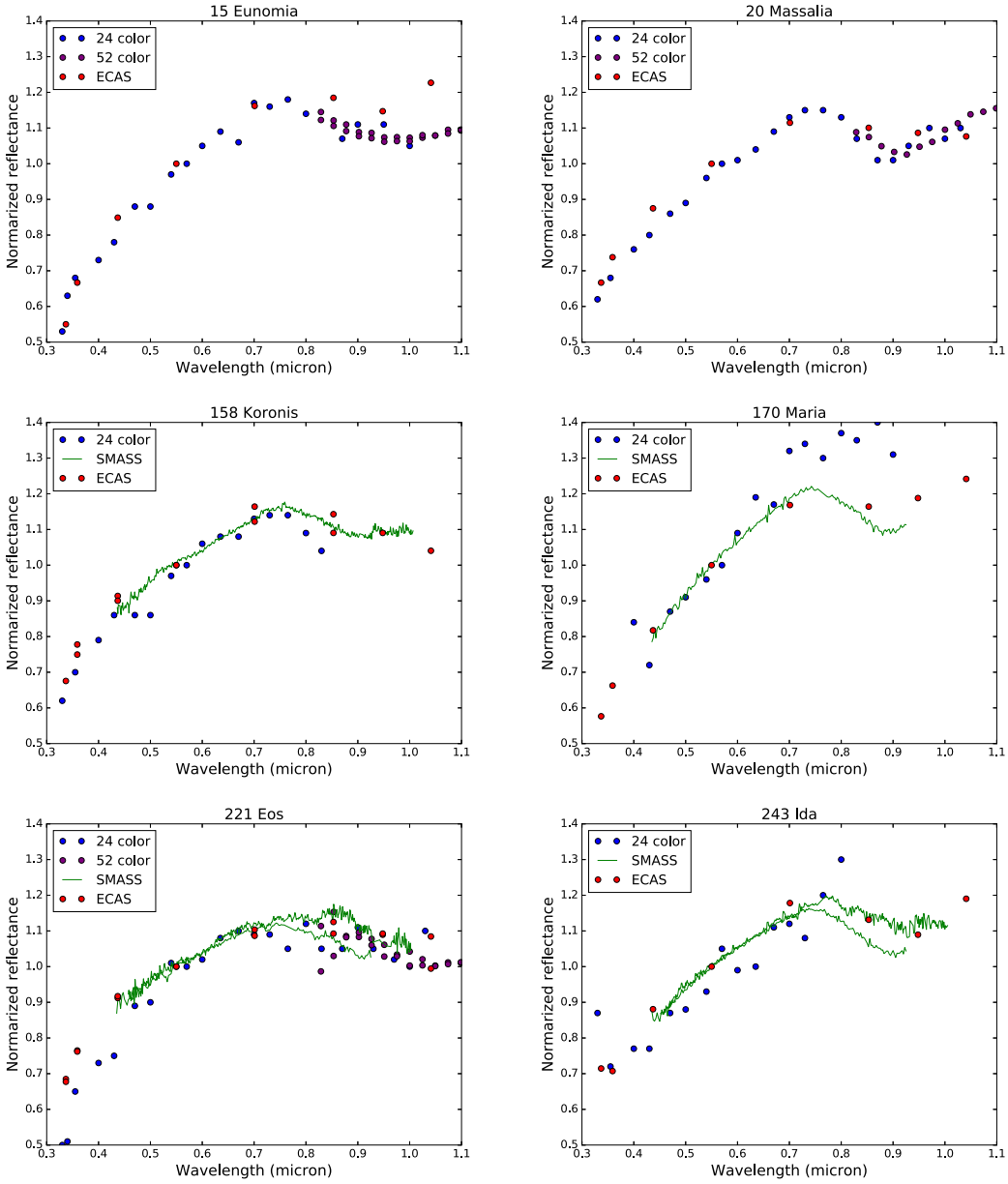

FIGURE C.1: Ground-based observations of S-complex asteroids. All spectra are normalized at 0.55 micron.

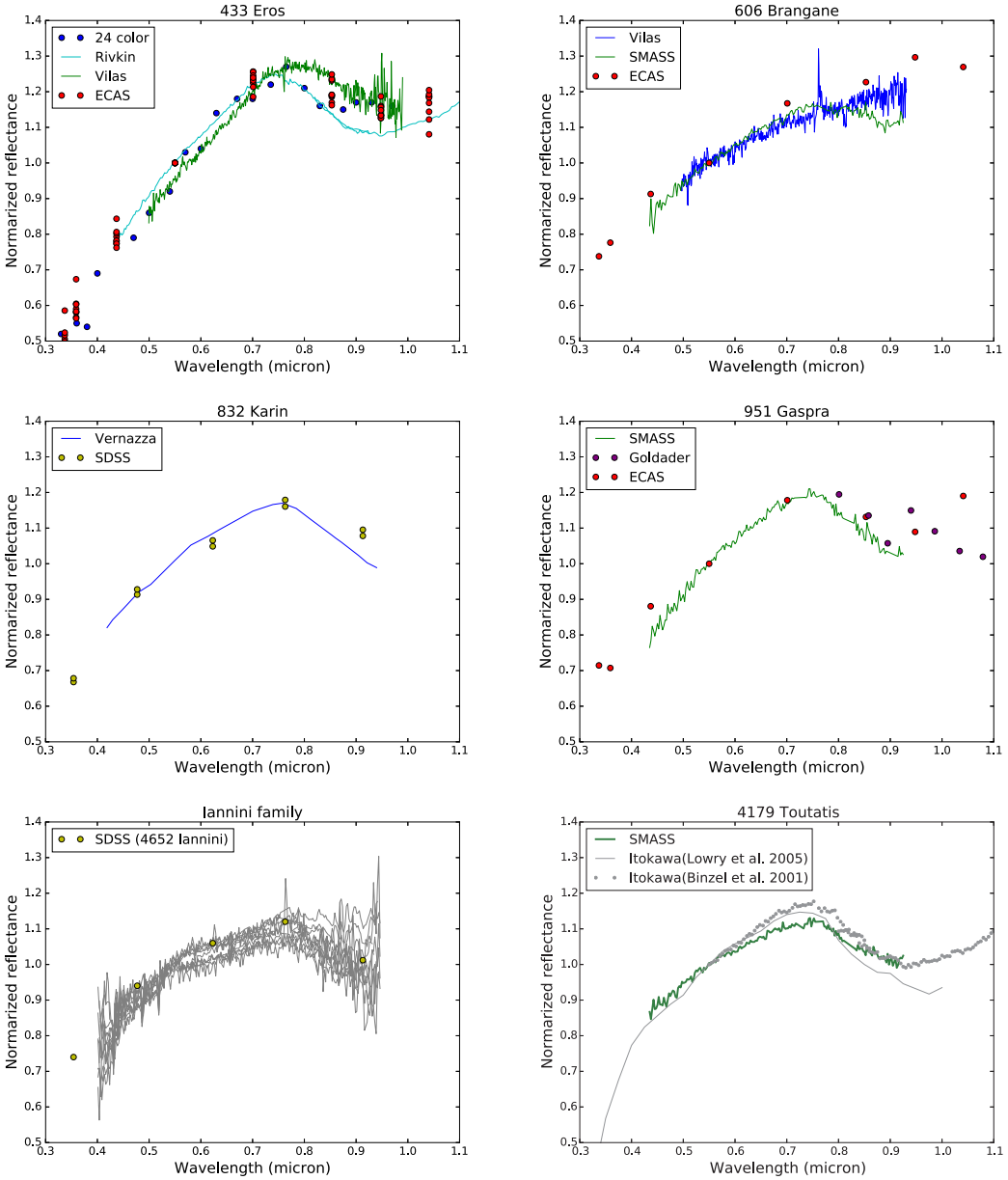

FIGURE C.2: Ground-based observations of S-complex asteroids. All spectra are normalized at 0.55 micron.

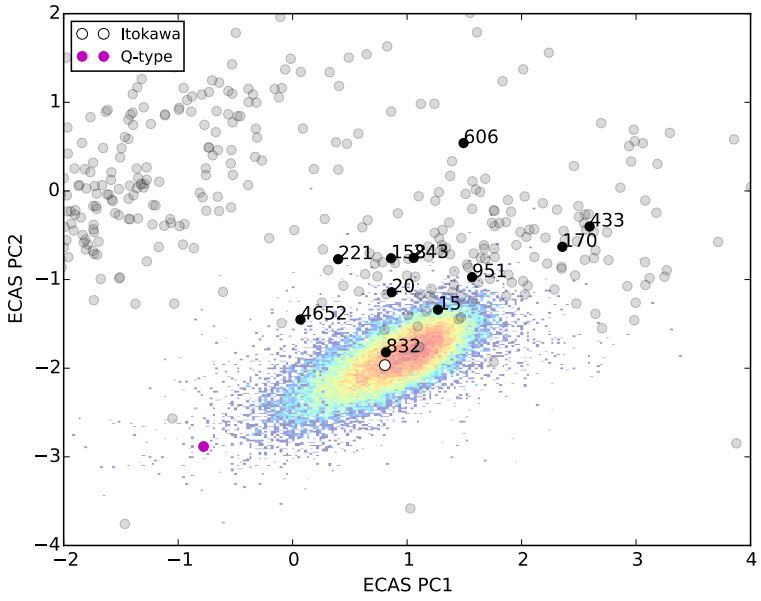

FIGURE C.3: Spectra of S-type asteroids in ECAS PC1–PC2 space. Asteroids are indicated by black markers with numbers.

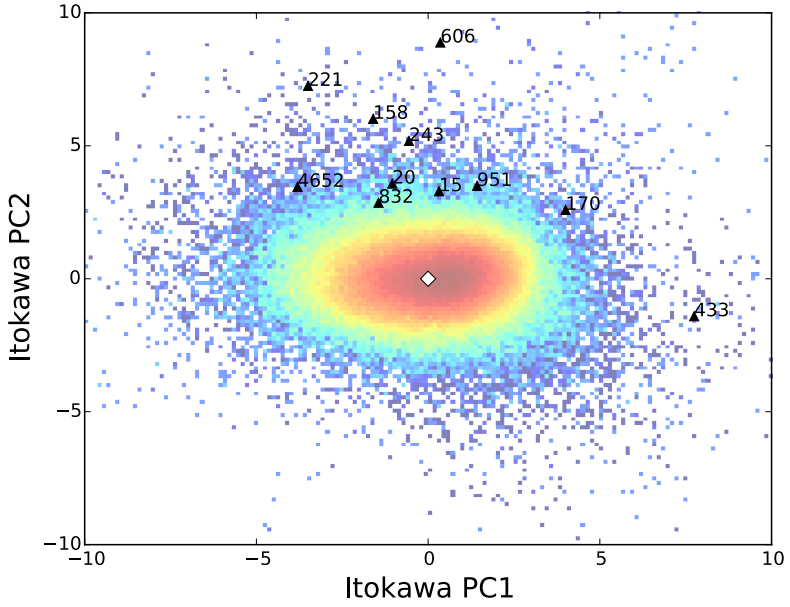

FIGURE C.4: Spectra of S-type asteroids in Itokawa PC1-PC2 space. Asteroids are indicated by black markers with numbers. Eros has distinctive spectra in this space. This might suggest the PC1 indicate space weathering trend in the near-Earth region.

Bibliography

Abe, S. et al. (2006). "Mass and Local Topography Measurements of Itokawa by Hayabusa". In: *Science* 312.5778, pp. 1344–1347.

Adams, J. B. and T. B. McCord (1971). "Alteration of Lunar Optical Properties: Age and Composition Effects". In: *Science* 171.3971.

Asphaug, E. (2009). "Growth and evolution of asteroids". In: *Annual Review of Earth and Planetary Science* 37, pp. 413–448.

Barnouin, O. S. et al. (2011). "Crater formation in pre-existing target structures: Implications for small bodies". In: *EPSC-DPS Joint Meeting 2011*, p. 1396.

Barnouin-Jha, O. S., M. J. Cintala, and D. A. Crawford (2002). "Investigating the Effects of Shock Duration and Grain Size on Ejecta Excavationand Crater Growth". In: *Lunar. Planet. Sci. Conf.* Vol. 33, p. 1738.

— (2005). "Impact into coarse grained spheres". In: *Lunar. Planet. Sci. Conf.* Vol. 36, p. 1585.

Barnouin-Jha, O. S. et al. (2008). "Small-scale topography of 25143 Itokawa from the Hayabusa laser altimeter". In: *Icarus* 198.1, pp. 108–124.

Basilevsky, A. T., J. W. Head, and F. Horz (2013). "Survival times of meter-sized boulders on the surface of the Moon". In: *Planetary and Space Science* 89, pp. 118–126.

Basilevsky, A. T. et al. (2015). "Survival Times of Meter-Sized Rock Boulders on the Surface of Airless Bodies". In: *Lunar and Planetary Science Conference*. Vol. 46, p. 1440.

Bell, J. F. et al. (1995). *52-color Asteroid Survey. EAR-A-RDR-3-52COLOR-V2.1*. NASA Planetary Data System.

Belton, M. J. S. et al. (1992). "Galileo encounter with 951 Gaspra: First pictures of an asteroid". In: *Science* 257.5077, pp. 1647–1652.

Belton, M. J. S. et al. (1994). "First images of asteroid 243 Ida". In: *Science* 265.5178, pp. 1543–1547.

Benz, W. and E. Asphaug (1999). "Catastrophic disruptions revisited". In: *Icarus* 142.1, pp. 5–20.

Berger, E. L. and L. P. Keller (2015). "Space Weathering of Itokawa Particles: Implications for Regolith Evolution". In: *Lunar and Planetary Science Conference*. Vol. 46. Lunar and Planetary Inst. Technical Report, p. 2351.

Binzel, R. P. et al. (2001). "MUSES ‐ C target asteroid (25143) 1998 SF36: A reddened ordinary chondrite". In: *Meteoritics & Planetary Science* 36.8, pp. 1167–1172.

Binzel, R. P. et al. (2004). "Observed spectral properties of near-Earth objects: results for population distribution, source regions, and space weathering processes". In: *Icarus* 170.2, pp. 259–294.

Binzel, R. P. et al. (2010). "Earth encounters as the origin of fresh surfaces on near-Earth asteroids". In: *Nature* 463.7279, pp. 331–334.

Bobrovnikoff, N. T. (1929). "The spectra of minor planets". In: *Lick Observatory Bulletin* 14, pp. 18–27.

Bogard, D. D. (1995). "Impact ages of meteorites: A synthesis". In: *Meteoritics* 30.3, pp. 244–268.

Bonal, L. et al. (2015). "Visible-IR and Raman microspectroscopic investigation of three Itokawa particles collected by Hayabusa: Mineralogy and degree of space weathering based on nondestructive analyses". In: *Meteoritics & Planetary Science* 50.9, pp. 1562–1576.

Bottke, W. (2002). "Debiased Orbital and Absolute Magnitude Distribution of the Near-Earth Objects". In: *Icarus* 156.2, pp. 399–433.

Bottke, W. F. et al. (1994). "Velocity distributions among colliding asteroids". In: *Icarus* 107.2, pp. 255–268.

Bottke, W. F. et al. (2005). "The fossilized size distribution of the main asteroid belt". In: *Icarus* 175.1, pp. 111–140.

Bottke Jr., W. F. and D. Vokrouhlický (2006). "The Yarkovsky and YORP effects: Implications for asteroid dynamics". In: *Annu. Rev. Earth Planet. Sci.* 34, pp. 157–191.

Britt, D. T. et al. (2002). "Asteroid density, porosity, and structure". In: *Asteroids III*.

Brunetto, R. and G. Strazzulla (2005). "Elastic collisions in ion irradiation experiments: A mechanism for space weathering of silicates". In: *Icarus* 179.1, pp. 265–273.

Brunetto, R. et al. (2006a). "Modeling asteroid surfaces from observations and irradiation experiments: The case of 832 Karin". In: *Icarus* 184.2, pp. 327–337.

Brunetto, R. et al. (2006b). "Space weathering of silicates simulated by nanosecond pulse UV excimer laser". In: *Icarus* 180.2, pp. 546–554.

Buckingham, E. (1914). "On physically similar systems; illustrations of the use of dimensional equations". In: *Physical Review* 4.4, pp. 345–376.

Bus, S. and R. P. Binzel (2003). *Small Main-belt Asteroid Spectroscopic Survey, Phase II. EAR-A-I0028-4-SBN0001/SMASSII-V1.0*. NASA Planetary Data System.

Bus, S. J. and R. P. Binzel (2002a). "Phase II of the Small Main-Belt Asteroid Spectroscopic Survey A Feature-Based Taxonomy". In: *Icarus* 158.1, pp. 146–177.

Bus, S. J. and R. P. Binzel (2002b). "Phase II of the small main-belt asteroid spectroscopic survey: The observations". In: *Icarus* 158.1, pp. 106–145.

Busemann, H. et al. (2015). "New Noble Gas Data and Further Examinations of Dust from Asteroid Itokawa". In: *Lunar and Planetary Science Conference*. Vol. 46, p. 2113.

Chapman, C. R. (2004). "SPACE WEATHERING OF ASTEROID SURFACES". In: *Earth and Planetary Sciences* 32.1, pp. 539–567.

Chapman, C. R., M. Gaffey, and L. McFadden (1993). *24-color Asteroid Survey. EAR-A-DBP-3-RDR-24COLOR-V2.1*. NASA Planetary Data System.

Chapman, C. R. and W. B. McKinnon (1986). "Cratering of planetary satellites". In: *IAU Colloq. 77: Some Background about Satellites*. Vol. 1, pp. 492–580.

Chapman, C. R. et al. (2002). "Impact History of Eros: Craters and Boulders". In: *Icarus* 155.1, pp. 104–118.

Christoffersen, R. and L. P. Keller (2015). "Solar Ion Processing of Itokawa Grains: Constraints on Surface Exposure Times". In: *Lunar and Planetary Science Conference*. Vol. 46. Lunar and Planetary Inst. Technical Report, p. 2084.

Cintala, M. J., L. Berthoud, and F. Hörz (1999). "Ejection-velocity distributions from impacts into coarse-grained sand". In: *Meteoritics & Planetary Science* 34.4, pp. 605–623.

Clark, B. E. et al. (2001). "Space weathering on Eros: Constraints from albedo and spectral measurements of Psyche crater". In: *Meteoritics & Planetary Science* 36.12, pp. 1617–1637.

Collins, G. S. et al. (2002). "Hydrocode simulations of Chicxulub crater collapse and peak-ring formation". In: *Icarus* 157.1, pp. 24–33.

Colwell, J. E. et al. (2005). "Dust transport in photoelectron layers and the formation of dust ponds on Eros". In: *Icarus* 175, pp. 159–169.

Coradini, A. et al. (2011). "The surface composition and temperature of asteroid 21 Lutetia as observed by Rosetta/VIRTIS". In: *Science* 334.6055, pp. 492–494.

CRATER ANALYSIS TECHNIQUES WORKING GROUP (1978). "Standard techniques for presentation and analysis of crater size-frequency data". In: *Icarus* 37, pp. 467–474.

Culling, W. E. H. (1963). "Soil creep and the development of hillside slopes". In: *The Journal of Geology*, pp. 127–161.

Delbo, M. et al. (2014). "Thermal fatigue as the origin of regolith on small asteroids". In: *Nature* 508.7495, pp. 233–236.

Delbo ', M. and P. Tanga (2009). "Thermal inertia of main belt asteroids smaller than 100km from IRAS data". In: *Planetary and Space Science* 57.2.

DeMeo, F. E. and B. Carry (2014). "Solar System evolution from compositional mapping of the asteroid belt". In: *Nature* 505.7485, pp. 629–634.

Dukes, C. A., R. A. Baragiola, and L. A. McFadden (1999). "Surface modification of olivine by H^+ and He^+ bombardment". In: *Journal of Geophysical Research* 104, pp. 1865–1872.

Durda, D. D. et al. (2011). "Experimental investigation of the impact fragmentation of blocks embedded in regolith". In: *Meteoritics & Planetary Science* 46.1, pp. 149–155.

Eugster, O. et al. (2006). "Irradiation records, cosmic-ray exposure ages, and transfer times of meteorites". In: *Meteorites and the early solar system II* 1, pp. 829–851.

Farinella, P., D. Vokrouhlickỳ, and W. K. Hartmann (1998). "Meteorite delivery via Yarkovsky orbital drift". In: *Icarus* 132.2, pp. 378–387.

Farinella, P. et al. (1994). "Asteroids falling into the Sun". In:

Flynn, G. J. et al. (2015). "Hypervelocity cratering and disruption of porous pumice targets: Implications for crater production, catastrophic disruption, and momentum transfer on porous asteroids". In: *Planetary and Space Science* 107, pp. 64–76.

Fujiwara, A. and A. Tsukamoto (1980). "Experimental study on the velocity of fragments in collisional breakup". In: *Icarus* 44.1, pp. 142–153.

Fujiwara, A. et al. (2006). "The rubble-pile asteroid Itokawa as observed by Hayabusa." In: *Science* 312.5778, pp. 1330–1334.

Gaffey, M. J. (1976). "Spectral reflectance characteristics of the meteorite classes". In: *Journal of Geophysical Research* 81.5, pp. 905–920.

Gault, D. E., F. Hörz, and J. B. Hartung (1972). "Effects of microcratering on the lunar surface". In: *Lunar and Planetary Science Conference*. Vol. 3, p. 2713.

Gombosi, D. J. et al. (2015). "Argon diffusion in Apollo 16 impact glass spherules: Implications for 40 Ar/39 Ar dating of lunar impact events". In: *Geochimica et Cosmochimica Acta* 148, pp. 251–268.

Gomes, R. et al. (2005). "Origin of the cataclysmic Late Heavy Bombardment period of the terrestrial planets". In: *Nature* 435.7041, pp. 466–469.

Greenberg, R. et al. (1994). "Collisional history of Gaspra". In: *Icarus* 107.1, pp. 84–97.

Greenberg, R. et al. (1996). "Collisional and dynamical history of Ida". In: *Icarus* 120.1, pp. 106–118.

Güttler, C., N. Hirata, and A. M. Nakamura (2012). "Cratering experiments on the self armoring of coarse-grained granular targets". In: *Icarus* 220.2, pp. 1040–1049.

Hapke, B. (2001). "Space weathering from Mercury to the asteroid belt". In: *Journal of Geophysical Research* 106.E5, pp. 10039–10073.

Hartzell, C. M. and D. J. Scheeres (2011). "The role of cohesive forces in particle launching on the Moon and asteroids". In: *Planetary and Space Science* 59, pp. 1758–1768.

Hasselmann, P. H., J. M. Carvano, and D. Lazzaro (2012). *SDSS-based Asteroid Taxonomy V1.1. EAR-A-I0035-5-SDSSTAX-V1.1*. NASA Planetary Data System.

He, D., N. N. Ekere, and L. Cai (1999). "Computer simulation of random packing of unequal particles". In: *Physical Review E* 60.6, p. 7098.

Helfenstein, P. et al. (1994). "Galileo photometry of asteroid 951 Gaspra". In: *Icarus* 107.1, pp. 37–60.

Hirata, N. et al. (2009). "A survey of possible impact structures on 25143 Itokawa". In: *Icarus* 200.2, pp. 486–502.

Hiroi, T. et al. (2006). "Developing space weathering on the asteroid 25143 Itokawa". In: *Nature* 443.7107, pp. 56–58.

Hiroi, T. et al. (2007). "Meteorite analogs of Asteroid 25143 Itokawa: Seeing beyond the effects of grain size and space weathering". In: *Lunar. Planet. Sci. Conf.* Vol. 38, p. 1048.

Holsapple, K. A. (1993). "The scaling of impact processes in planetary sciences". In: *Annual Review of Earth and Planetary Sciences* 21, pp. 333–373.

— (2007). "Spin limits of Solar System bodies: From the small fast-rotators to 2003 EL61". In: *Icarus* 187.2, pp. 500–509.

Holsapple, K. A. and K. R. Housen (2014). "Cratering in Blocky Regoliths". In: *Lunar. Planet. Sci. Conf.* Vol. 45, p. 2538.

Holsapple, K. A. and R. M. Schmidt (1987). "Point source solutions and coupling parameters in cratering mechanics". In: *Journal of Geophysical Research* 92.B7, pp. 6350–6376.

Hörz, F. et al. (1975). "Catastrophic rupture of lunar rocks: A Monte Carlo simulation". In: *The moon* 13.1-3, pp. 235–258.

Huang, J. et al. (2013). "The ginger-shaped asteroid 4179 toutatis: New observations from a successful flyby of Chang'e-2". In: *Scientific reports* 3.

Ishiguro, M. (2014). "Scattered light correction of Hayabusa/AMICA data and quantitative spectral comparisons of Itokawa". In: *Publications of the Astronomical Society of Japan*, psu036.

Ishiguro, M. et al. (2007). "Global mapping of the degree of space weathering on asteroid 25143 Itokawa by Hayabusa/AMICA observations". In: *Meteoritics & Planetary Science* 42.10, pp. 1791–1800.

Ishiguro, M. et al. (2010). "The Hayabusa Spacecraft Asteroid Multi-band Imaging Camera (AMICA)". In: *Icarus* 207.2, pp. 714–731.

Jaumann, R. et al. (2012). "Vesta's shape and morphology". In: *science* 336.6082, pp. 687–690.

Jedicke, R. et al. (2004). "An age-colour relationship for main-belt S-complex asteroids". In: *Nature* 429.6989, pp. 275–277.

Jeffreys, H. (1947). "The relation of cohesion to Roche's limit". In: *Monthly Notices of the Royal Astronomical Society* 107.3, pp. 260–262.

Jiang, Y. et al. (2015). "Boulders on asteroid Toutatis as observed by Chang ' e-2". In: *Scientific reports* 5.

Jutzi, M., P. Michel, and W. Benz (2010). "A large crater as a probe of the internal structure of the E-type asteroid Steins". In: *Astronomy & Astrophysics* 509, L2, p. L2.

Kaasalainen, M., T Kwiatkowski, and M Abe (2003). "CCD photometry and model of MUSES-C target (25143) 1998 SF36". In: *Astronomy & Astrophysics* 405.3, pp. L29–L32.

Kawaguchi, J., K. Uesugi, and A. Fujiwara (2003). "The MUSES-C mission for the sample and return—its technology development status and readiness". In: *Acta Astronautica* 52.2, pp. 117–123.

Keller, H. U. et al. (2010). "E-type Asteroid (2867) Steins as imaged by OSIRIS on board Rosetta". In: *Science* 327.5962, pp. 190–193.

Keller, L. P. and D. S. McKay (1993). "Discovery of Vapor Deposits in the Lunar Regolith". In: *Science* 261.5126.

Keller, L. P. and D. S. McKay (1997). "The nature and origin of rims on lunar soil grains". In: *Geochimica et Cosmochimica Acta* 61.11, pp. 2331–2341.

Keller, L. P. et al. (2000). "Space Weathering in the Fine Size Fractions of Lunar Soils: Mare/Highland Differences". In: *Lunar. Planet. Sci. Conf.* Vol. 31.

Kobayashi, H. and H. Tanaka (2010). "Fragmentation model dependence of collision cascades". In: *Icarus* 206.2, pp. 735–746.

Koga, S. et al. (2014). "Spectral Evolution Tracks of S-Type Asteroids Suggested by Principal Component Analysis of Multi-Band Images of Itokawa". In: *Lunar. Planet. Sci. Conf.* Vol. 45, p. 1721.

Krasinsky, G. (2002). "Hidden Mass in the Asteroid Belt". In: *Icarus* 158.1, pp. 98–9105.

Lazzarin, M. et al. (2006). "Space weathering in the main asteroid belt: The big picture". In: *The Astrophysical Journal Letters* 647.2, p. L179.

Lee, P. (1996). "Dust Levitation on Asteroids". In: *Icarus* 124, pp. 181–194.

Levison, H. F. et al. (2001). "Could the lunar "Late Heavy Bombardment" have been triggered by the formation of Uranus and Neptune?" In: *Icarus* 151.2, pp. 286–306.

Leya, I. et al. (2000). "The production of cosmogenic nuclides in stony meteoroids by galactic cosmic ray particles". In: *Meteoritics and Planetary Science* 35, pp. 259–286.

Loeffler, M. J., C. A. Dukes, and R. A. Baragiola (2009). "Irradiation of olivine by 4 keV He^+: Simulation of space weathering by the solar wind". In: *Journal of Geophysical Research (Planets)* 114, E03003, E03003.

Lowe, D. G. (2004). "Distinctive image features from scale-invariant keypoints". In: *International journal of computer vision* 60.2, pp. 91–110.

Lowry, S. C. et al. (2005). "Physical properties of Asteroid (25143) Itokawa–Target of the Hayabusa sample return mission". In: *Icarus* 176.2, pp. 408–417.

Lowry, SC et al. (2014). "The internal structure of asteroid (25143) Itokawa as revealed by detection of YORP spin-up". In: *Astronomy & Astrophysics* 562, A48.

Marchi, S. et al. (2009). "Heating of near-Earth objects and meteoroids due to close approaches to the Sun". In: *Monthly Notices of the Royal Astronomical Society* 400.1, pp. 147–153.

Marchi, S. et al. (2010). "The cratering history of asteroid (2867) Steins". In: *Planetary and Space Science* 58.9, pp. 1116–1123.

Marchi, S. et al. (2012). "The cratering history of asteroid (21) Lutetia". In: *Planetary and Space Science* 66.1, pp. 87–95.

Marti, K. and T. Graf (1992). "Cosmic-ray exposure history of ordinary chondrites". In: *Annual Review of Earth and Planetary Sciences* 20, pp. 221–243.

Maxwell, D. E. (1977). "Simple Z model for cratering, ejection, and the overturned flap." In: *Impact and Explosion Cratering: Planetary and Terrestrial Implications*. Vol. 1, pp. 1003–1008.

Mazrouei, S. et al. (2014). "Block distributions on Itokawa". In: *Icarus* 229, pp. 181–189.

Meier, M. M. M. et al. (2014). "A Precise Cosmic-Ray Exposure Age for an Olivine Grain from the Surface of Near-Earth Asteroid (25143) Itokawa". In: *Lunar. Planet. Sci. Conf.* Vol. 45, p. 1247.

Melosh, H. J. (1989). *Impact Cratering: A Geologic Process*. Oxford monographs on geology and geophysics. Oxford University Press. ISBN: 9780195104639.

Michel, P. and M. Delbo (2010). "Orbital and thermal evolutions of four potential targets for a sample return space mission to a primitive near-Earth asteroid". In: *Icarus* 209.2, pp. 520–534.

Michel, P. and M. Yoshikawa (2006). "Dynamical origin of the asteroid (25143) Itokawa: the target of the sample-return Hayabusa space mission". In: *Astronomy & Astrophysics* 449.2, pp. 817–820.

Michel, P. et al. (2009). "Itokawa's cratering record as observed by Hayabusa: Implications for its age and collisional history". In: *Icarus* 200.2, pp. 503–513.

Michikami, T. et al. (2008). "Size-frequency statistics of boulders on global surface of asteroid 25143 Itokawa". In: *Earth, Planets and Space* 60.1, pp. 13–20.

Miyamoto, H. et al. (2007). "Regolith Migration and Sorting on Asteroid Itokawa". In: *Science* 316.5827, pp. 1011–1014.

Morbidelli, A. et al. (2000). "Source regions and timescales for the delivery of water to the Earth". In: *Meteoritics & Planetary Science* 35.6, pp. 1309–1320.

Moroz, L. et al. (2004). "Optical alteration of complex organics induced by ion irradiation:: 1. Laboratory experiments suggest unusual space weathering trend". In: *Icarus* 170.1, pp. 214–228.

Mothé-Diniz, T. and D. Nesvorný (2008). "Visible spectroscopy of extremely young asteroid families". In: *Astronomy & Astrophysics* 486, pp. L9–L12.

Murchie, S. et al. (2002). "Color Variations on Eros from NEAR Multispectral Imaging". In: *Icarus* 155.1, pp. 145–168.

Nagao, K. et al. (2011). "Irradiation history of Itokawa regolith material deduced from noble gases in the Hayabusa samples". In: *Science* 333.6046, pp. 1128–1131.

Nakamura, A. and A. Fujiwara (1991). "Velocity distribution of fragments formed in a simulated collisional disruption". In: *Icarus* 92.1, pp. 132–146.

Nakamura, A. M. et al. (2008). "Impact process of boulders on the surface of asteroid 25143 Itokawa—fragments from collisional disruption". In: *Earth, Planets and Space* 60.1, pp. 7–12.

Nakamura, E. et al. (2012). "Space environment of an asteroid preserved on micrograins returned by the Hayabusa spacecraft". In: *Proceedings of the National Academy of Sciences* 109.11, E624–E629.

Nakamura, T. et al. (2011). "Itokawa dust particles: a direct link between S-type asteroids and ordinary chondrites". In: *Science* 333.6046, pp. 1113–1116.

Nesvornỳ, D. and W. F. Bottke (2004). "Detection of the Yarkovsky effect for main-belt asteroids". In: *Icarus* 170.2, pp. 324–342.

Nesvornỳ, D. and D. Vokrouhlickỳ (2006). "New candidates for recent asteroid breakups". In: *The Astronomical Journal* 132.5, p. 1950.

Nesvornỳ, D., D. Vokrouhlickỳ, and W. F. Bottke (2006). "The breakup of a main-belt asteroid 450 thousand years ago". In: *Science* 312.5779, pp. 1490–1490.

Nesvornỳ, D. et al. (2002). "The recent breakup of an asteroid in the main-belt region". In: *Nature* 417.6890, pp. 720–771.

Nesvorný, D. et al. (2005). "Evidence for asteroid space weathering from the Sloan Digital Sky Survey". In: *Icarus* 173.1, pp. 132–152.

Nesvornỳ, D. et al. (2010). "Do planetary encounters reset surfaces of near Earth asteroids?" In: *Icarus* 209.2, pp. 510–519.

Nishiizumi, K., M. W. Caffee, and K. C. Welten (2015). "Measurements of Cosmogenic Radionuclides in a Hayabusa Sample". In: *Lunar and Planetary Science Conference*. Vol. 46, p. 2499.

Noble, S. K., C. M. Pieters, and L. P. Keller (2007). "An experimental approach to understanding the optical effects of space weathering". In: *Icarus* 192.2, pp. 629–642.

Noguchi, T. et al. (2011). "Incipient space weathering observed on the surface of Itokawa dust particles." In: *Science* 333.6046, pp. 1121–1125.

Noguchi, T. et al. (2014). "Space weathered rims found on the surfaces of the Itokawa dust particles". In: *Meteoritics and Planetary Science* 49, pp. 188–214.

Nolan, M. C. et al. (1996). "Impact Craters on Asteroids: Does Gravity or Strength Control Their Size?" In: *Icarus* 124, pp. 359–371.

O'Brien, D. P. and R. Greenberg (2005). "The collisional and dynamical evolution of the main-belt and NEA size distributions". In: *Icarus* 178.1, pp. 179–212.

O'Brien, D. P., R. Greenberg, and J. E. Richardson (2006). "Craters on asteroids: Reconciling diverse impact records with a common impacting population". In: *Icarus* 183.1, pp. 79–92.

O'Brien, D. P., M. V. Sykes, and P. Tricarico (2011). "Collision Probabilities and Impact Velocity Distributions for Vesta and Ceres". In: *Lunar and Planetary Science Conference*. Vol. 42. Lunar and Planetary Science Conference, p. 2665.

Ohba, Y. et al. (2003). "Pole orientation and triaxial ellipsoid shape of (25143) 1998 SF36, a target asteroid of the MUSES-C* mission". In: *Earth, planets and space* 55.6, pp. 341–347.

O'Keefe, J. D. and T. J. Ahrens (1999). "Complex craters: Relationship of stratigraphy and rings to impact conditions". In: *Journal of Geophysical Research* 104.E11, pp. 27091–27104.

Ostro, S. J., L. A. M. Benner, and M. C. Nolan (2004). "Radar observations of asteroid 25143 Itokawa (1998 SF36)". In: *Meteoritics & Planetary Science Archives* 39.3, pp. 407–424.

O ' Brien, D. P. et al. (2014). "Water delivery and giant impacts in the ' Grand Tack ' scenario". In: *Icarus* 239, pp. 74–84.

Park, J. et al. (2015). "40Ar/39Ar age of material returned from asteroid 25143 Itokawa". In: *Meteoritics & Planetary Science* 50.12, pp. 2087–2098.

Patmore, E. B. et al. (2014). "Compression Strength of Pumice". In: *Lunar. Planet. Sci. Conf.* Vol. 45, p. 2429.

Pieters, C. M., L. A. Taylor, and S. K. Noble (2000). "Space weathering on airless bodies: Resolving a mystery with lunar samples". In: *Meteoritics & Planetary Science* 35.5, pp. 1101–1107.

Pieters, C. M. et al. (1993). "Optical effects of space weathering: The role of the finest fraction". In: *Journal of Geophysical Research* 98.E11, pp. 20817–20824.

Pieters, C. M. et al. (2012). "Distinctive space weathering on Vesta from regolith mixing processes". In: *Nature* 491.7422, pp. 79–82.

Pravec, P. and A. W. Harris (2000). "Fast and slow rotation of asteroids". In: *Icarus* 148, pp. 12–20.

Pravec, P., A. W. Harris, and T. Michalowski (2002). "Asteroid Rotations". In: *Asteroids III*, pp. 113–122.

Reddy, V. et al. (2012a). "Color and albedo heterogeneity of Vesta from Dawn". In: *Science* 336.6082, pp. 700–704.

Reddy, V. et al. (2012b). "Composition of near-earth asteroid (4179) Toutatis". In: *Icarus* 221.2, pp. 1177–1179.

Richardson, J. E., J. H. Melosh, and R. Greenberg (2004). "Impact-Induced Seismic Activity on Asteroid 433 Eros: A Surface Modification Process". In: *Science* 306.5701, pp. 1526–1529.

Richardson Jr., J. et al. (2005). "The global effects of impact-induced seismic activity on fractured asteroid surface morphology". In: *Icarus* 179.2, pp. 325–349.

Rozitis, B., E. MacLennan, and J. P. Emery (2014). "Cohesive forces prevent the rotational breakup of rubble-pile asteroid (29075) 1950 DA". In: *Nature* 512.7513, pp. 174–176.

Rubincam, D. P. (1995). "Asteroid orbit evolution due to thermal drag". In: *Journal of Geophysical Research* 100.E1, pp. 1585–1594.

— (1998). "Yarkovsky thermal drag on small asteroids and Mars-Earth delivery". In: *Journal of Geophysical Research* 103.E1, pp. 1725–1732.

— (2000). "Radiative spin-up and spin-down of small asteroids". In: *Icarus* 148.1, pp. 2–11.

Saito, J. et al. (2006). "Detailed images of asteroid 25143 Itokawa from Hayabusa". In: *Science* 312.5778, pp. 1341–1344.

Saito, J. et al. (2010). *Hayabusa AMICA V1.0. HAY-A-AMICA-3-HAYAMICA-V1.0.* NASA Planetary Data System.

Sánchez, P. and D. J. Scheeres (2014). "The strength of regolith and rubble pile asteroids". In: *Meteoritics & Planetary Science* 49.5, pp. 788–811.

Sasaki, S. et al. (2001). "Production of iron nanoparticles by laser irradiation in a simulation of lunar-like space weathering". In: *Nature* 410.6828, pp. 555–557.

Scheeres, D. J. and R. W. Gaskell (2008). "Effect of density inhomogeneity on YORP: The case of Itokawa". In: *Icarus* 198.1, pp. 125–129.

Scheeres, D. J. et al. (2010). "Scaling forces to asteroid surfaces: The role of cohesion". In: *Icarus* 210.2, pp. 968–984.

Schmidt, R. M. and K. R. Housen (1987). "Some recent advances in the scaling of impact and explosion cratering". In: *International Journal of Impact Engineering* 5.1-4, pp. 543–560.

Schultz, P. H. and D. E. Gault (1975). "Seismic effects from major basin formations on the Moon and Mercury". In: *The Moon* 12.2, pp. 159–177.

Scott, G. D. and D. M. Kilgour (1969). "The density of random close packing of spheres". In: *Journal of Physics D: Applied Physics* 2.6, p. 863.

Setoh, M. et al. (2010). "High- and low-velocity impact experiments on porous sintered glass bead targets of different compressive strengths: Outcome sensitivity and scaling". In: *Icarus* 205.2, pp. 702–711.

Shkuratov, Y. et al. (1999). "A Model of Spectral Albedo of Particulate Surfaces: Implications for Optical Properties of the Moon". In: *Icarus* 137.2, pp. 235–246.

Shoemaker, E. M. (1971). "Origin of fragmental debris on the lunar surface and the history of bombardment of the moon". In: *Presentation at I Seminario de Geologia Lunar, Univ. of Barcelona*.

Sierks, H. et al. (2011). "Images of asteroid 21 Lutetia: a remnant planetesimal from the early solar system". In: *science* 334.6055, pp. 487–490.

Strazzulla, G. et al. (2005). "Spectral alteration of the Meteorite Epinal (H5) induced by heavy ion irradiation: a simulation of space weathering effects on near-Earth asteroids". In: *Icarus* 174.1, pp. 31–35.

Strom, R. G. et al. (2005). "The origin of planetary impactors in the inner solar system." In: *Science* 309.5742, pp. 1847–1850.

Stuart, J. S. and R. P. Binzel (2004). "Bias-corrected population, size distribution, and impact hazard for the near-Earth objects". In: *Icarus* 170.2, pp. 295–311.

Sugita, S., P. H. Schultz, and M. A. Adams (1998). "Spectroscopic measurements of vapor clouds due to oblique impacts". In: *Journal of Geophysical Research* 103.E8, pp. 19427–19441.

Sullivan, R. et al. (1996). "Geology of 243 Ida". In: *Icarus* 120, pp. 119–139.

Takagi, Y., H. Mizutani, and S. I. Kawakami (1984). "Impact fragmentation experiments of basalts and pyrophyllites". In: *Icarus* 59, pp. 462–477.

Tancredi, G., S. Roland, and S. Bruzzone (2015). "Distribution of boulders and the gravity potential on asteroid Itokawa". In: *Icarus* 247, pp. 279–290.

Tholen, D. J. (1984). "Asteroid taxonomy from cluster analysis of photometry". PhD thesis. University of Arizona, Tucson.

Tsiganis, K. et al. (2005). "Origin of the orbital architecture of the giant planets of the Solar System". In: *Nature* 435.7041, pp. 459–461.

Tsuchiyama, A. et al. (2011). "Three-dimensional structure of Hayabusa samples: origin and evolution of Itokawa regolith." In: *Science* 333.6046, pp. 1125–1128.

Tsuchiyama, A. et al. (2013). "Analytical dual-energy microtomography: a new method for obtaining three-dimensional mineral phase images and its application to Hayabusa samples". In: *Geochimica et Cosmochimica Acta* 116, pp. 5–16.

Tsuchiyama, A. et al. (2014). "Three - dimensional microstructure of samples recovered from asteroid 25143 Itokawa: Comparison with LL5 and LL6 chondrite particles". In: *Meteoritics & Planetary Science* 49.2, pp. 172–187.

Turner, G., M. C. Enright, and P. H. Cadogan (1978). "The early history of chondrite parent bodies inferred from Ar-40-Ar-39 ages". In: *Lunar and Planetary Science Conference Proceedings*. Vol. 9, pp. 989–1025.

Vernazza, P. et al. (2009). "Solar wind as the origin of rapid reddening of asteroid surfaces". In: *Nature* 458.7241, pp. 993–995.

Veverka, J. et al. (1999). "NEAR encounter with asteroid 253 Mathilde: overview". In: *Icarus* 140.1, pp. 3–16.

Veverka, J. et al. (2000). "NEAR at Eros: Imaging and spectral results". In: *Science* 289.5487, pp. 2088–2097.

Veverka, J. et al. (2001). "Imaging of Small-Scale Features on 433 Eros from NEAR: Evidence for a Complex Regolith". In: *Science* 292.5516, pp. 484–488.

Vilas, F. et al. (1998). *Vilas Asteroid Spectra V1.1. EAR-A-3-RDR-VILAS-ASTEROID-SPECTRA-V1.1*. NASA Planetary Data System.

Vincent, J. et al. (2012). "Physical properties of craters on asteroid (21) Lutetia". In: *Planetary and Space Science* 66.1, pp. 79–86.

Vokrouhlicky, D. (1998). "Diurnal Yarkovsky effect as a source of mobility of meter-sized asteroidal fragments. I. Linear theory". In: *Astronomy and Astrophysics* 335, pp. 1093–1100.

Wada, K., H. Senshu, and T. Matsui (2006). "Numerical simulation of impact cratering on granular material". In: *Icarus* 180, pp. 528–545.

Walsh, K. J., D. C. Richardson, and P. Michel (2008). "Rotational breakup as the origin of small binary asteroids". In: *Nature* 454.7201, pp. 188–191.

Walsh, K. J. et al. (2011). "A low mass for Mars from Jupiter/'s early gas-driven migration". In: *Nature* 475.7355, pp. 206–209.

Williams, D. R. and G. W. Wetherill (1994). "Size distribution of collisionally evolved asteroidal populations: Analytical solution for self-similar collision cascades". In: *Icarus* 107, pp. 117–128.

Willman, M. et al. (2008). "Redetermination of the space weathering rate using spectra of Iannini asteroid family members". In: *Icarus* 195.

Xu, S. et al. (1995). "Small main-belt asteroid spectroscopic survey: Initial results". In: *Icarus* 115, pp. 1–35.

Xu, S. et al. (1996). *Small Main-Belt Asteroid Survey. EAR-A-M3SPEC-3-RDR-SMASS-V2.1*. NASA Planetary Data System.

Yamada, M. et al. (1999). "Simulation of space weathering of planet-forming materials: Nanosecond pulse laser irradiation and proton implantation on olivine and pyroxene samples". In: *Earth, planets and space* 51.11, pp. 1255–1265.

Yano, H. et al. (2006). "Touchdown of the Hayabusa spacecraft at the Muses Sea on Itokawa". In: *Science* 312, pp. 1350–1353.

Yeomans, D. K. et al. (1997). "Estimating the mass of asteroid 253 mathilde from tracking data during the NEAR flyby". In: *Science* 278.5346, pp. 2106–2109.

Yoshikawa, M. (2002). "Orbital evolution of the MUSES-C mission target:(25143) 1998 SF36". In: *Asteroids, Comets, and Meteors: ACM 2002*. Vol. 500, pp. 331–333.

Yurimoto, H. et al. (2011). "Oxygen isotopic compositions of asteroidal materials returned from Itokawa by the Hayabusa mission". In: *Science* 333.6046, pp. 1116–1119.

Zellner, B. (1973). "Polarimetric Albedos of Asteroids." In: *Bulletin of the American Astronomical Society* 5, p. 388.

Zellner, B., D. J. Tholen, and E. F. Tedesco (1985). "The eight-color asteroid survey: Results for 589 minor planets". In: *Icarus* 61, pp. 355–416.

Zellner, B., D. J. Tholen, and E. F. Tedesco (2009). *Eight Color Asteroid Survey. EAR-A-2CP-3-RDR-ECAS-V4.0*. NASA Planetary Data System.